Swansea University
Prifysgol Abertawe

Super Duplex Stainless Steels: Influence of Copper & Tungsten on the Passivity & Corrosion Resistance

Lottie Hollamby

Swansea University

Submitted to Swansea University in fulfillment of the requirements for the Degree of *Masters of Science by Research.*

September 2023

Summary

This thesis has investigated the corrosion behaviour of three Super Duplex Stainless Steel grades, FERR (UNS 32250), SAF (UNS S32750) and ZER (UNS S32760), with focus on the influence of copper (Cu) and tungsten (W) content on pitting and crevice corrosion. In addition, the influence of surface roughness and deaeration of the environment was explored. The experiments involved potentiostatic polarisation techniques and microscopy to quantify the frequency, area and depth of dissolution observed. Two mass loss models, Faraday's Law & Pit Geometry, were also implemented to further quantity the corrosion seen.

The samples were exposed to a 3.5% w/v $NaCl$ solution and heated from 65 °C to 85 °C at a ramp rate of 40 °C/hour. The Critical Pitting Temperatures (CPT) showed a minimal 4 °C difference between the highest, of additional W content, ZER and the lowest, of low Cu content, SAF. FERR, which has increased Cu content, displayed substantial pit frequency, aligning with the high recorded currents. The presence of metastable pitting was observed, contributing to pit repassivation and lower pitting corrosion in SAF and ZER. Despite expectations, additional W in ZER did not produce significantly improved results. The mass loss calculations correlated well with potentiostatic results although several factors like lacy pits and pit shape variability impacted accuracy.

Samples were used from previous research that were ground to a smoother surface finish and exposed to a 3.5% w/v $NaCl$ solution. A deaerated environment using a nitrogen inlet was created, and the samples heated from 65 °C to 85 °C at a ramp rate of 30 °C/hour. FERR and ZER demonstrated improved performance in the deaerated conditions, attributed to smoother finish reducing pit initiation sites, and decreased cathodic reactions in oxygen depleted environments. SAF exhibited contrasting results with increased dissolution observed.

The samples were exposed to 3.5% w/v $NaCl$ solution at temperatures of 85 °C, 75 °C and 65 °C, utilising an o-ring to change the preferred method of corrosion from pitting to crevice. At 85 °C, all grades exhibited substantial dissolution due to surpassing Critical Crevice Temperatures (CCT). FERR and ZER showed similar crevice depths, implying no significant impact of Cu

or W additions. At 75 °C, a reduction in current and crevice depths were seen, with some samples showing incomplete crevice formation around the circumference. At 65 °C, corrosion rates declined significantly, with some areas showing no crevice formation. FERR and ZER again showed similar performance. SAF exhibited stable performance over the temperature range with potential for a broad range of temperature applications.

Overall, this research highlighted insights into the complex relationship between composition, temperature and other factors of corrosion behaviour. While Cu additions did not show a significant impact in aerated conditions, it showed much improvement in deaerated environments. The addition of W had a more influential role in aerated conditions, although both Cu and W additions performed similarly under the crevice corrosion mechanism. The lower alloyed SAF seemed to have irregular behaviour across all experiments apart from crevice corrosion. Additionally, a smoother surface finish and absence of oxygen became a crucial factor for influencing corrosion rates.

Declarations

This work has not previously been accepted in substance for any degree and is not being concurrently submitted in candidature for any degree.

Signed: Lottie Hollamby

Date: 29/09/2023

This thesis is the result of my own investigations, except where otherwise stated. Other sources are acknowledged by footnotes giving explicit references. A bibliography is appended.

Signed: Lottie Hollamby

Date: 29/09/2023

I hereby give consent for my thesis, if accepted, to be available for electronic sharing

Signed: Lottie Hollamby

Date: 29/09/2023

The University's ethical procedures have been followed and, where appropriate, that ethical approval has been granted.

Signed: Lottie Hollamby

Date: 29/09/2023

Contents

Acknowledgements

I would like to thank my academic supervisor, Professor Jim Sullivan, for his invaluable support and excellent guidance over the past two years. I would also like to thank my industrial supervisor, Rodney Rice, for warmly welcoming me onto this project and great guidance when required. Lastly, I would like to thank my family and friends for their unwavering and much needed support. All of your contributions were essential in the completion of this thesis!

Definitions & Abbreviations

Stainless Steel ..... SS
Intergranular Corrosion ..... IGC
Duplex Stainless Steel ..... DSS
Super Duplex Stainless Steel ..... SDSS
Open Circuit Potential ..... OCP
Critical Pitting Temperature ..... CPT
Critical Crevice Temperature ..... CCT
Pitting Resistance Equivalent Number ..... PREn
UNS S32250 (high copper content/(Cu+) ..... FERR
UNS S32750 (low copper content/(Cu) ..... SAF
UNS S32250 (tungsten & copper content/(W) ..... ZER
Primary Passive Potential ..... Epp
Pitting Potential ..... Epit
Corrosion Current Density ..... icorr
Passive Current Density ..... ipass
Critical Crevice Solution ..... CCS
Repassivation Potential ..... Erp
Critical Pitting Potential ..... CPP

1.0 LITERATURE REVIEW

Super Duplex Stainless Steel

Stainless steel *(SS)* has widespread use across a multitude of applications due to its wide range of properties and excellent resistance in a variety of environments. Its mechanical properties often outweigh associated cost offering high toughness and ductility over extensive temperatures, along with excellent resistance to corrosion and oxidation. Research has experimented with different microstructures introducing martensitic, ferritic and austenitic SS, each providing differing properties for specific use. The differences occur due to the atomic arrangement within the crystal microstructure. Ferrite adopts a body centered cubic structure with one iron atom at each corner and one in the center. Austenite adopts a face-centered cubic structure, with atoms situated at the center of the faces in the structure. The differing structures mean austenitic SS has good corrosion resistance, but they lack strength and are vulnerable to corrosion in chloride environments. They are also susceptible to metallurgical segregation, localised depletion of chromium (Cr) leading to passive breakdown at grain boundaries and intergranular corrosion (IGC). In contrast, ferritic SS have higher strength and greater resistance to corrosion. Austenitic SS only contains up to 20% ferrite but increasing the ferrite volume to 50% provides the best combination of mechanical properties and corrosion characteristics from both microstructures. This 50/50 structure gives rise to the duplex stainless steels (DSS), typically containing 18- 30 wt% Cr with additions of molybdenum (Mo) and nitrogen (N). Early DSS lacked toughness in thick sections, causing issues during heat treatment and casting processes. However, advancements in composition and microstructure have since optimised performance [1][2].

Some DSS have incorporated nickel (Ni), resulting in metastable ferrite present within the austenite grains. This composition is highly resistant to IGC, due to Cr diffusing more rapidly from ferrite than austenite at typical sensitising temperatures. Carbides also tend to form preferentially at the boundaries between ferrite and austenite. With insufficient carbon remaining, carbides cannot precipitate at the austenite grain boundaries. Increasing the Cr content to 25 wt%, whilst maintaining the phase balance through Ni adjustments, Super Duplex Stainless Steel ($SDSS$) is formed, offering optimal corrosion resistance, in particular, pitting corrosion. DSS and SDSS have several advantages, including higher mechanical strength,

corrosion resistance within a broad temperature range (-50 °C to 250 °C) and cost-effectiveness due to reduced Ni content. Corrosion resistant alloys are required in the oil and gas industry to handle process streams containing water and H_2S. Higher alloyed steels and duplex are preferred for pitting, corrosion and SCC enhanced by H_2S [1] [2]. In industry, SDSS is available in three main grades, UNS S32250, UNS S32750 and UNS S32760. Each grade has a differing composition of elements but in particular their copper (Cu) and Tungsten (W) additions. There is ongoing debate regarding specific benefits of these elements, particularly in pitting and crevice corrosion resistance. Henceforth, the three grades of SDSS will be referred to as FERR - UNS S32250 (high copper content), SAF - UNS S32750 (low copper content) and ZER - UNS S32760 (tungsten & copper content).

FERR was the first to incorporate *N* into the composition to improve toughness and corrosion resistance in environments containing chloride ions and Cu, which is vital for corrosion resistance in acids. These improvements increase the mechanical strength allowing it to excel in applications requiring thinner sections such as flue gas desulfurisation [3] [4].

Manufacturing these materials correctly is important, as deviations in heat treatment or welding procedures can alter the microstructure. This results in detrimental phases precipitating that adversely affect localised corrosion resistance and mechanical properties. SDSS is stronger due to its two-phase structure, with ferrite providing strength and austenite providing ductility and toughness, along with refinement of grain size. Ferrite displays high yield strength ranging from 550 to 690 MPa, almost double that of an austenitic SS. This is achieved from solution strengthening by substitutional and interstitial solid solution involving Cr, Ni and N. A material's resistance to plastic deformation depends on grain size, with fine-grained materials exhibiting greater hardness due to the increase in boundary area impeding dislocation motion. Austenite in the SDSS refines the grain size, further enhancing the mechanical properties [5].

SS is characterised by Fe-based alloys containing a minimum of 10.5 wt% Cr. The definition of SDSS extends beyond Cr content and includes the Pitting Resistance Equivalent Number *(PREn)* which is typically >40 for SDSS. This empirical formula compares the combined effects of key alloying elements, such as Cr, Ni and N, for $Fe - Cr - Ni$ alloys using a 'pitting index'. It is a useful indicator of a metal's performance in corrosive environment. The PREn was first proposed by Lorentz and Medawar [6] and included N which is defined by equation (1):

$$PRE_N = Cr\ wt\% + 3.3\ x\ Mo\ wt\% + 16\ x\ N\ wt\% \quad (1)$$

Due to work on the beneficial effects of other alloys such as *W* on the Critical Pitting Potential *(CPP)*, it was proposed that the equation be modified to include *W*, defined in equation (2) [7]:

$$PRE_{N,W} = Cr\ wt\% + 3.3\ (Mo\ wt\% + 0.5\ x\ W\ wt\%) + 16\ x\ N\ wt\% \quad (2)$$

Copper has now been introduced as a beneficial element in the PREn number with an extended formula defined by equation (3) [7]:

$$PRE_{EXT} = Cr\ wt\% + 3.3(Mo\ wt\% + 0.5\ W\ wt\%) + 2(Cu\ wt\%) + 16\ (N\ wt\%) \quad (3)$$

Material	Phase	Chemical Composition (wt%) (Avg)					PRE_N (Avg)	PRE_W (Avg)	PRE_{EXT} (Avg)	E_{pit} (mV) SCE
		Cr	Mo	Cu	W	N				
Ferralium 255	Austenite	24	2.5	1.7	-	0.5	40.1	40.1	43.4	882
	SD	0.18	0.09	0.1	-	-	0.25	0.25	0.3	22
	Ferrite	25.3	3.4	1.1	-	0.07	37.6	37.6	40	518
	SD	0.3	0.23	0.08	-	-	0.6	0.6	0.7	29
SAF 2507	Austenite	24	2.4	0.24	0.7	0.52	40	41.5	42	862
	SD	0.09	0.04	0.03	0.07	-	0.12	0.44	0.35	25
	Ferrite	26.2	3.8	0.18	0.9	0.07	39.8	41.6	42	540
	SD	0.29	0.08	0.01	0.03	-	0.37	0.52	0.53	44
Zeron 100	Austenite	23.3	2.8	0.7	0.6	0.46	39.8	41.6	42.6	868
	SD	0.43	0.1	0.05	0.04	-	0.7	0.6	0.6	21
	Ferrite	25.6	3.3	0.48	0.9	0.07	37.8	39.4	40.4	503
	SD	0.36	0.1	0.02	0.07	-	0.47	0.38	0.38	34
PRE_N = %Cr + (3.3 %Mo) + (16 %N) PRE_w = %Cr + 3.3 (%Mo + 0.5% W) + 16 (%N) PRE_{EXT} = %Cr + 3.3(%Mo + 0.5 % W) + 2(%Cu) + 16 (%N)										

Table 1: PREn numbers calculated from compositional elements in three SDSS grades. SD referring to the standard deviation [7]

Previous work has been undertaken to calculate the PREn numbers of the grades used in this thesis. As these are not the exact same batch of material, this cannot be used for direct comparison

in this paper, but as a base understanding of how these grades may corrode. Given the potential for uneven distribution of elements in the two-phase material, calculations are performed separately for each phase, with the lower value determining the PREn.

Based on the table J. Alsarraf [7] configured in **Table 1**, the PREext is highest in FERR due to Cu segregating in the austenite phase. However, pitting usually takes place in the ferrite phase due to lower pitting potential as N and Ni wt% are higher in austenite. This could be reasoning behind why the ferrite PREext may be the lowest. In practice, a uniform distribution of elements can improve pitting corrosion by reducing composition disparities in the two phases. In the table, 'SD' refers to the standard deviation of the composition which is highest for the ferrite phase in FERR. Increased variability in the PREn will lead to variations in the mechanical properties, affecting factors such as Critical Pitting Temperature *(CPT)* and other parameters crucial for assessing corrosion resistance in these metals [8].

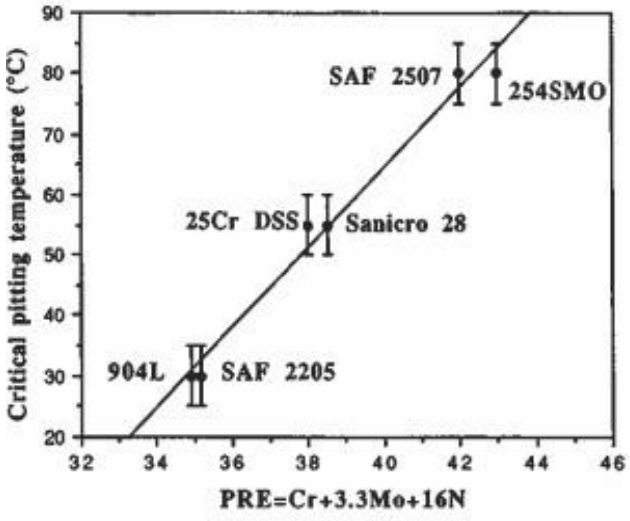

Figure 2: Linear relation between PREn and critical pitting temperature for DSS grade and austenitic steel [8]

The CPT represents the lowest temperature at which stable pits can form. This concept was first introduced by Brigham and Tozer [9] and is widely used to rank the pitting susceptibility of stainless steels. This is discussed in more detail in the proceeding sections.

Figure 2 illustrates the practical utility of the PREn, showing a clear linear correlation between the PREn and CPT. This is valuable as localised corrosion can cause concealed structural damage. Opting for a material with a higher PREn mitigates the risk of material failure in specific environmental conditions [8]. However, a limitation of this parameter is that it

disregards impact of microstructural factors on the initiation of passivity breakdown, through pitting or crevice corrosion [10] [11].

1.1 Localised Corrosion

Mechanism

Corrosion is an electrochemical process that involves the deterioration of materials by oxidation. Under ambient conditions, the oxidation of most metals is thermodynamically spontaneous [12]. In iron, the process involves Fe being oxidised to Fe^{2+} at an anodic site on the surface of the metal. Simultaneously, oxygen is reduced to form OH^- at the cathodic site. Excess electrons from the anodic reaction are transferred from the anode to the cathode through the electrically conductive metal. The formation of rust is the result of oxidation of Fe^{2+} by oxygen, illustrated in **Figure 3**.

The chemical process can be represented by the following equations (4) (5) (6) [13]:

$$2Fe(OH)_3 \rightarrow Fe_2O_3.H_2O + 2H_2O \quad (4)$$

Anodic:

$$Fe \rightarrow Fe^{2+} + 2e^- \quad (5)$$

Cathodic:

$$2H_2O + O_2 + 4e^- \rightarrow 4OH^- \quad (6)$$

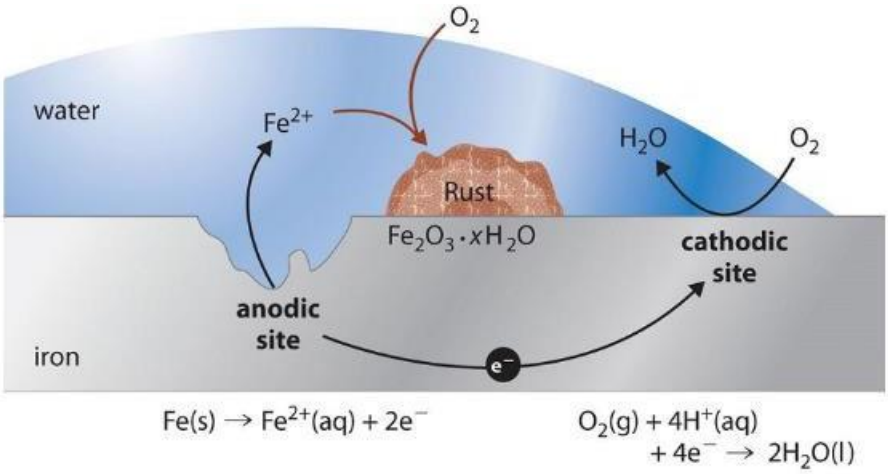

Figure 3: Schematic of corrosion mechanism on iron [13]

The sites that determine the anode and cathode are typically found at lattice defects or impurities. In the case of SDSS, this often occurs at the boundaries between ferrite and austenite grains. As previously discussed, ferrite has a lower PREn, and the ferrite phase tends to become the anode whilst the austenite phase becomes the cathode.

1.2 Passive Oxide Film

Passivity, as defined by ASTM, refers to the state of a metal surface characterised by low corrosion rates, in a potential region that is strongly oxidising for metals [10]. This property is crucial in understanding the corrosion behaviour of metals. Metals like iron lack the Cr content required to form a passive oxide layer resulting in intense dissolution. This characteristic is paramount for corrosion resistance in SDSS. The effectiveness of a passive film varies based on alloy composition and environmental factors. Critical parameters such as density, thickness, porosity and stability of the oxide layer are all linked to the chemical composition of the alloy. Passivation exhibits a decrease in corrosion rate in a dissolving metal due to increased oxidation in the surrounding environment, as the process involves outward diffusion of cations and inward diffusion of anions [14].

Research by Hashimoto *et al.* [15] details the structure of passive films in stainless steel, consisting of an outer iron oxide and an inner chromium rich oxide layer. In acidic environments, oxidised iron tends to dissolve while Cr remains stable, leading to the formation

of a Cr enriched oxyhydroxide passive film. Whilst generally resistant to corrosion, stainless steel can be susceptible to localised breakdown, resulting in accelerated dissolution of the underlying metal. Open surfaces experience pitting corrosion whereas occluded sites can suffer from crevice corrosion. The extent and mechanism of corrosion depends on multiple factors including alloy composition, environmental conditions and electrochemical potential [16].

Stainless steels can exist in three distinct electrochemical states: active, passive and transpassive. Active and transpassive states are associated with uniform corrosion attacks, whilst the passive state is characterised by extremely low corrosion rate, almost approaching zero [17]. The Primary Passive Potential (E_{pp}) is the critical threshold in the context of active-passive polarisation behaviour. Beyond this point, the passive film stabilises resulting in a decrease in corrosion rates. At higher potentials, the passive film can break down, leading to increased anodic corrosion rates in the transpassive state. For stainless steels, this transpassive breakdown occurs near the oxygen evolution potential, where the Cr rich passive film is unstable. Harsh conditions such as acidity and temperature can narrow the passive potential range, elevating current densities and corrosion rates at all potentials [18].

The properties of the oxide film play a significant role in pit propagation. mechanically sound oxide films provide reliable cover for growing pits, whilst weak and stressed films are susceptible to rupture, resulting in repassivation with this mechanism discussed in the next section [19].

1.3 Pitting Corrosion

Pitting corrosion is a specific form of localised corrosion characterised by the dissolution of metal, resulting in the formation of holes within a material. A challenge of pitting corrosion lies in its unpredictability, and it is difficult to anticipate where and when pittingd may occur. Another difficulty is detecting the corrosion as the corrosion products often conceal the damage beneath the surface [7].

There is general consensus that pitting corrosion progresses through several stages: pit initiation, metastable pitting and stable pit growth. The exact factors controlling the process and

a material's susceptibility are subjects of ongoing debate and research [20]. Numerous studies explored various corrosion mechanisms, however prediction of where these events may occur remains unclear. This is due to the processes occurring on a small scale, involving a passive film of only a few nanometres thick and situated on nucleation sites of a similar scale. Additionally, the situation is also dynamic with changing chemistries further complicating the predictability [21].

Mechanism

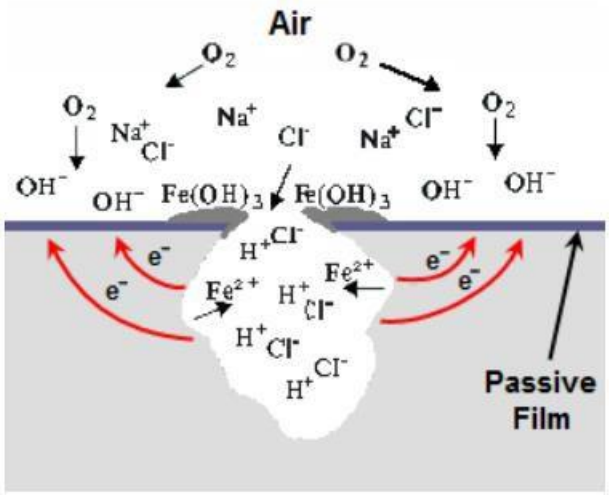

Figure 4: Schematic of pitting corrosion in stainless steel in NaCl solution [7]

Pitting corrosion often begins at surface defects like inclusions or areas where the passive film is damaged. Ongoing debate surrounds whether sulfide inclusions are the most susceptible point for pit nucleation, although other theories suggest that non-metallic inclusions could also play a part. Sulfide inclusions, composed of FeS or MnS, are readily dissolved and create shells around oxide particles, leading to narrow crevices that serve as points where pitting corrosion may begin. It has also been found that sulfides can influence pit formation by acting as local cathodes. [22] Pitting most commonly occurs in environments containing aggressive anionic species such as chloride ions. [22] The high solubility of chlorides ions with metallic cations disrupts the integrity of the passive oxide layer, and the presence of oxidising agents further increases the likelihood of pitting corrosion [22].

Figure 4 illustrates the process of pitting corrosion, beginning where the oxide layer is damaged, resulting in the formation of an anodic site. Iron dissolution then occurs in the presence of water detailed by equation (6). This releases two electrons which are transported to

the cathodic area where they combine with depolarised oxygen and form hydroxyl ions. This reaction is balanced with the reduction of oxygen at the cathode on the surface stated in equation (7) below. This leads to the production of acidic H+ ions within the pit, decreasing the pH and perpetuating the autocatalytic process of corrosion [7] [23].

Pit Initiation

The external surface serves as a distributed cathode area whilst the pit acts as a small anode. This large area difference accelerates the corrosion rate within the pit. In contrast to anodic sites, which tend to be localised in specific regions, cathodic processes can occur anywhere on the surrounding surface. The external surface remains passivated due to higher oxygen levels and a higher pH. However, inside the pit, rapid metal dissolution occurs, leading to an increase in Cl^- ions and acidification of the solution. Oxygen and hydrogen reduction processes take place on the surface, contributing to an increase in the IR drop (decrease in the effective potential applied to the electrochemical double layer). This maintains the potential differences, keeping the pit actively corroding [7].

The production of positively charged Fe^{2+} ions in the pit attracts negatively charged anions like Cl^- ions to the initiation site. Hydrolysis of the Fe^{2+} ions is represented in the equation below:

$$Fe^{2+} + 2H_20 + 2Cl^- \rightarrow Fe(OH)_3 + 2HCl \quad (7)$$

This results in the reduction of the local pH at the initiation site. The acid chloride solution formed accelerates the anodic dissolution, further concentrating chloride ions within the pit. An insoluble cap of corrosion product, $Fe(OH)_3$, accumulates and slows the outward transfer of Fe^{2+} ions. However, it remains porous to chloride ions, sustaining the high acid concentration illustrating the autocatalytic nature of the process. Furthermore, the pit creates a sheltered area that prevents easy transport between the interior and surrounding bulk solution. The anode of the pit is sustained by the reduction of dissolved oxidisers like oxygen on the cathode surfaces [18].

Metastable Pitting

Fluctuations in current often precede the formation of stable pits. These are indicative of formation, early growth and repassivation of initiated pits, suggesting that the passive film undergoes localised breakdown and subsequent repair, restoring the current. The pit nucleation activity is related to the quality of the passive film, whilst the growth and repassivation of pits are determined by the composition of the alloy [24].

Metastable pits are stabilised by the presence of a porous pit cover, serving multiple purposes. This cover provides an ohmic drop that is sufficient to maintain the pit bottom in the active state. It also acts as a diffusion barrier, helping to maintain a concentrated local chemistry. Without this, the surrounding area would be exposed to the aggressive pit environment and general breakdown would proceed. This observation contradicts the definition of pitting potential, as metastable pits can initiate and grow at potentials well above the threshold [16] [24].

Metastable pitting can be observed through drops in potential, reflecting initiation, growth and passivation of a micropit. These transients occur at potentials below the pitting potential but above the CPT. It has been proposed that an anodic salt film, such as $FeCl_2$, passivates pits below the CPT and stabilises pit growth above the CPT. Pistorius and Burstein [25] found that the rate of growth of individual corrosion pits is primarily controlled by the diffusion of dissolving metal cations from the pit interior. The surface of which is saturated with metal chloride independent of electrode potential. Pit growth occurs when no cover is needed for continued pit propagation and the pit depth is a sufficient diffusion barrier in itself. If the cover is lost prematurely, the pit solution is diluted and repassivation occurs. Shallower, more open pit sites are activated at higher potentials and current densities, making them more likely to achieve stability [26].

The early stages of pit growth typically occur in a hemispherical mode, with the pit contents protected by perforated remnants of the passive film. As the pit grows and reaches a critical size, the pit cover is destroyed causing an ineffective diffusion barrier, leaving an open hemispherical cavity. This is an unstable shape and under anodic diffusion, transitions to a

saucer-shaped form. The parts of the pit nearer to the bulk solution have shorter diffusion lengths, resulting in lower interfacial cation concentrations near the edges of the pit compared to the bottom. This initially hemispherical cavity passivates near the mouth whilst further dissolution undercuts the passivated material, shown in **Figure 5**. Ions diffuse out of the created hole and the surrounding material continues to passivate, allowing the continued growth of the pit. This is a cyclic process and is essential for providing a stable cover for early metastable pit growth [27].

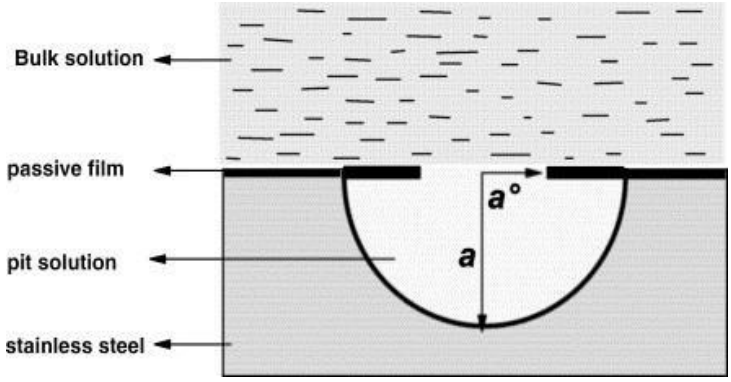

Figure 5: Schematic of metastable pit growth due to porous pit cover [26]

Pistorius and Burstein's research [28] further found that the radius of a metastable pit when the cover ruptures is nearly independent of the current density by which the pit initially grows. This implies that the likelihood of a metastable pit developing into a stable pit after the cover ruptures, increases with higher applied potential.

The nucleation of corrosion pits on stainless steel in chloride solution, under constant potential, can be observed through minute current transients. Nucleation of the pit is a sharp and microscopically violent event. Many metastable pits die through repassivation while still in the metastable growth state. It's important to note that metastable pits which do not achieve stability are not structurally damaging in themselves, although they can affect surface finish on a microscopic scale. All pits, regardless of whether they proceed to stable growth, begin in the metastable state. Some nucleation events result in no observable propagation, indicating that not all nucleation events lead to formation of a metastable pit [28] [29] [30] [31].

The rate of pit growth varies depending on the applied potential. At higher potential, pit growth is controlled by the diffusion of metal ions from the internal pit surface to the external

electrolyte. At lower potentials, evidence suggests a combination of activation and ohmic control. When the pit is small, the diffusion rate is predicted as rapid although in practice, this isn't observed due to the presence of the perforated cover, mentioned previously, over the propagating pit. Pit growth is then controlled by diffusion of metal ions through flaws in the cover into the bulk electrolyte. As the pit expands beneath the cover, it becomes structurally weaker. When the cover ruptures, the diffusion rate increases, accelerating pit growth. This behaviour can be observed as a series of discrete jumps in the transient current, arising from the propagation of individual corrosion pits at a constant potential. The characteristics of metastable pit growth are therefore linked to the behaviour of the protective cover. The potentiostatic pit current transient can be seen as a stepwise rise in current as the metastable pit propagates. The horizontal portion corresponds to the constant pit current under diffusion control through a flaw of constant size, while the vertical portion signifies the current increase by expansion of the flaw size [1] [32] [33] [34].

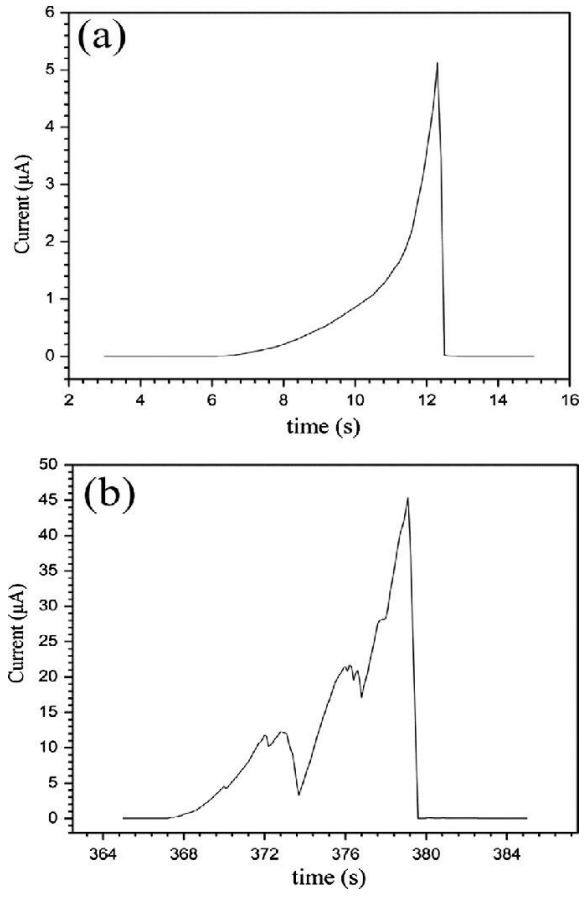

Figure 6: Metastable pitting behaviour of 304 stainless steel in 3.5% w/v NaCl solution. (a) is a peak current transient from a metastable pit, no pit nucleation. (b) is fluctuations in current from activation and passivation of pitting [35]

The top graph *(a)* in **Figure 6** shows a peak current transient resulting from the growth of a metastable pit, where no pit nucleation occurred. In this case, metal dissolution was not stable and the pit repassivated, indicated by an abrupt drop in current back to background levels Activation and passivation of pitting occurs simultaneously during corrosion, producing fluctuations shown in the bottom graph *(b)* in **Figure 6**. The current exhibits rises from anodic dissolution inside the pits during metastable pitting, and subsequent drops associated with pit repassivation after a short period of propagation. The relationship between these fluctuations and time is approximately proportional to the square of time, indicating that diffusion of corrosion products plays a significant role in controlling metastable pit growth [35].

Stable Pit Growth

The stability of corrosion pits depends on the maintenance of local aggressive ions and a low pH within the pit cavity. This environment encourages metal dissolution and prevents repassivation. The acidity inside the pit amplifies due to hydrolysis of the dissolved metal ions. When the rate at which metal ions exit the cavity is slower than their production rate, the metal ion content and local acidity of the pit cavity is maintained, facilitating continued growth of the pit. Conversely, if the metal ions are transported away then the aggressive environment cannot be maintained, resulting in repassivation [36].

Whilst many aspects of pit stabilisation remain unclear, there is consensus that pit stability requires the presence of an aggressive pit environment, and this must be consistently sustained in order for pit growth [37].

Potentials of Pitting

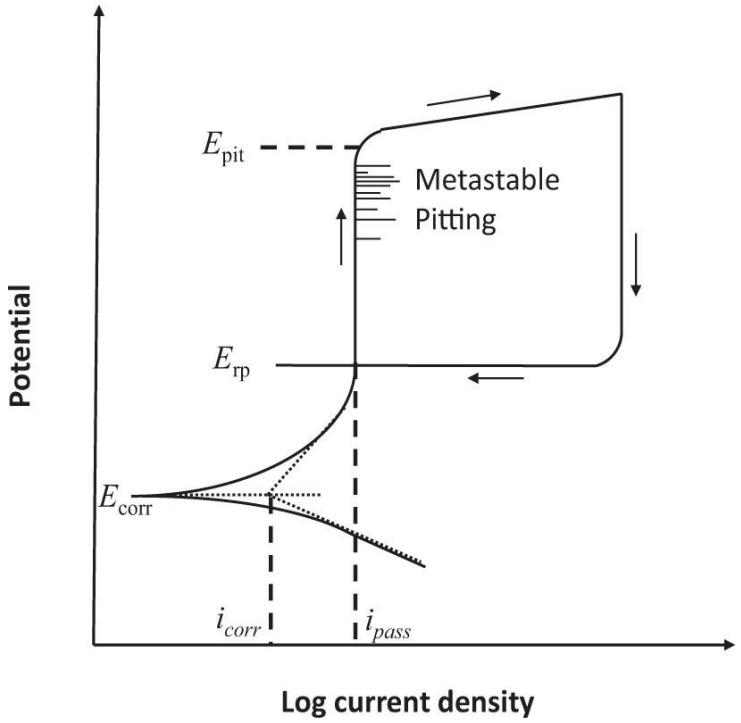

Figure 7: Cyclic polarisation curve [38]

The three stages of pitting can be visualised on a cyclic polarisation curve, seen in **Figure 7**. Between the Corrosion Current Density (i_{corr}) and Passive Current Density (i_{pass}), only metastable pitting can occur. When the applied potential becomes more noble than those specific values, the passive film breaks down and the rapid increase in current density indicates stable pit formation. This point is known as the Pitting Potential (E_{pit}), representing the potential at which the pit solution composition becomes aggressive enough to locally destabilise the passive film, preventing repassivation. It also can be the minimum potential for metastable pits to transition to stable pits. When reversing the scan direction, the Repassivation Potential (E_{rp}) value can be determined when the current density drops, indicating repassivation of the pit. For stable pits to form, the potential must be higher than the E_{pit}, but can only propagate at potentials beyond E_{rp}. It's worth noting that metastable pits can form, and already existing pits can propagate beyond E_{rp} with higher values of both suggest greater resistance to pitting corrosion [38] [39]. Below the CPT, the current density needed to sustain the pit environment is greater than that required for passivation and thus all metastable pits repassivate [24].

Morphology of Pits

In pit morphology, larger pits often deviate from perfect hemispheric shapes and tend to be dish-shaped. This is attributed to the porous pit cover as the edges have lower diffusional resistances and dissolve more rapidly. Frankel [20] proposed that the high resistance was initially provided to pits by the pit cover, rather than by a salt layer. It was suggested that only the pits that survived long enough to precipitate a salt film became stable, whilst others repassivated when the covers ruptured and the ohmic barrier was lost. If a salt film is present when the cover breaks, it is presumed to thicken and accommodate additional potential, maintaining pit stability [40].

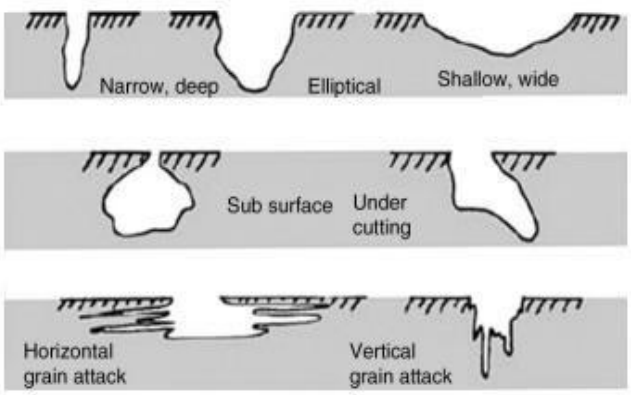

Figure 8: Typical pit morphologies [41]

Various factors including precipitation, segregation, cold work and heat treatments can affect size and distribution of pits [18]. **Figure 8** shows the typical pit morphologies observed in stainless steel corrosion. These can vary with some displaying flat walls which reveal the metallic structure, with other exhibiting irregular shapes. These can be classified as trough or sideways pits, with the cavities being filled with corroded product, forming caps commonly referred to as lacy pits [23]. These have been discussed in previous sections as the lace-like cover over large pits which eventually dissolve or rupture [42].

1.4 Crevice Corrosion

Crevice corrosion occurs in occluded spaces containing solution where the passive film is defective or weakened. It is a result of disparities in oxygen or metal ion concentration outside the crevice. Much like pitting corrosion, crevice corrosion accelerates the corrosion rate and is commonly known as 'differential aeration'. It is a common and detrimental form of localised corrosion in stainless steel [43].

Crevice corrosion shares similarities with pitting corrosion, such as an increasing likelihood with rising potential and chloride concentration. It also exhibits a CCT, like the CPT, representing the potential required for crevice corrosion initiation. The ranking of alloys in terms of crevice corrosion resistance aligns with their performance in pitting corrosion. Alloying elements like Mo are believed to influence both types of corrosion. Research considers pitting as a form of crevice corrosion and view corroded crevices as large pits. Wood *et al.* [44] declared that crevice corrosion is no more than 'lateral pitting' occurring within an occluded area. It has been suggested that structural heterogeneities, which influence pitting, may also impact crevice corrosion. Manganese sulfide inclusions have been identified as initiation sites for metastable pitting that can transition to stable pits. These sites can then act as initiation sites for crevice corrosion [24] [45].

Crevice corrosion can be split into initiation and propagation stages. Initiation referring to the transition from passivity to corrosion within the crevice with development of an aggressive local chemistry. Meanwhile, propagation refers to the rate of metal dissolution and the factors controlling it [24]. Crevice corrosion is relatively easier to initiate than pitting due to the longer diffusion length and smaller anodic current densities required [46]. In a study conducted by D. Han *et al.* [47], experiments were conducted to ascertain the CCT of SAF. The results indicated that crevice corrosion can be effectively prevented when the operating temperature remains below the CPT.

Fontana Greene Mechanism

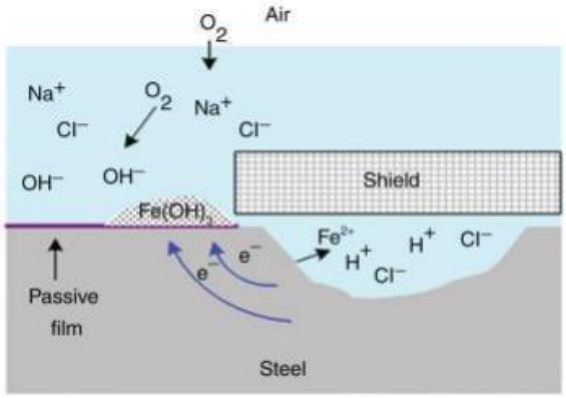

Figure 9: Fontana Greene corrosion mechanism of steel in NaCl solution [41]

The passive dissolution model proposed by Oldfield and Sutton [48] refers to the mechanism of crevice corrosion in stainless steel within aerated, neutral chloride solutions. Initially, both anodic dissolution and cathodic oxygen reduction reactions occur inside and outside the crevice area. As the original oxygen present in the crevice is depleted, the crevice becomes the local anode, with the passive current balanced by oxygen on the surface. Metal ions produced within the crevice gradually diffuse and migrate out, with the hydrolysis of these leading to progressive decrease in pH within the crevice. Similar to local acidification of pits, this leads to the migration of Cl^-ions into the crevice, developing an aggressive local solution. When the crevice environment reaches a Critical Crevice Solution (CCS), the passive film becomes unstable and breaks down, initialisation corrosion within the crevice. Microscopic examination shows micro-pitting and the coalescence of these pits results in general corrosion.

CCS and IR Drop Mechanism

Two widely accepted mechanisms for crevice corrosion are CCS and IR drop mechanisms. Alterations in the chemical and electrochemical environment occur within the crevice in both mechanisms, including decreased dissolved oxygen concentration, enrichment of H^+ and Cl^- ions, negative potential shifts and increases in anodic dissolution current. The CCS theory proposes that changes in the chemical environment leads to crevice corrosion, which subsequently alters the electrochemical environment. The IR drop mechanism suggests that

changes in the electrochemical environment initiates crevice corrosion, subsequently altering the chemical environment. Detailed flows of these mechanisms can be seen below in **Figure 10.** The geometry of the crevice, such as length, crevice gap and electrode area ratio, has major influence on the chemical and electrochemical environment. The gap and length can impact the distribution of dissolved oxygen, H^+ and Cl^- concentrations, whilst crevice gap can affect potential and current distribution. The electrode area ratio can influence the rate of acidification of the crevice solution [45].

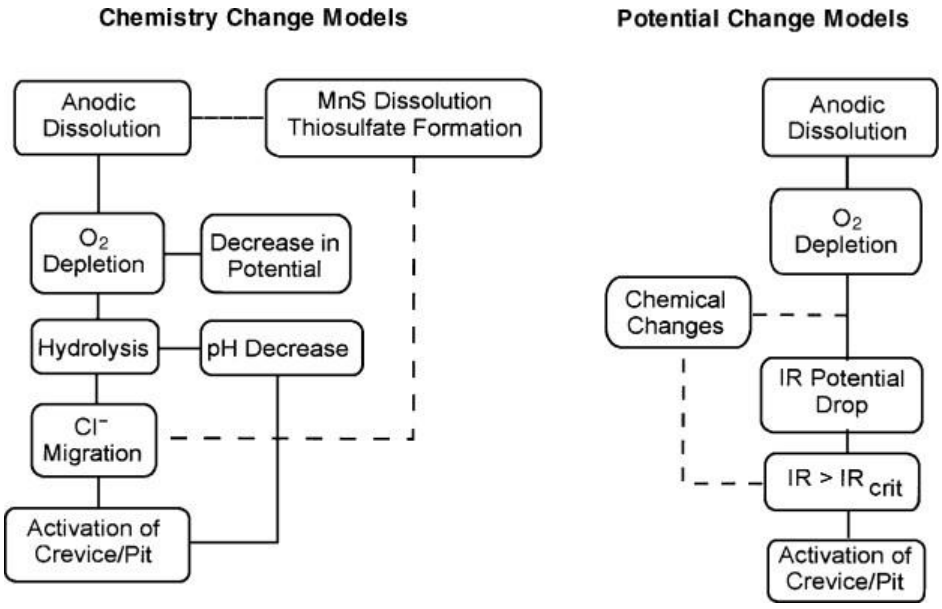

Figure 10: Two sequences of chemical and potential processes that have been suggested to result in initiation of crevice corrosion [49]

Other studies [50] found that the pH does not steadily decrease over time but decreases abruptly after an increase in current, indicating the onset of stable crevice corrosion. Chloride concentration shows a similar pattern, increasing rapidly after corrosion initiation. This implies that crevice corrosion induces a change in crevice solution chemistry rather than a gradual change of local chemistry leading to crevice corrosion. This is contradictory to the CCS theory which predicted a reciprocal relationship [24]. As the corrosion development process is determined by the potential and current density distribution within the crevice, it must follow the IR drop mechanism. The crevice gap determines the H^+ and Cl^- enrichment as well as the potential and current density distribution, thus is the dominant factor for the development mechanism of crevice corrosion [46].

The general consensus in crevice corrosion research addresses the sequence of events as a specific progression: anodic dissolution to oxygen depletion, followed by hydrolysis and a drop in pH. Migration of chloride ions then occurs into the crevice, forming the critical crevice solution that triggers depassivation and active corrosion. Lott and Alkire [51] proposed an alternative perspective, that the dissolution of MnS inclusions inside the crevice generates thiosulfate ions, which, in combination with Cl^-, cause depassivation. This mechanism doesn't require a prior drop in pH but rather initiates crevice corrosion as a result of specific crevice conditions.

The potential change hypothesis suggests a different course of events: anodic dissolution, followed by oxygen depletion which leads to a gradient of potential due to IR drop. When reaching a critical value, it prompts a transition from the passive regime to the active passive peak. For SS, the active passive peak is primarily observed in highly acidic conditions. Therefore, the potential change model must also rely on changes in the crevice chemistry before crevice corrosion activation. Under potentiostatic conditions, this model implies that crevice chemistry transforms first, followed by an increase in current [49].

Crevice Initiation

Pickering [52] observed that an initial attack in crevice corrosion often appears as pitting events on the crevice bottom. The corrosion products formed within the pits accumulate in the confined crevice geometry, increasing the solution's resistance alongside the crevice. It was reported that a significant increase in anodic current due to pitting was not observed, implying that only metastable pitting on the exposed surface could be responsible for current transients. At higher temperatures, anodic metal dissolution within the crevice may suppress the initiation of metastable pitting on the surface, resulting in indistinct current transients. Stockhert and Bohni [53] established a direct relationship between crevice corrosion susceptibility and the occurrence of metastable pitting events. Laycock [24] noted that metastable pitting can be stabilised in the presence of a crevice, suggesting that, like pitting, is influenced by geometry.

Wilde and Williams [49] established a difference between Pitting Potential (E_p) and Repassivation Potential (E_r) and susceptibility to crevice corrosion for various alloys. It was

found that the larger the $E_p - E_r$ difference, the more susceptible the alloy is to crevice corrosion.

Tafel's Law offers explanation for susceptibility of alloys to crevice corrosion in NaCl solutions, particularly under conditions where the metal exhibits a pitting potential. It encompasses salt film formation, electrochemical kinetics governing pit propagation, and the mechanism by which Mo improves pitting corrosion resistance of stainless steels. [54]

Crevice Propagation

Galvele [1] proposed a criterion, known as the stability product (IA), to estimate the transition of metastable pits to stable ones. The model doesn't impose any restriction of the crevice length, A, so the value is applicable for both pitting and crevice corrosion. As previously discussed, the crevice gap has a significant effect on crevice corrosion susceptibility, but there is no criterion for pits developing within a crevice, unlike Shoejaei's findings [55]. Reducing the crevice gap is shown to decrease the time required to attain pit stabilisation. It is evident that non-creviced specimens exhibit the highest metastable stability product, suggesting that metastable pits formed in the absence of a crevice are more likely to transition to stable pits, than those formed within crevices of different gap sizes.

Shoejaei [55] discovered that an increase in current following pit formation amplified the IR drop, and intensifies the acidification of the crevice solution. Both the IR drop and critical crevice solution can influence the propagation stage of crevice corrosion.

Nishimoto *et al.* [56] measured pH and chloride concentration within a crevice, revealing a sharp pH decrease and a significant increase in Cl^- concentration. Shoejaei's work [55] found that no obvious corroded area was observed where pitting was not initiated, suggesting that stable pitting must occur before crevice corrosion development. This is crucial as with pitting, the rate of metal ions dissolving from the passive film would not lead to sufficient acidification of the crevice solution. Prior studies [25] [57] [58] [59] confirm this as tighter crevices are found to make alloys more susceptible to crevice corrosion.

If the diffusion is limited out of the pit, then the metastable pit can stabilise even if it would not have propagated on an open surface, referred to as geometrical stabilisation. The current density required to stabilise the pit within the crevice is lower than that needed to stabilise a metastable pit on an open surface. This is the evidence to why the CCT is lower than the CPT [60].

Crevice corrosion is characterised by a gradual rise in anodic current followed by a slow decay back to the passivating level or the continuation of crevice corrosion. A high frequency of anodic current noise indicates many pit nucleation sites within the crevice [61].

1.5 The Effect of Temperature on Corrosion Behaviour of SDSS

Temperature plays a pivotal role in corrosion processes and is well known in its significant influence on behaviour in both pitting and crevice mechanisms similarly. At low temperatures, alloys exhibit high breakdown potentials. As these temperatures are below the alloy's CPT or CCT, corrosion is unlikely even if external factors that typically influence the corrosion rate are present, such as $NaCl$ concentration [47].

As the solution temperature increases, distinct changes in corrosion emerge. Research [47] with SAF 2205 in a 4% $NaCl$ solution at temperatures from 20 °C to 60 °C, found that resistance to corrosion decreases as the solution temperatures rises. It was verified that variations in $NaCl$ concentration had no impact on the breakdown potential when the temperature remained below the CPT. During the testing process, the microstructure of the sample was periodically examined. It was observed that as the temperature increased, the depths of pitting also increased, attributed to the lack of stability in the oxide film.

At higher temperatures, multiple current peaks become apparent below the CPT. These are indicative of the breakdown of the passive film. Once the temperature surpasses the CPT threshold, there is a sudden and continuous increase in current density, indicating the start of stable pitting. Temperature also causes a substantial impact on the composition and structure of the passive film, pivotal in corrosion mechanisms [62]. Furthermore, elevating the temperature shifts the breakdown potential towards more active values, implying that the

resistance to pitting corrosion decreases with rising temperature. The kinetics of pit formation at higher temperatures shows an increased number of pits with alterations in their depth. This suggests that a stronger chemisorption of Cl^- ions onto the metal surface, leading to a higher number of pits distributed on a larger anodic area, impeding the growth in depth [22].

Lauritsen's investigation [63] involved analysis of SDSS alloys within a temperature range of 40 °C to 80 °C. The findings indicated that with rising temperature, the OCP declined. This decrease lowered the pitting potential, resulting in an increased occurrence of pits observed on the surface of the samples.

1.6 Effect of Deaeration & Surface Finish on Corrosion Behaviour of SDSS

Previous research [40] has explored the impact of surface finish on pit formation. Sites which are wider, more open to the environment, require a faster initial rate of reaction in order to achieve diffusion control, which is only obtained at higher potential. Sites which are less open can propagate at lower potential as the diffusion barrier is more easily reached [18]. It has also been found that a coarser finish can lead to the formation of more metastable pits, with a higher likelihood of pits becoming stable due to a lower E_{pit} value. These pits originate at specific sites on the metal surface, such as sulfide inclusions. Most of these nucleation events do not lead to propagation of the pit but instead repassivate and can renucleate multiple times if propagation does not occur. Nucleation is a random mechanism and the frequency decreases over time following first-order kinetics. The surface finish influences the time constant and, in turn, the behaviour of metastable pits or repassivation. A smoother surface makes pit propagation more challenging and allows for more repetitive nucleations from the same site [34] [64].

Burstein *et al.* [29] found that a smoother surface had a greater number of nucleation events due to the same site nucleating multiple times, although they took longer to terminate compared to a rougher surface. Smoother surfaces also tended to have fewer metastable pits as these require a greater number of nucleation events, and the sites are on average more open than a rougher surface. For propagation, a higher chloride concentration or potential would be needed. Corrosion products of Fe, Cr and Ni accumulate in the pit and form very acid chloride

solutions, increasing the corrosion rate needed for pit propagation [18]. If a metastable pit propagates from a given nucleation event and dies through repassivation, the site is killed and cannot renucleate. Conversely, if it fails to propagate, the site remains available for further renucleation and may renucleate multiple times. The probability that propagation follows from a nucleation event is significantly lower for a smoother surface. Potentiostatic data also confirms the discussed research with the frequency of current spikes on a smoother surface greater than that on a rougher surface [64] [65].

It is well established that the pitting potential tends to decrease as the surface roughness of the sample increases, due to the changing characteristics of the sites available for pit initiation. These sites can be associated with MnS inclusions and rougher surfaces provide sites with more occluded geometry. This is then easier to maintain a concentrated local chemistry and support a higher frequency of pit initiation. Many of these pits are metastable but are associated with a lower pitting potential [66].

Furthermore, Y. Tang *et al.* [67] found that rougher samples of DSS exhibited a higher active surface state and a greater likelihood of stable pitting. It was also noted that metastable pit size increased and had a longer lifetime on surfaces of greater roughness.

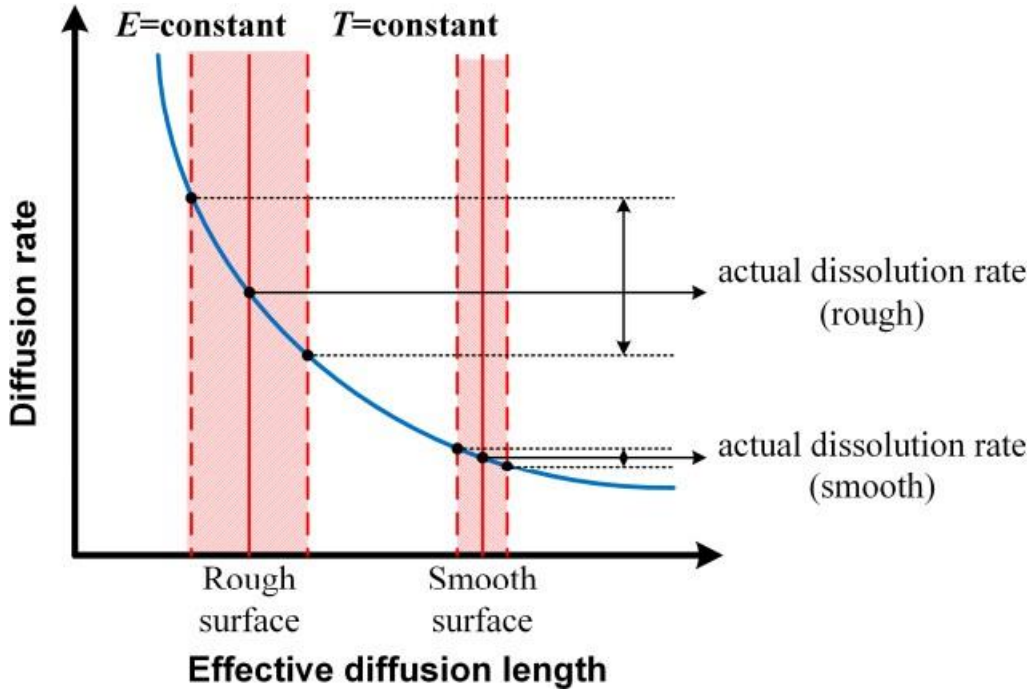

Figure 11: Relationship between surface roughness, effective diffusion length, diffusion rate and actual dissolution rate of metastable pits [67]

Figure 11 illustrates the mechanics of metastable pitting in relation to various surface finishes. The rougher finish shows a longer diffusion length, which increases the probability of sustaining an aggressive environment as the transport of metal cations out of the pit is affected. Consequently, the critical concentration for dissolution is attained faster, as evidenced by the larger area of actual dissolution rate on the rough surface.

Under aerated conditions, the corrosion process occurs as described in equations (4) (5) (6), involving the reduction of oxygen. The presence of an oxidiser increases the corrosion rate into a more active state. When the conditions are deaerated, the cathodic reaction shifts from equation (6) to equation (8):

$$2H_2O + O_2 + 4e^- \rightarrow 4OH^- \quad (6)$$

$$2H_2O + 2e^- \rightarrow H_2 + 2OH^- \quad (8)$$

Both the rate of hydrogen production and corrosion are lower in deaerated conditions but as aeration increases, the reduction of dissolved oxygen dominates, raising the corrosion rate [18].

Research [18] has shown that when steam condensate comes into contact with air, it absorbs oxygen leading to high dissolution of steel. This occurs through the formation of highly aggressive differential aeration cells, seen at temperatures exceeding 50 °C. The bottom of active pits contain black magnetite Fe_3O_4, whilst the surrounding surface exhibits the characteristic red rust colour of Fe_2O_3. In the absence of dissolved oxygen, the magnetite surface film is protective, resulting in uniform and low corrosion rates.

1.7 Microstructure of SDSS

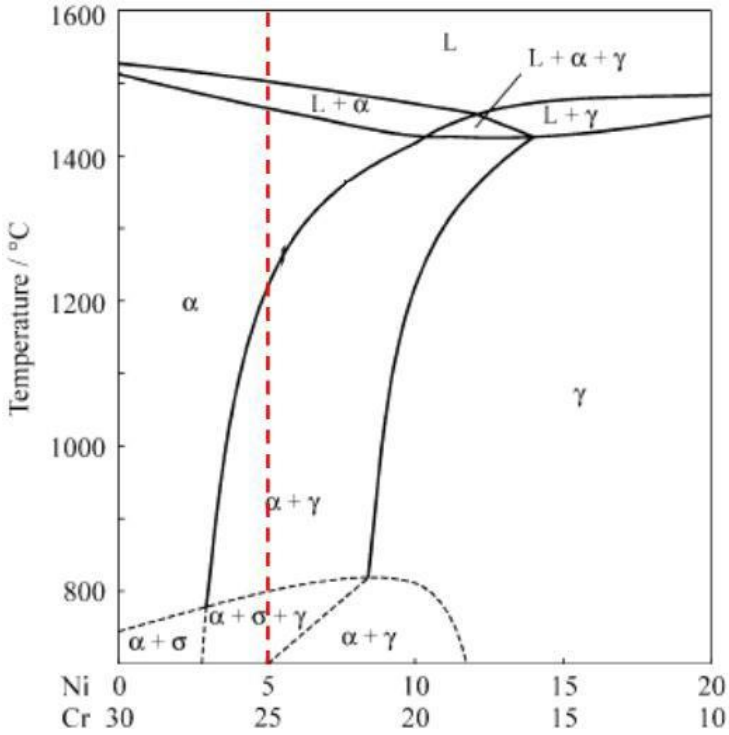

Figure 12: Cross section of Fe-Cr-Ni phase diagram with 70% Fe, red line for phase transformation for the SDSS grades on alloying additions [68]

The aim for SDSS is to have 50% of both ferrite and austenite phases although this is not always achieved in practice. The red line on the phase diagram in **Figure 12** shows the transformation that occurs for the formation on a SDSS alloy. The alloy is solution annealed by heating to high temperatures ~1600 °C to ensure a solid solution. Rapid cooling from this temperature causes

precipitation of the ferrite phase, then transforming to a mixture of ferrite and austenite. The volume of austenite formed in duplex microstructure can vary from 35% to 55% [5].

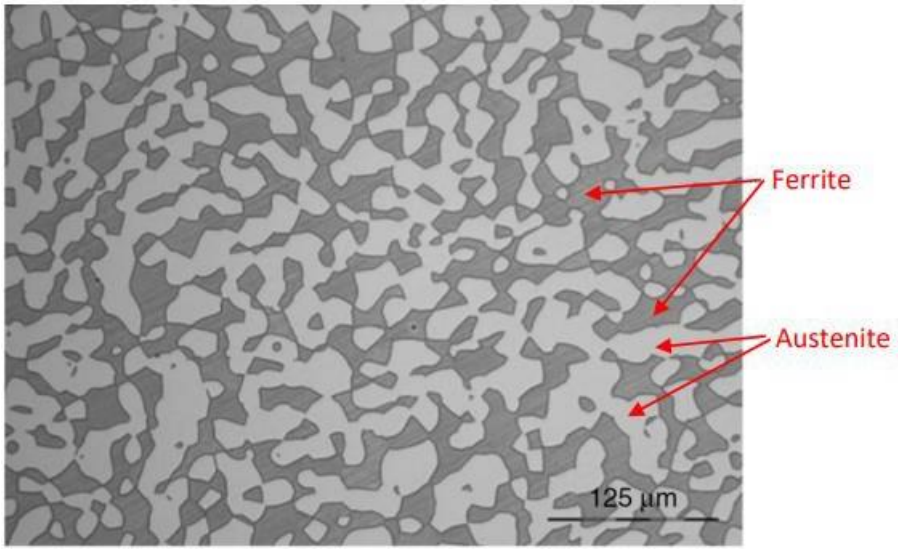

Figure 13: Optical image of solution annealed SAF showing light austenite and dark ferrite phase [68]

Previous work [68] using the same batch of all three grades used in this paper has been undertaken with the specimens etched in a 40 wt% NaOH solution using 1.5 V for 30 s to 40 s. **Figure 13** shows the microstructure of SAF with evenly distributed austenite and ferrite phases highlighted.

1.8 Effects of Alloy Additions

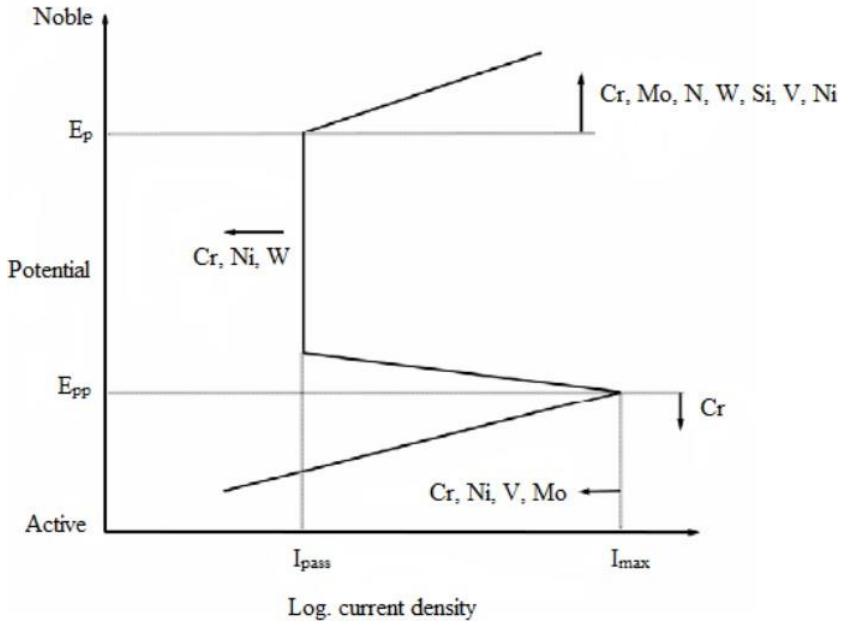

Figure 14: Effect of alloying elements on the polarisation curve of austenitic stainless steel [69]

The corrosion resistance of the alloying elements below is essential and many of them are included in the PREn equations (1) (2) (3) introduced previously.

Chromium

Stainless steel's corrosion resistance originates from the natural oxidation of chromium and iron, leading to the formation of the protective passive film on its surface. The chromium content significantly affects the corrosion resistance as it directly impacts the passive film [70]. As the Cr content increases, so does the resistance to pitting corrosion, with a notable effect up to ~25%. Beyond this, further increases do not produce significant changes [22].

Alloying with Cr also effects the passivation potential by shifting it towards the active direction, expanding the range of passive potential, illustrated in **Figure 14** [10]. Although, there is an upper limit to the Cr content. Exceeding the limit can lead to formation of embrittling phases, reducing the material's toughness, ductility and corrosion-resistant properties [71].

Copper

Copper has only gained interest relatively recently, showing improvements in corrosion performance due to the formation of a copper layer on the surface during corrosion [10]. The mechanism is thought to be through the accumulation of metallic copper on the surface, forming a protective insoluble salt when reacting with chloride ions [68]. This is beneficial in pitting corrosion but also has been attributed to improvements on other methods of corrosion such as stress corrosion cracking and intergranular corrosion [72].

Copper contributes to an increase in tensile strength in DSS through precipitation hardening, as its solubility in ferrite decreases with temperature [4]. It offers a particular advantage in environments such as seawater contaminated with hydrogen sulfide, especially at high flow velocities where cavitation can occur [3]. When alloying with copper, in various solutions, it has been observed that additions can lead to variations in performance. A study conducted by Kivisäkk *et al.* [73] investigated 25% Cr SDSS with varying copper content ranging from 0.02 to 2.01 wt%. It was found that the addition of copper did not have any beneficial effects on the iso-corrosion curves in hydrochloric acid. However, it was noted that the two highest copper content levels did exhibit a lower corrosion limit in this context. Copper impact was found to be beneficial in sulfuric acid, H_2SO_4, solutions. A paper [74] revealed a positive effect on corrosion resistance when examining active corrosion behaviour of hyper-duplex stainless steels. The result saw a decrease in critical and corrosion current densities, along with an increase in polarisation resistance. This enhancement is attributed to the enrichment of the surface film with metallic copper through the selective dissolution of Cr, Fe and Ni as well as the electrochemical dissolution of the corrosion products generated.

Researchers [75] [76] examined how copper influences the corrosion properties of SDSS in varying solution concentrations. Their aim was to investigate whether copper impact on corrosion resistance was due to segregation within the austenite phase. This has been previously discussed where copper increases the PREext of austenite compared to ferrite. Their findings agreed with this theory, showing that the austenite phase exhibited improved resistance to pitting corrosion when compared to the ferrite phase.

The optimal copper content depends on the Cr content, although are typically maintained at ~2 wt% as beyond this limit can reduce ductility and detrimental phase formation [3] [68]. This also correlates to the experiments Roscoe *et al.* [71] conducted in 3% $NaCl$ solution at 30 °C, which found that with an increase in copper wt% resulted in significant decrease in pitting current density, which levelled off at levels of 2% wt% Cu in the alloy. Additional investigations [63] into localised corrosion properties of high tungsten SDSS, ZER in this paper, observed interesting behaviour when exceeding 4.5 wt% Cu. A phase enriched with copper formed at the boundaries between ferrite and austenite phases. This triggered localised corrosion to initiate at these grain boundaries which increased with longer isothermal heat treatment times.

Manganese

Whilst manganese can have a detrimental impact on pitting resistance when considered as a single element, its effects are more beneficial when combined with Mo and N, exhibiting higher pitting potentials. Mn content needs to be maintained at low level, ~0.5 wt%, as this helps prevent the preferential formation of chromium sulphides, which increase the likelihood of pit initiation [10] [71].

Molybdenum

Molybdenum's effectiveness in stainless steel corrosion resistance is closely related to the presence of Cr. It stabilises the oxide film and shifts the pitting potential in the noble direction, inhibiting the breakdown in passivity, seen in **Figure 14**. At certain levels of addition, stable pitting can cease altogether as passivation occurs within the pit itself [40]. Similar to Cr, there is a limit to Mo additions, not exceeding 4 wt% as beyond this threshold it can lead to detrimental phases formed in the microstructure, reducing ductility [3]. Additionally, Mo slows the growth kinetics of pitting by reducing the current density at the pit surface. This reduction decreases the likelihood of a micropit transitioning from a metastable pit to a stable one [58]. It has also been observed to bond with sulfur and dissolve, mitigating adverse effects of sulfur, such as sulfide inclusions [16].

There is a proposed mechanism where Mo forms a passive MoO_2 film, which decreases the active dissolution current. This is achieved by eliminating active surface points through the

formation o f Mo oxides or oxyhydroxides at locations where the stable passive film is compromised [14] [15].

In the contrast of crevice corrosion, Roscoe [71] conducted experiments in 3% $NacCl +$ 0.05 Na_2SO_4, aerated at 90 °C for 30 days. It was observed that the minimum mass loss hovered around 3-4% but increased beyond this, up to 5%.

Nickel

Nickel stabilises austenite in the microstructure, crucial with high concentrations of Cr and Mo which are added into the composition to compensate for the low wt% of C content. It offers a good balance of strength and ductility, although excessive additions can cause the austenite proportion to exceed 50% of the structure. This increases susceptibility that residual ferrite with transform into the brittle sigma phase at lower temperatures, resulting in adverse effects on toughness and weldability. Even if the ferrite transformation is avoided, higher austenite % leads to inferior strength and pitting resistance. Conversely, insufficient nickel content can lead to low toughness through the formation of delta ferrite during solidification, which is also associated with reduced ductility linking to grain size [3].

To achieve optimal pitting resistance, it is recommended that the nickel content keeps within the 4-8 wt% range when in a 25% Cr material. This enhances the pitting potential by extending its passive range, shown in **Figure 14**. A study by Roscoe [71] observed that in 3% $NaCl$ + 0.05 Na_2SO_4, aerated at 80 °C for 30 days, a nickel content of 6-6.5% resulted in the minimum mass loss of the stainless steel samples examined. Beyond this range, the mass loss increased significantly.

Nitrogen

Nitrogen is also another element that shifts the pitting potential in the noble direction, depicted in **Figure 14**. The benefits are enhanced when in presence on Mo, which extends the noble range to the maximum possible for a Cr protected alloy. These advantages require a high level of manganese to ensure the solid solubility of nitrogen in austenite containing Cr [10]. A

mechanism has been proposed involving N forming carbonitrides and subsequently reducing pitting corrosion. This is particularly effective as pitting corrosion often initiates at the boundaries of carbide inclusions. Steels containing higher N content tend to have passive films with higher concentrations of both Cr and Mo stabilising the film. Nitrogen has been shown to segregate to the metal oxide interface, forming a stable interstitial nitride phase which acts as a kinetic barrier against dissolution [77] [78].

Furthermore, it has also been seen that N compensates for the pH drop within pits from the H^+ reacting by forming NH^{4+} (ammonium) and NH_3 instead. The addition of Cr and increased pH in the pits from the N enhances passivation and passive film properties [77].

Tungsten

Tungsten has demonstrated significant improvements to localised corrosion resistance and can be attributed to several factors. Studies have shown that the CCT and the temperature at which crevices repassivate increase with rising W content, with improvements up 10 °C at 2.1 wt%. This is due to W promoting the stability of Mo, Cr and Fe in the passive film by the formation of tungsten oxide and nitrides. The compounds positively affect the band gap energy of the layer, increasing corrosion resistance. Materials containing W show no chromium depletion and lower dissolution of Fe when compared to W-free materials, stabilising the passive film further [79]. The presence of tungsten trioxide, WO_3, within the passive film acts as a barrier, preventing anion attack and cation ejection. Tungsten anions have also been reported to act as inhibitors in the electrolyte inside pits and crevices [80].

The additions of W are intentional for its benefits, despite its higher cost in comparison to Cr and Mo [81]. Szklarska-Smialowska [82] also found a synergistic effect between W and Mo, where a certain ratio leads to peak corrosion performance. According to Kim *et al.* [83], the optimal corrosion performance is achieved when using a W to Mo ratio of 2:1.

In their study, Haugen *et al.* [81] determined the CCT for two SDSS grades, FERR as well as an alloy enriched with tungsten, in 3.5 wt% $NaCl$ at pH 8. Crevice corrosion was observed in

FERR within the temperature range of 50 °C to 60 °C, whilst the tungsten-enriched alloy exhibited crevice corrosion at a much higher temperature, ~85 °C.

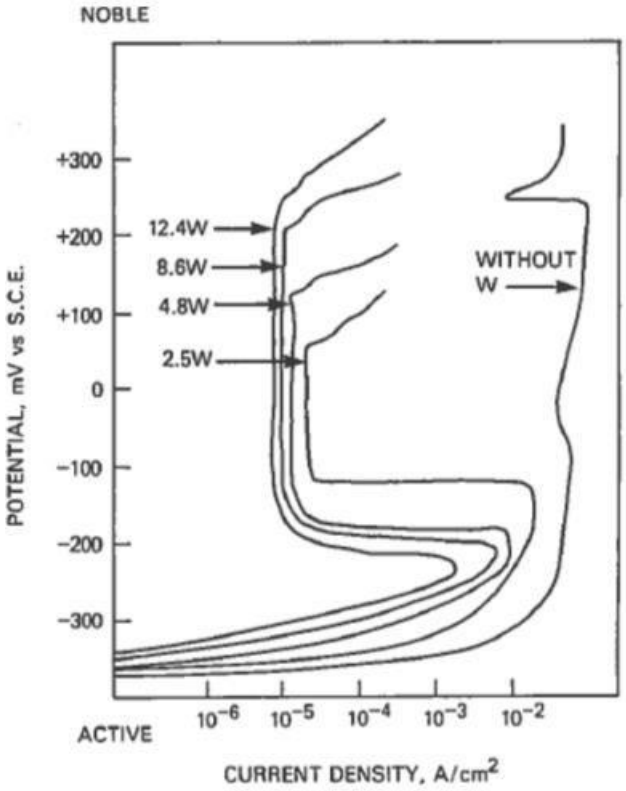

Figure 15: Effect of tungsten on polarisation curve in SDSS [5]

Tungsten is also another element that extends the passive potential range, seen in **Figure 14** and increases the passive potential whilst decreasing the passive current density, as shown in **Figure 15**. Anodic Critical Pitting Potential measurements have shown that *W* increases the CPT when comparing stainless steel grades with varying *W* additions. In the study conducted by Haugen *et al.* [81] on the influence of *W* in 25Cr SDSS, it was discovered that ZER had a CPT approximately 15 degrees higher than FERR (Cu+). W was also observed to promote pit repassivation kinetics whilst delaying the formation of undesirable phases. Instead, it precipitated into less detrimental phases such as the intermetallic x phase. This change in microstructure reduced the volume fraction of unwanted tertiary phases, leading to an improvement in corrosion resistance.

Studies have proven that *W* is adsorbed in the passive film without modification of the oxidation state. In acid chloride solutions of low pH, it is thought that *W* passes directly from the metal

into the passive film, interacting with water to form insoluble WO_3. In neutral chloride solutions, the beneficial effect of W is through its interaction with other oxides, resulting in enhanced stability and bonding of the oxide layer to the base metal [84].

It has also been found that the addition of 2 wt% W reduces the total concentration of deleterious phases and slows down precipitation. However, an addition of only 0.6 wt% produces an opposite effect in promotion of deleterious phases, negatively impacting localised corrosion [79]. This also correlates to the experiments Roscoe *et al.* [71] conducted in 3% $NacCl + 0.05\ Na_2SO_4$, solution at 80 °C, which found that the immunity potential to crevice corrosion increased linearly and increasing W content, up to 1.5 wt%.

Other Elements

Other alloying elements, such as vanadium and silicon, have been shown to widen the passive potential to more noble values, reducing the passive current density. This can be seen in **Figure 15**. Although, silicon content above 1 wt% can enhance sigma phase formation in the microstructure, adversely affecting corrosion resistance [10] [71].

1.9 Mass Loss Estimation Models

Corrosion rate can be directly linked to mass loss and often quantified by two main methodologies: gravimetric analysis and electrochemical techniques. It is essential for comparative studies between metals to choose the most suitable material for the specific application. The choice between the approaches depends on the nature of the research carried out, with time constraints and accuracy being key considerations to either method. An alternative method used in this thesis involves analysing pit and crevice geometries formed during corrosion where the volume of these corrosion features can be calculated.

Gravimetric Analysis

Gravimetric analysis is the predominant method to quantify corrosion rates due to its simplicity and well-established procedures. It involves immersion tests with standardised procedures, where metal samples of known surface area are immersed in a corrosive medium for specified duration of time. After immersion, the mass loss is determined by comparing the weight before and after testing.[85]

Although widely used, this method of analysis does have limitations. It provides an average corrosion rate over the test duration, however, does not account for variations in oxidation kinetics. Inaccuracies may also arise due to excessive removal of corrosion products after testing. Some assumptions taken will lead to errors in the calculations, in that the surface area remains constant throughout the testing, although it is known that the area would change as a function of time as the object dissolves. Additionally, this method would need significant mass change to minimise weighing errors. These are typically achieved through long exposure times, which is not suitable for experiments requiring shorter durations. [86]

Electrochemical Analysis

Electrochemical methods are used due to their ability to monitor electrical parameters during corrosion. Corrosion reactions involve transfer of charge, producing electrical current.
Faraday's Law, one of the key principles in electrochemistry, relates electrical charge transfer to mass loss. It states that the amounts of electrical changes produced by the same quantity of electricity are proportional to their equivalent weights and is written by the equation:

$$M(mg) = \frac{Q}{n*F} * A \quad (9)$$

Where M represents mass loss, Q denotes the total electric charge transferred, n signifies the number of moles of electrons, F is the Faraday constant and A represents the surface area.[87][88]

This method provides insights into real-time monitoring of corrosion kinetics with accurate data collection through a complex instrumentation setup. However, it relies on the assumption that only a singular corrosion mechanism is active at one time.

Pit Geometry

Mass loss can also be estimated using measurements taken from the pits and crevices formed during corrosion. Although using accurate data measurements, assumptions have been incorporated into these calculations by using idealised shapes, such as hemispherical pits and uniform cylindrical crevices. The morphology of pits has previously been discussed and Akpanyung and Loto [23] found that typical morphologies vary and other exhibit irregular shapes. Therefore, these simplified estimations would overstate the mass loss calculated.

Using the volume of a sphere, this can be halved to find the volume of one pit, used to find the total pit volume and then the total mass loss by the equations below.

$$V(one\ pit) = \frac{(({}^{4}/_{3}) * PI * (average\ pit\ depth(r)^{3}))}{2} \quad (10)$$

R obtained using the diameter.

Total pit volume can then be approximated by equation (11):

$$Total\ pit\ volume = V(one\ pit) * number\ of\ pits \quad (11)$$

and in turn can be used to calculate the overall mass loss by equation (12):

$$M(mg) = total\ pit\ volume * density \quad (12)$$

The calculations to estimate mass loss for crevice corrosion are similar to pitting corrosion. The crevice depth is used to calculate the volume of half a cylinder by the equations below, see **Figure 16** for visualisation.

$$Area\ (m^2) = \frac{Pi\ x\ r^2}{2} \quad (13)$$

R obtained using the diameter.

The circumference (C) calculated by equation (14):

$$C = Pi\ x\ 2\mathrm{r} \quad (14)$$

Calculate the volume of the crevice by equation (15):

$$Volume = Area\ x\ Circumferenc\mathrm{e} \quad (15)$$

Mass is found using the density of iron into the equation (16):

$$Mass\ (kg) = Volume\ x\ Density \quad (16)$$

Then changed into grams by equation (17):

$$Mass\ (g) = Mass\ (kg)\ x\ 1000 \quad (17)$$

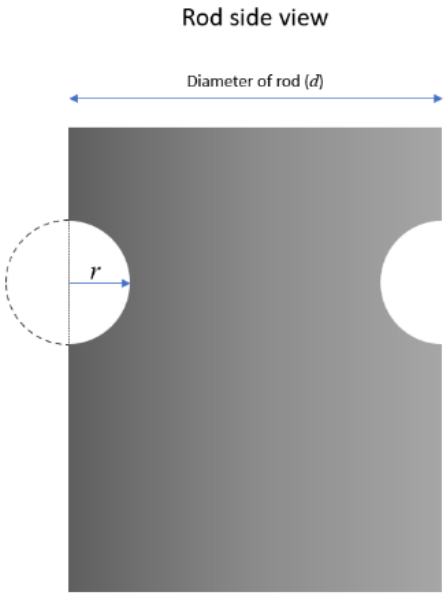

Figure 16: Schematic visualising side view of the rod for mass loss calculation

Aims & Objectives

- A comprehensive assessment of pitting corrosion will involve quantitative analysis, focussing on parameters such as CPT and the frequency, area and depth of dissolution. This will be conducted through potentiostatic polarisation techniques in a 3.5% w/v $NaCl$ environment, with temperatures incrementally increased using a controlled ramp rate. This approach will provide valuable insights into the pitting behaviour of SDSS and the roles of Cu and W on the composition. Additionally, the impact of temperature, deaeration and surface finish on the behaviour of SDSS will also be discussed.

- A comprehensive assessment of crevice corrosion will involve quantitative analysis, focussing on parameters such as CCT and the depth of dissolution. This will be conducted through potentiostatic polarisation techniques in 3.5% w/v $NaCl$ environments, with temperature held at specific intervals in conjunction with o-rings. This approach will provide valuable insights into the crevice behaviour of SDSS and the roles of Cu and W on the composition. Additionally, the impact of temperature on the behaviour of SDSS will also be discussed.

- Based on the data gathered from previous experiments, two mass loss models will be employed: Faraday's Law and Pit Geometry. These models will be utilised in comparison to assess their accuracy and determine if the calculated mass loss aligns with the data collected in the experiments.

2.0 EXPERIMENTAL PROCEDURE

Materials

Three grades of Super Duplex Stainless Steel were provided by Langley Alloys of tradenames, Ferralium 225, SAF 2507 and Zeron 100. Rods of 13 mm diameters and length of 10cm were used. The samples were not mounted to ensure pitting corrosion was the preferential corrosion method.

The composition of each grade can be seen in **Table 2**.

Table 2: Chemical composition of Super Duplex Stainless Steel grades FERR, SAF and ZER [89]

Tradename	Cr	Ni	Mo	N	C	Mn	P	S	Si	Cu	Other
Ferralium 255	24.5 - 26.5	5.5 - 6.5	3.1 - 3.8	0.20 - 0.25	0.025	0.80 - 1.20	0.025	0.005	0.7	1.5 - 2.0	
SAF 2507	24.0 - 26.0	6.0 - 8.0	3.0 - 5.0	0.24 - 0.32	0.03	1.2	0.035	0.02	0.8	0.5	
Zeron 100	24.0 - 26.0	6.0 - 8.0	3.0 - 4.0	0.20 - 0.30	0.03	1	0.03	0.01	1	0.5 - 1.0	W 0.5 - 1.0

Influence of Temperature on CPT and Pit Initiation

Potentiostatic Polarisation

The electrochemical experiments were conducted using a Gamry Interface 1010E with a conventional three electrode setup. A digital programmable hot plate was used to ramp the temperature at a constant rate. A platinum counter electrode, saturated calomel electrode and a sample, acting as a working electrode, were immersed in a beaker containing 3.5% w/v NaCl solution. All solutions were prepared with laboratory grade salt and distilled water. The samples were prepared with 400 grit silicon carbide papers and cleaned with ethanol. The setup was placed on the hotplate with a thermocouple situated near the sample and electrically connected. A schematic of the setup can be seen in **Figure 17**.

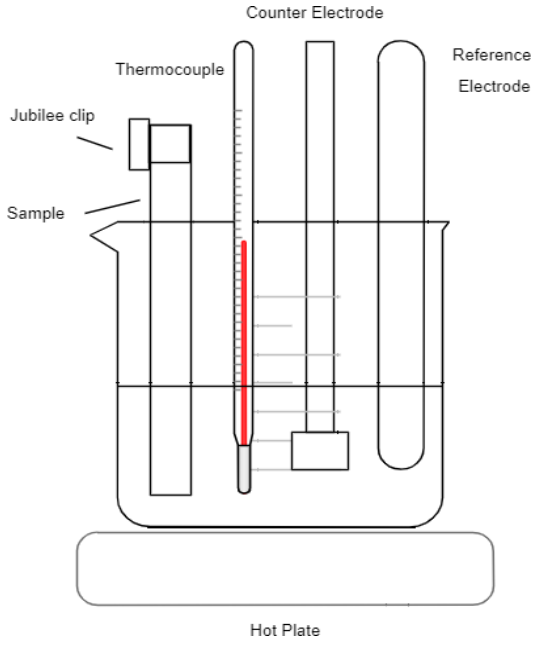

Figure 17: Schematic representation of apparatus set up

Potentiostatic polarisation was performed using a constant potential of 0.9 V vs SCE. These values were chosen from previous potentiostatic experiments ran with the same samples [90]. A sample was placed an exact distance of 2cm into the solution, with an assumption that the as received samples had the same outer surface finish. An Open Circuit Potential (OCP) was run for 10 minutes at room temperature to ensure correct setup. The solution was heated to 65 °C with the ramp set to 40 °C/hour up to 85 °C, with the potentiostat recording starting as the ramp was set. The final temperature was chosen due to the CPT of each sample being below 85 °C, this would ensure each grade would have sufficient corrosion damage. At 85 °C, the sample was taken out of solution and cleaned with ethanol. The typical experiment duration lasted roughly 30 minutes. The experiment was repeated once to ensure results were representative of the alloy behaviour.

Data from the potentiostat was collected as current vs time. Temperature was incorporated by calculating the temperature increase where each data point was measured, every 10 seconds. The temperature increase was assumed constant at each recorded point and for each data set in order for each experiment to be comparable. Current vs temperature graphs were plotted and analysed. According to ASTM G150, the CPT is defined as the temperature at which the current density exceeds 100 $\mu A/cm^2$ for one minute [91].

Analytical Microscopy

The samples were cut using a diamond saw to isolate the corroded end, cleaned using ethanol and analysed underneath a Keyence VHX-7000 microscope. The end face was the only surface to be quantifiably analysed and a stitched image at 150x magnification was produced. Using a maximum grain measurement tool, discernible pits were highlighted. The area of each pit was then calculated by the software using the highlighted area, and the data along with the number of pits was compiled. Depth of the pits were also measured using a 3D depth profile in which the maximum and minimum points of the pit were calculated and repeated for five pits on each sample. Bias was reduced by increasing the magnification and moving irregularly to different points on the sample. Micrographs were also compared to ensure the same pit had not been measured twice. On some samples, five pit depths could not be obtained due to limitations in the technique i.e. lacy pits affecting the light in the pit. The data was compiled and statistically analysed using box plots.

Influence of Temperature on Mass Loss in Aerated Conditions

This section is using the same data collected from the prior experimental section of aerated samples.

Using the current vs time graphs recorded by the potentiostat, charge (Q) was calculated for each sample by integrating under each curve using the trapezium rule below in equation (18):

$$Q = \frac{(x_1 + x_2)}{2}\, x\, (y_2 - y_1) \tag{18}$$

Using Faraday's Law of Electrolysis, mass loss was obtained using the equation (9):

$$M(mg) = \frac{Q}{n*F} * A \tag{9}$$

where Q = charge, n = electrons transferred, F = Faraday's constant and A = atomic weight of Fe. Although each sample's total time under polarisation was different, the time from the initial current increase till the end of each test was ~500s, which allows the charge to be comparable

between each grade. The average mass loss with maximum and minimum values were then calculated for statistical plots to be analysed.

The data obtained from pit depths can be used to estimate mass loss also using the pit geometry. The volume of one pit was calculated by equation (10):

$$V(one\ pit) = \frac{(({}^{4}/_{3})*PI*(average\ pit\ depth(r)^{3}))}{2} \quad (10)$$

R was obtained using the diameter of the samples.

Total pit volume can then be approximated by equation (11):

$$Total\ pit\ volume = V(one\ pit) * number\ of\ pits \quad (11)$$

and in turn can be used to calculate the overall mass loss by equation (12):

$$M(mg) = total\ pit\ volume * density \quad (12)$$

The two methods have been compared and disparities between them discussed.

Influence of Deaeration and Surface Finish on Pit Initiation

The samples from previous research [90] have been analysed in conjunction with the prior section. The samples were prepared and analysed using the same method described in the previous section but with a finer surface finish using 4000 grit silicon carbide papers. The experimental procedure was similar to the method described in the previous section; however, a nitrogen inlet and insulation was used, the pH of the solution maintained at 7 and the ramp rate was 30 °C/hour rather than 40 °C/hour used in the previous method. A schematic of the setup can be seen in **Figure 18**.

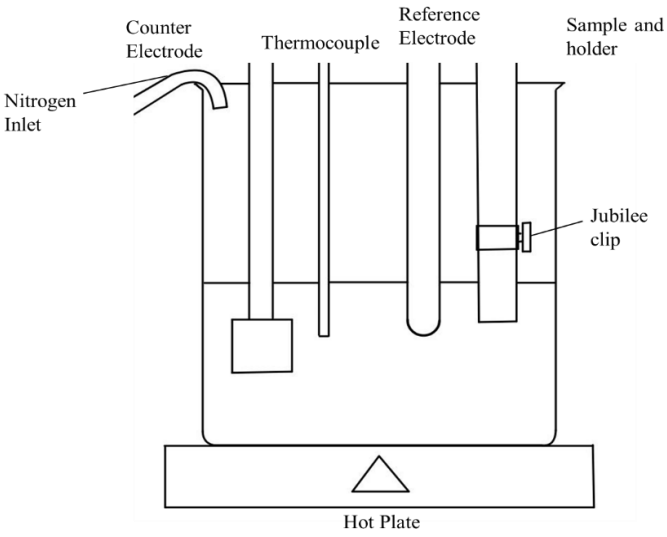

Figure 18: Schematic representation of CPT apparatus set up [90]

Crevice Corrosion Susceptibility of SDSS at Temperature

The same potentiostatic polarisation setup as described in the previous sections was used. An o-ring was placed around the circumference of the rod, 1cm from the end and placed 2cm into the solution, to change the preferential corrosion method to crevice instead of pitting. A schematic of the setup can be seen in **Figure 19**.

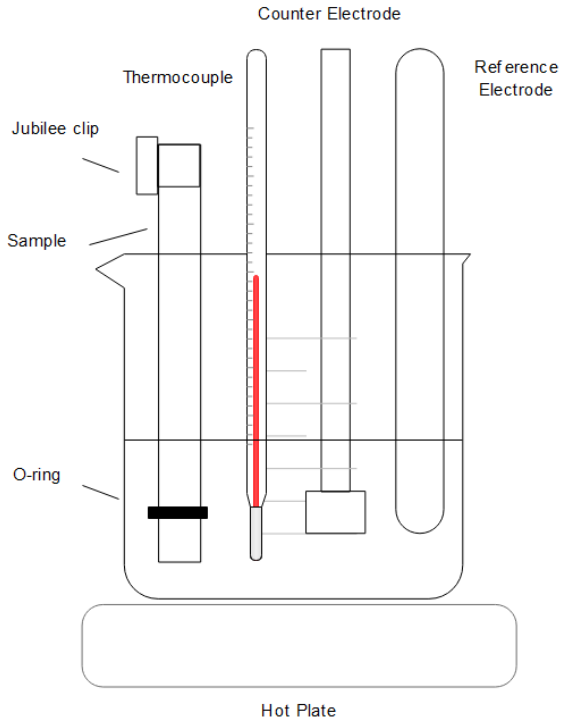

Figure 19: Schematic representation of apparatus set up

An Open Circuit Potential (OCP) was run for 10 minutes at room temperature to ensure correct setup. From a constant laboratory temperature of 23 °C, the potentiostat was recording and the electrolyte was heated to 85 °C and held for 30 minutes. The sample was then taken out of the solution and cleaned with ethanol. This was then repeated for 3 samples of each grade. A time period of 20 minutes was left between each heating cycle to allow the hot plate to cool sufficiently and minimise the effect on the next experiment. The typical experiment duration lasted roughly 45 minutes. The experiment was repeated at 75 °C for three samples of each grade and one sample of each grade was obtained at 65 °C.

The samples were cut using a diamond saw to isolate the corroded end and cleaned with ethanol. The ends were marked with permanent ink into 4 even quarters on the face of the rod and placed underneath the microscope. At each quarter, an image was taken using a Keyence VHX-7000 to generate a 3D depth image and 'flatten' the image due to the cylindrical shape of the rod. Once this was completed, the crevice was measured and the depth recorded. The deepest part was found by performing a horizontal line scan across the sample quarter. An average of the four measurements was calculated to compare between each sample. In some cases, there was no dissolution to measure which was inputted into the sample average as '0 µm'.

The data was presented using current vs time graph and analysed with statistical analysis from box plots also.

Crevice Corrosion Susceptibility Mass Loss

This section is using the same data collected from the prior experimental section of crevice corrosion susceptibility.

Using the current vs time graphs recorded by the potentiostat, charge (Q) was calculated for each sample by integrating under each curve using the trapezium rule below in equation (18):

$$Q = \frac{(x_1 + x_2)}{2} \, x \, (y_2 - y_1) \tag{18}$$

Using Faraday's Law of Electrolysis, mass loss was obtained using the equation (9):

$$M(mg) = \frac{Q}{n*F} * A \quad (9)$$

where Q = charge, n = electrons transferred, F = Faraday's constant and A = atomic weight of Fe. The average mass loss with maximum and minimum values were then calculated for statistical plots to be analysed.

The data obtained from the crevice depths can be used to estimate mass loss also. This model is assuming a continuous crevice formed around the entire circumference. The average crevice depth (r) was converted into metres using equation (19):

$$r\ (m) = \frac{r\ (\mu m)}{10^6} \quad (19)$$

The depth is denoted as r as the crevice depth is the radius of the circumference, see **Figure 16** for visualisation. Area was then calculated using equation (13):

$$Area\ (m^2) = \frac{Pi\ x\ r^2}{2} \quad (13)$$

and as the diameter of the rod was 0.013m, the circumference (C) was calculated in equation (14):

$$C = Pi\ x\ 2\mathrm{r} \quad (14)$$

This was used to calculate the volume of the crevice in equation (15):

$$Volume = Area\ x\ Circumference \quad (15)$$

and mass was found using the density of iron as 7800 into the equation (16):

$$Mass\ (kg) = Volume\ x\ Density \quad (16)$$

finally changed into grams by equation (17):

$$Mass\ (g) = Mass\ (kg) x\ 1000 \quad (17)$$

The two methods have been compared and disparities between them discussed.

3.0 RESULTS

3.1 Influence of Temperature on CPT and Pit Initiation

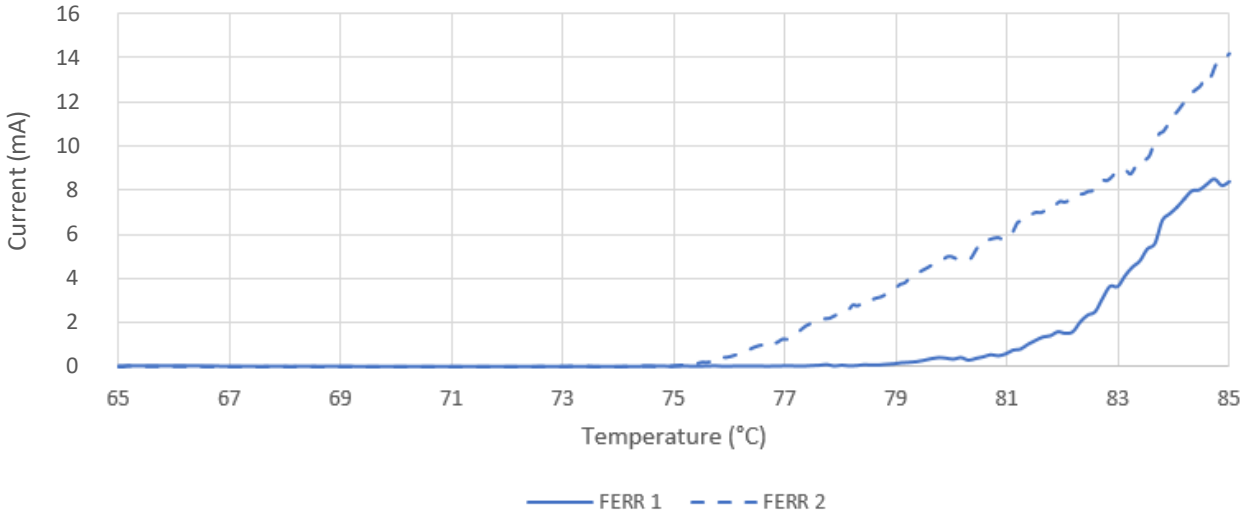

Figure 20: Current vs temperature of FERR after polarising in 3.5% w/v NaCl at 0.9 V vs SCE, 40 °C/hr from 65 °C to 85 °C

Figure 20 displays the potentiostatic polarisation data for two sets of FERR when heated at 40 °C/hour from 65 °C to 85 °C. FERR 1 had a substantial increase in current at ~79 °C with FERR 2 increasing at ~75 °C. Therefore, the CPT can be taken from the average of the two values at 77 °C. FERR 1 showed a constant gradient ending ~14 mA whereas FERR 2 had a sudden increase at 81 °C to plateau ~8 mA.

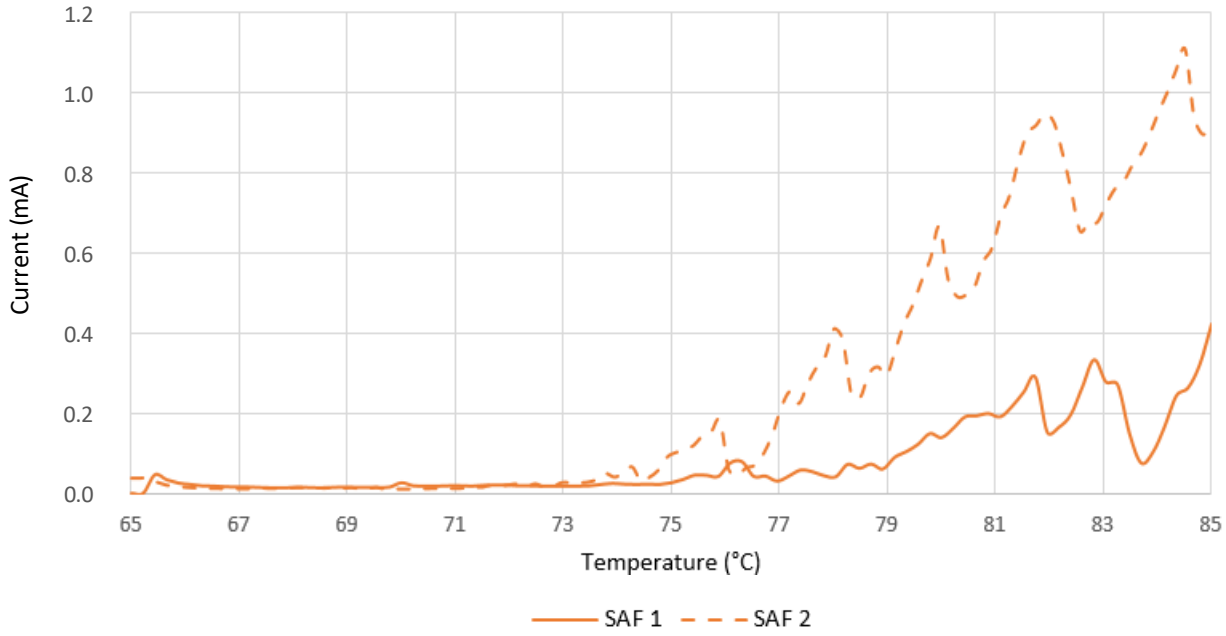

Figure 21: Current vs temperature of SAF after polarising in 3.5% w/v NaCl at 0.9 V vs SCE, 40 °C/hr from 65 °C to 85 °C

Figure 21 displays the potentiostatic polarisation data for two sets of SAF when heated at 40 °C/hour from 65 °C to 85 °C. SAF 1 had a substantial increase in current at ~75 °C with S2 increasing at ~77 °C. Therefore, the CPT can be taken from the average of the two values at 76 °C. Both samples do not have gradually increasing current with increasing temperature. The declines followed by subsequent inclines, seen in both samples in the 83 °C - 85 °C region, could be attributed to repassivation and metastable pitting. There is a large disparity between the final currents, SAF 2 had a concluding current of 0.9 mA, more than double that of SAF 1 with 0.4 mA.

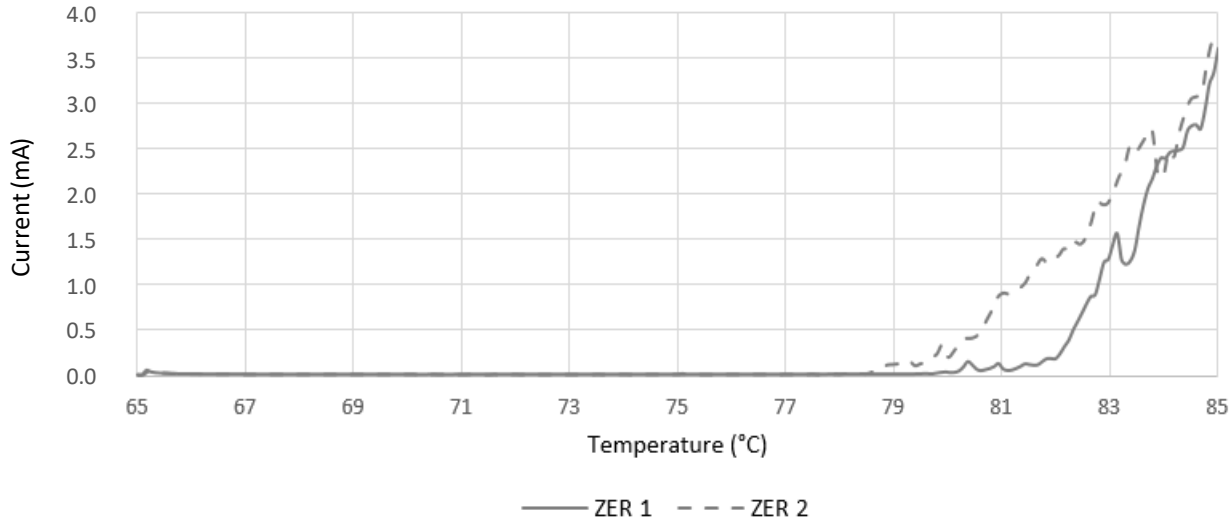

Figure 22: Current vs temperature of ZER after polarising in 3.5% w/v NaCl at 0.9 V vs SCE, 40 °C/hr from 65 °C to 85 °C

Figure 22 displays the potentiostatic polarisation data for two sets of ZER when heated at 40 °C/hour from 65 °C to 85 °C. ZER 1 had a substantial increase in current at ~81 °C with ZER 2 increasing at ~79 °C. Therefore, the CPT can be taken from the average of the two values at 80 °C. Both samples follow similar gradients with some distinct points of possible metastable pitting and repassivation, seen in the 83 °C - 85 °C region. The final current recordings are also similar, both ending just above 3.5 mA.

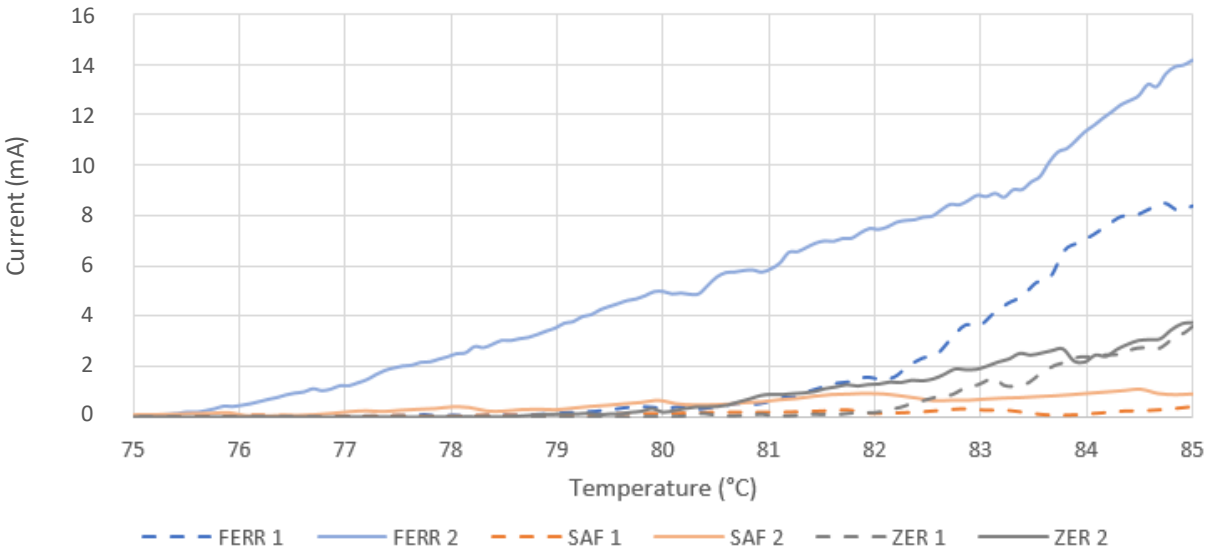

Figure 23: Current vs temperature of all grades after polarising in 3.5% w/v NaCl at 0.9 V vs SCE, 40 °C/hr from 65 °C to 85 °C

Figure 23 shows the data from **Figures 20, 21 & 22** from 75 °C - 85 °C. Both FERR samples have higher current in comparison with the other two grades, FERR 2 in particular with a current of ~14 mA. ZER and SAF have more similar gradients throughout, but SAF had the lowest current ~1 mA.

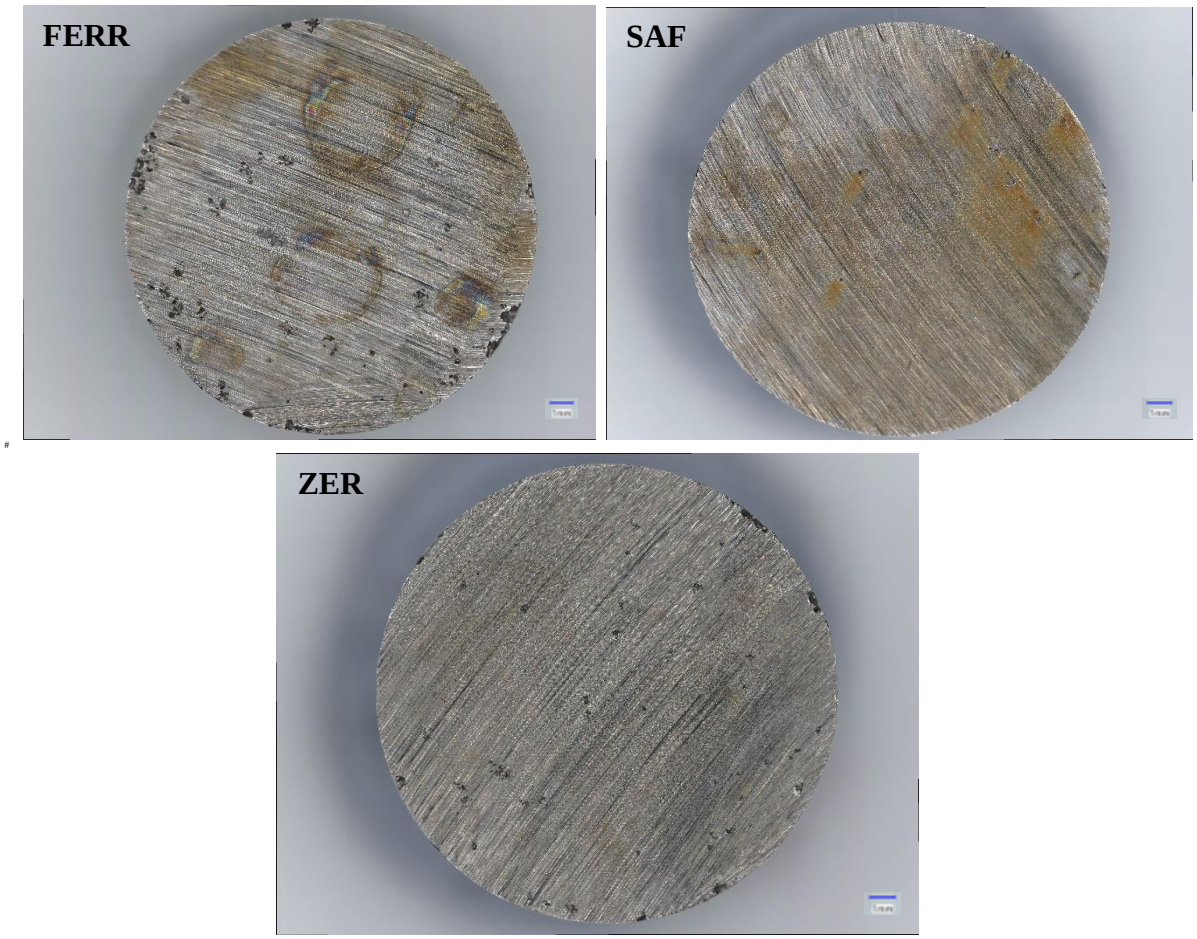

Figure 24: Extent of pitting corrosion in each sample observed after polarising in 3.5% w/v NaCl at 0.9 V vs SCE, 40 °C/hr from 65 °C to 85 °C

Six samples were analysed and **Figure 24** shows representative images of the corrosion observed in the three grades. FERR had the greatest corrosion damage seen with evidence of coalesced pits around the circumference and on the end face. ZER also had visible corroded areas with some large pits visible around the circumference. SAF had evidence of corrosion due to the product formed on the face although only small pits can be observed, possible evidence of metastable pitting and repassivation.

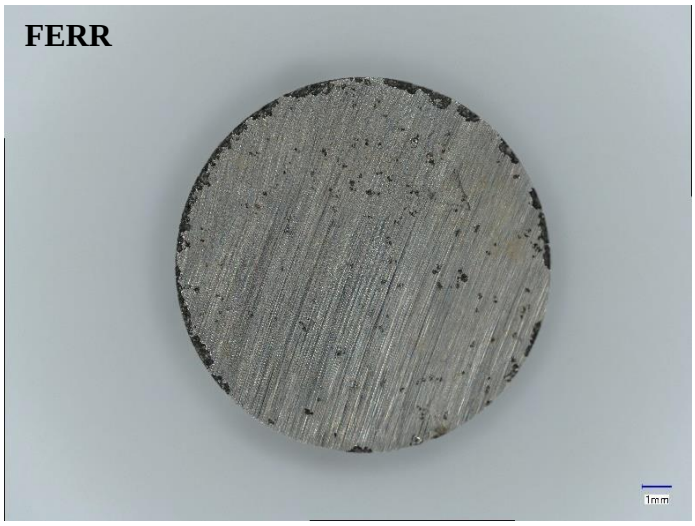

Figure 25: Sample two of FERR showing extent of pitting corrosion observed after polarising in 3.5% w/v NaCl at 0.9 V vs SCE, 40 °C/hr from 65 °C to 85 °C

Figure 25 shows the corrosion observed on a sample two of FERR. Due to the intense dissolution, the pits formed on the circumference have coalesced into larger areas. It could suggest that preferential corrosion occurred around the circumference which was not observed as severely in other samples. The outer diameter was also heavily corroded, not all corrosion was solely on the face of the sample.

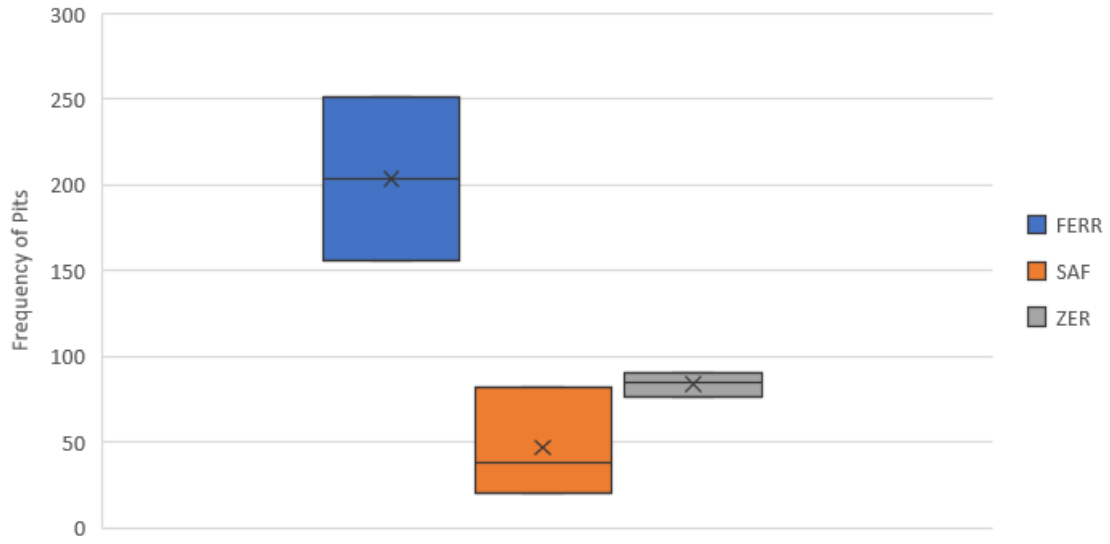

Figure 26: Number of pits observed in each sample after polarising in 3.5% w/v NaCl at 0.9 V vs SCE, 40 °C/hr from 65 °C to 85 °C

Figure 26 shows the statistical spread of data between the three grades in terms of frequency of pits observed. Due to slight skewness in the data obtained for SAF, the median value will be used for comparison instead of the average. FERR had the largest distribution of data points suggesting high variability in the data, and the highest frequency with a median of 204 pits. As there is no overlap in the FERR dataset with the other two grades, this suggests a large statistical difference between them. ZER had the smallest variability in the data but a higher frequency of pits than SAF with medians of 85 and 38 pits respectively. Although, there is little statistical difference between SAF and ZER as the data overlaps.

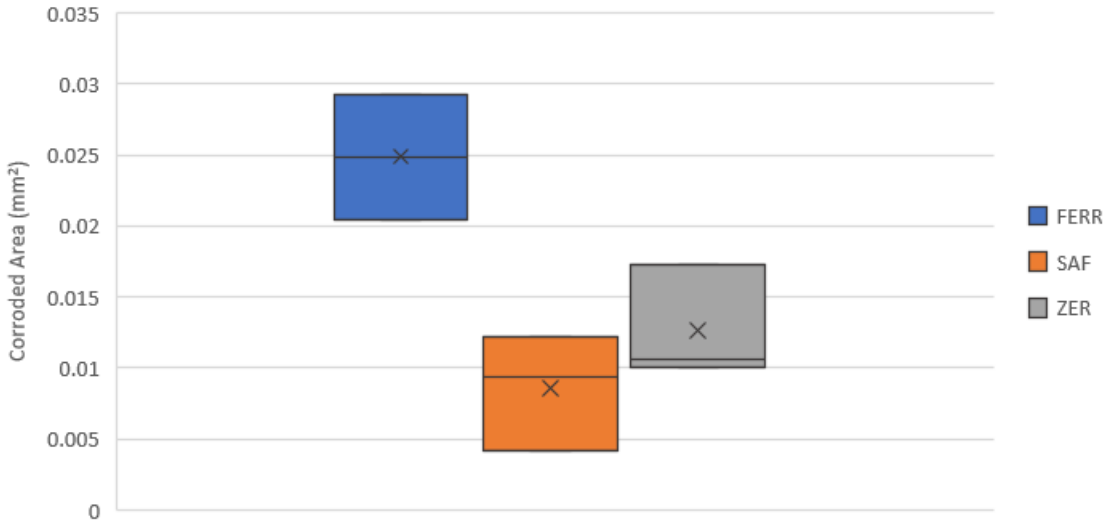

Figure 27: Average corroded area of pits in each sample after polarising in 3.5% w/v NaCl at 0.9 V vs SCE, 40 °C/hr from 65 °C to 85 °C

Figure 27 shows the statistical spread of data between the three grades in terms of corroded area measured. Due to the skewed data seen in SAF and ZER, the median value will be used for comparison instead of the average. FERR had the largest corroded area of the three with a median of 0.02488 mm^2. As there is no overlap in the FERR dataset with the other two grades, this suggests a large statistical difference between them. However, all three have similar distributions of data points implying similar variability. SAF and ZER have little difference between them as the two plots overlap, although ZER had a slightly larger corroded area than SAF with medians of 0.01056 mm^2 and 0.00940 mm^2 respectively. Both samples performed similarly with over half the corroded area in comparison to FERR.

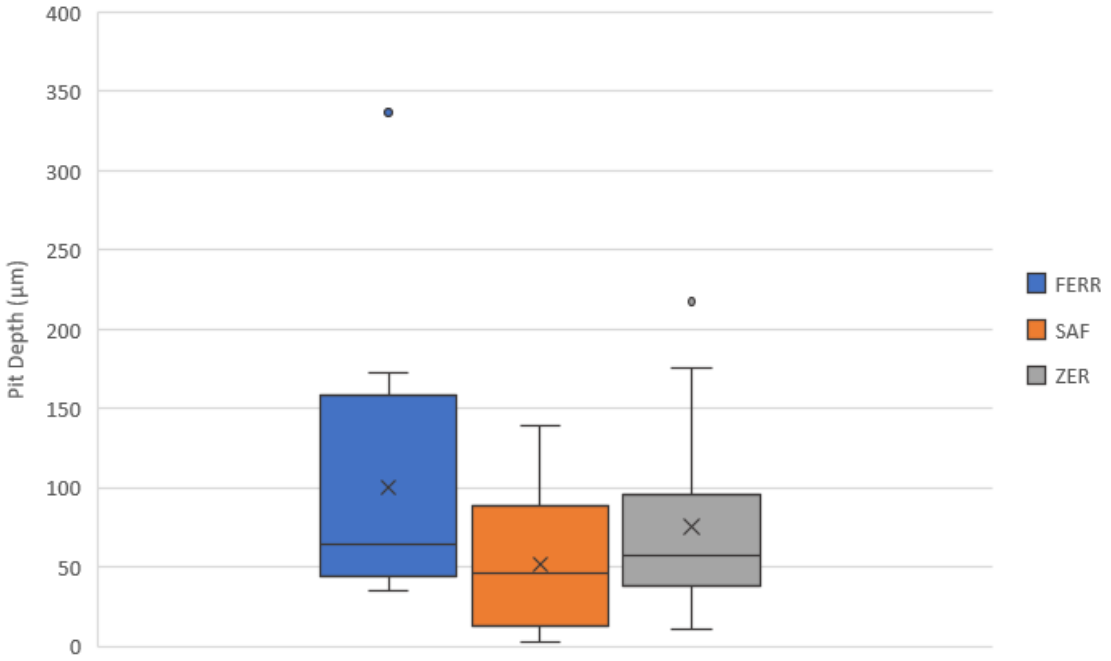

Figure 28: Average depth of pits in each sample after polarising in 3.5% w/v NaCl at 0.9 V vs SCE, 40 °C/hr from 65 °C to 85 °C, with outliers

Figure 28 shows the statistical spread of data between the three grades in terms of pit depths measured. As all three data sets are positively skewed, the median will be used in comparison instead of the average value. As the data sets overlap there is not a large statistical difference between the samples, as seen by the similar medians of FERR with the deepest pits of 64.44 µm, 57.91 µm for ZER and 46.5 µm for SAF. ZER had the largest distribution although FERR had the largest interquartile range suggesting higher variability in the data. Two outliers are seen, one in FERR and one in ZER, the impact of these have been reflected below in **Figure 29**.

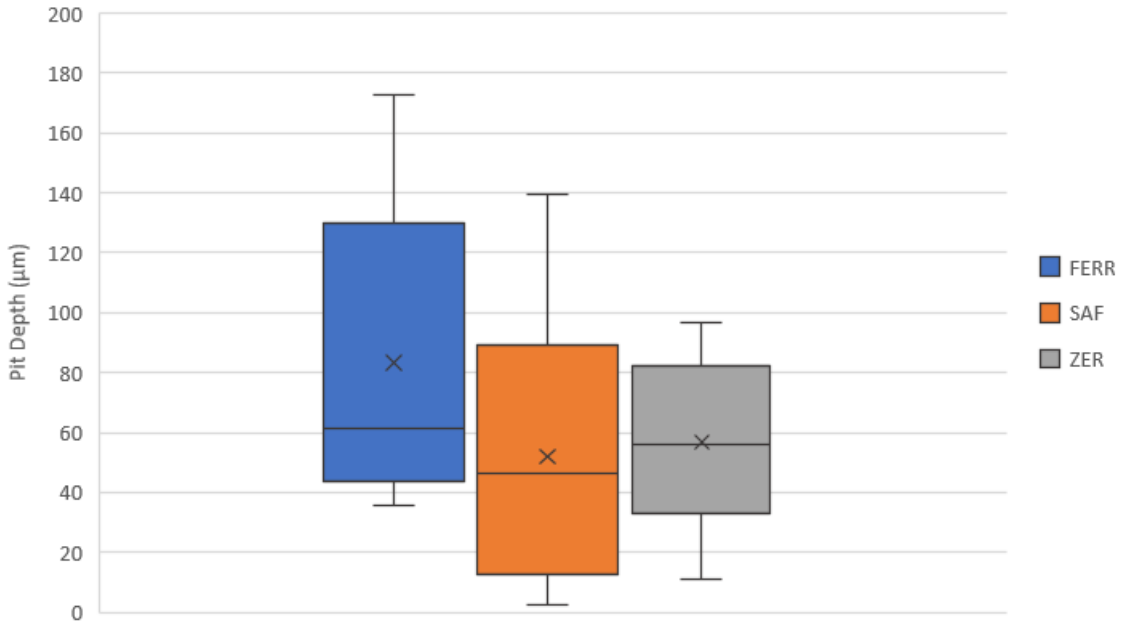

Figure 29: Average depth of pits in each sample after polarising in 3.5% w/v NaCl at 0.9 V vs SCE, 40 °C/hr from 65 °C to 85 °C, without outliers

Figure 29 shows the impact in pit depths without the outliers calculated in **Figure 28**. FERR had the widest distribution of data whilst ZER had the smallest. Both grades' median pit depth values decreased from 64.44 µm to 61.56 µm and 57.91 µm to 55.79 µm respectively. Both samples have improved performance in comparison to SAF which had the same median of 46.5 µm.

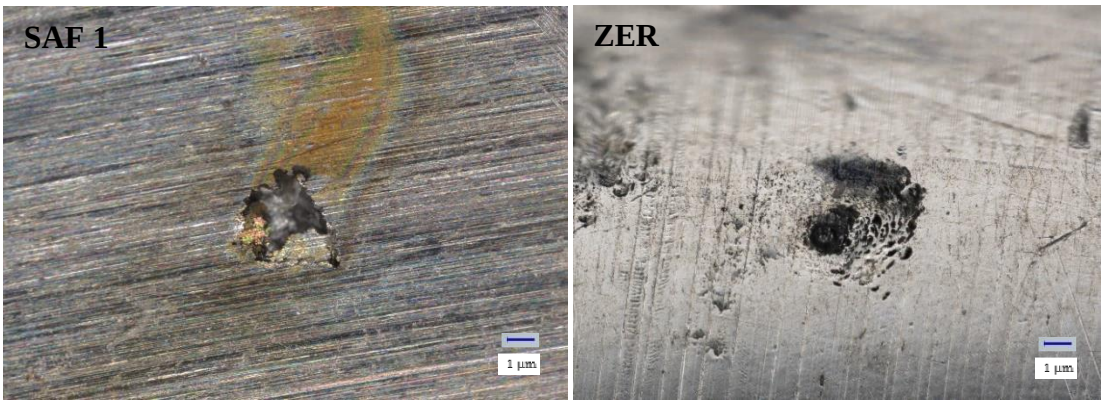

Figure 30: A lacy pit observed in SAF 1 and ZER 2

Figure 30 shows a feature observed on sample SAF 1 and ZER 2. Lacy pits were seen on each sample with varying size and shape, but all had a majority of material covering the top of the pit. This is evidence of repassivation.

3.2 Influence of Temperature on Mass Loss in Aerated Conditions

This section uses the same data collected from the prior section of aerated samples.

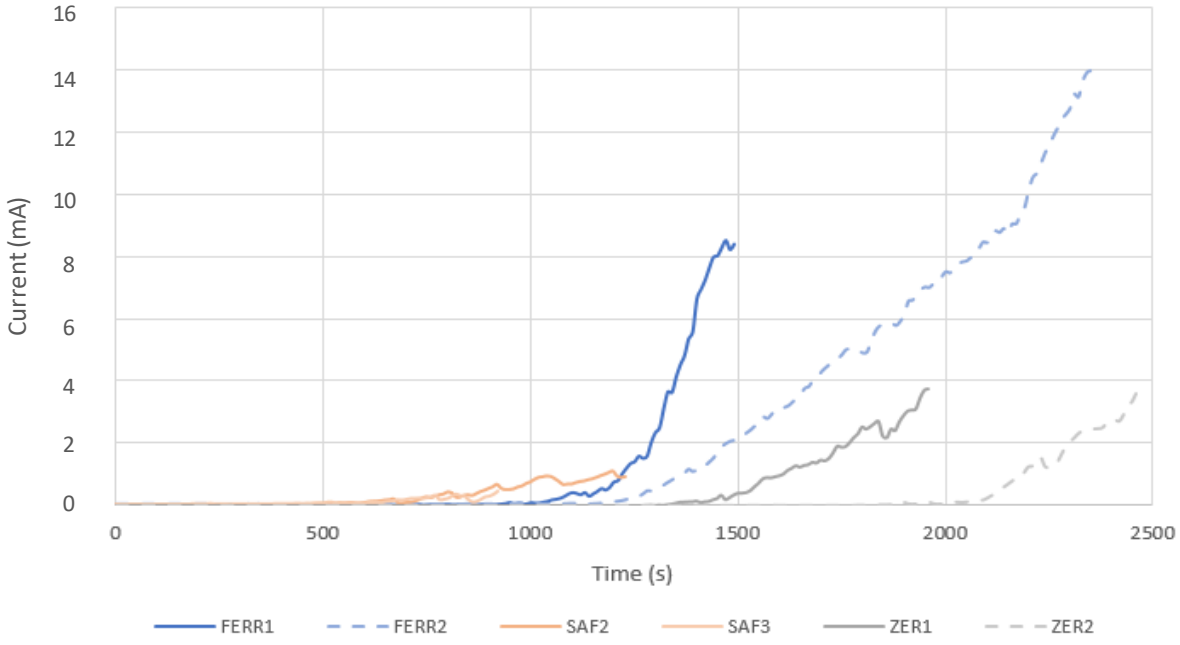

Figure 31: Current vs time of all samples after polarising in 3.5% w/v NaCl at 0.9 V vs SCE, 40 °C/hr from 65 °C to 85 °C

Using **Figure 31**, charge (Q) was calculated for each sample by integrating under each curve and using equation (18) and equation (9) using Faraday's Law of Electrolysis to determine the mass loss. The data obtained from pit depths can be used to estimate mass loss also by using equations (10), (11) & (12). The two methods have been compared and disparities between them discussed.

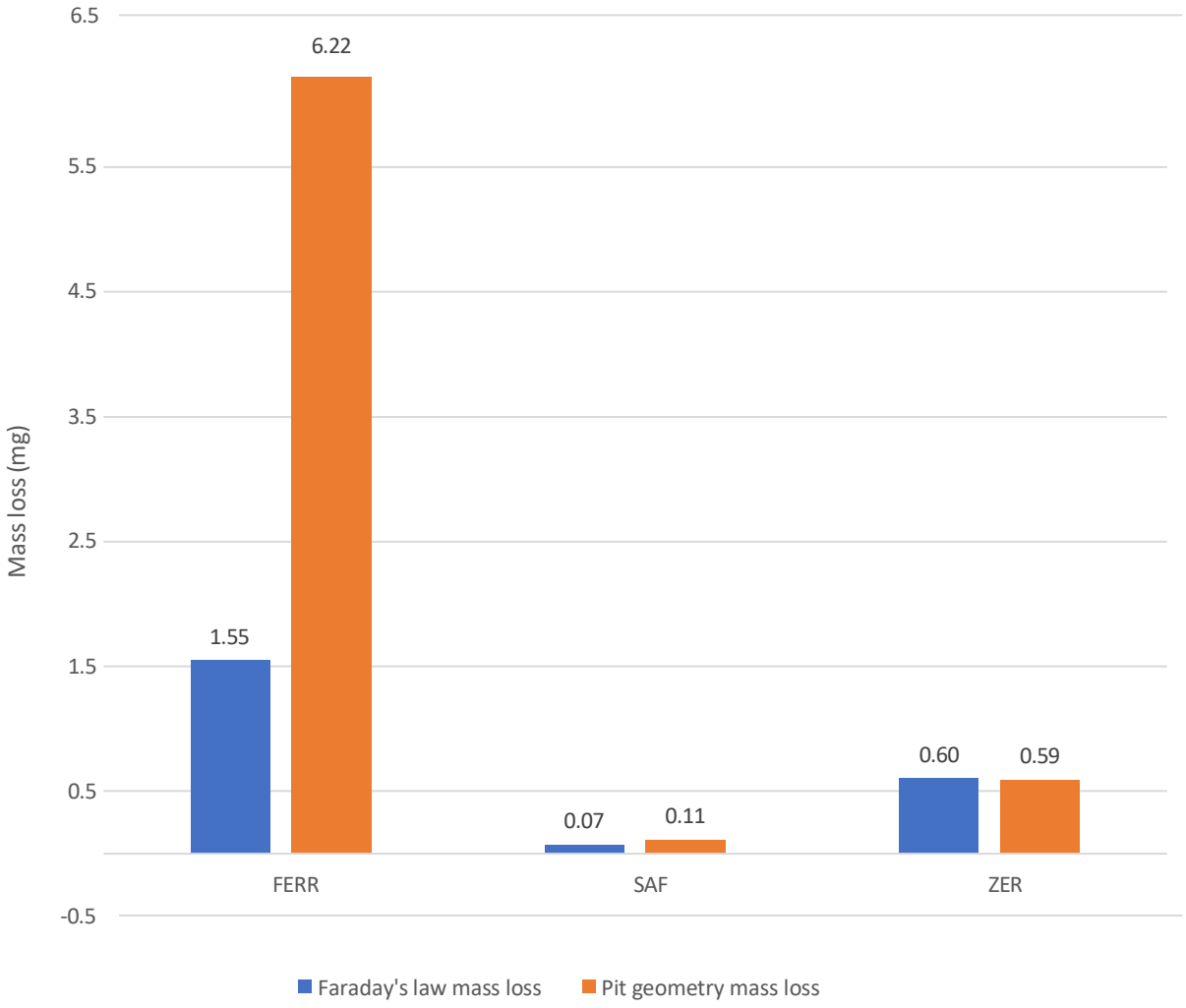

Figure 32: Faraday's Law and pit geometry average mass loss for each sample

Using the values calculated using Faraday's Law and pit geometry, the mass loss for each sample can be seen in **Figure 32**. FERR had the largest mass loss from both methods used with a disparity between each value, 4.67 mg. SAF and ZER had very similar mass loss values calculated with differences of 0.04 mg and 0.1 mg respectively. This implies the techniques accurately calculated mass loss in those grades whereas other factors contributed to FERR, causing the difference.

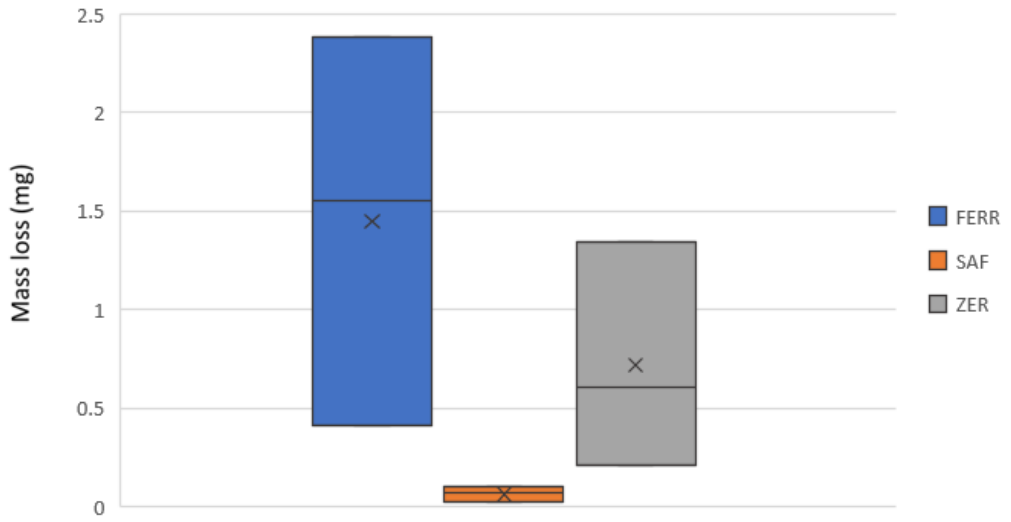

Figure 33: Faraday's Law mass loss for each sample

From **Figure 33**, FERR and ZER had wide distributions in comparison to SAF, implying unpredictability of both grades when heating 40 °C/hour to 85 °C. FERR had the largest mass loss with an average of 1.39 mg with ZER at 0.76 mg. SAF had very small variation in the data with a very low mass loss of 0.07 mg.

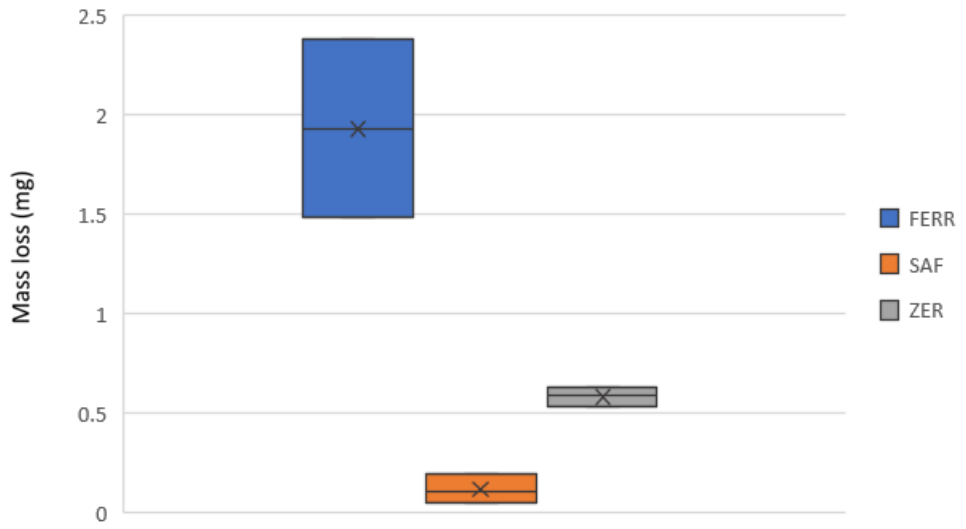

Figure 34: Pit geometry mass loss for each sample

From **Figure 34**, FERR had a significantly wide distribution in comparison to SAF and ZER, implying unpredictability of this grade when calculating mass loss from its pit geometry. FERR had the largest mass loss with a median of 2.38 mg. SAF and ZER had very small variation in the data with both having very low mass loss of 0.11 mg and 0.59 mg.

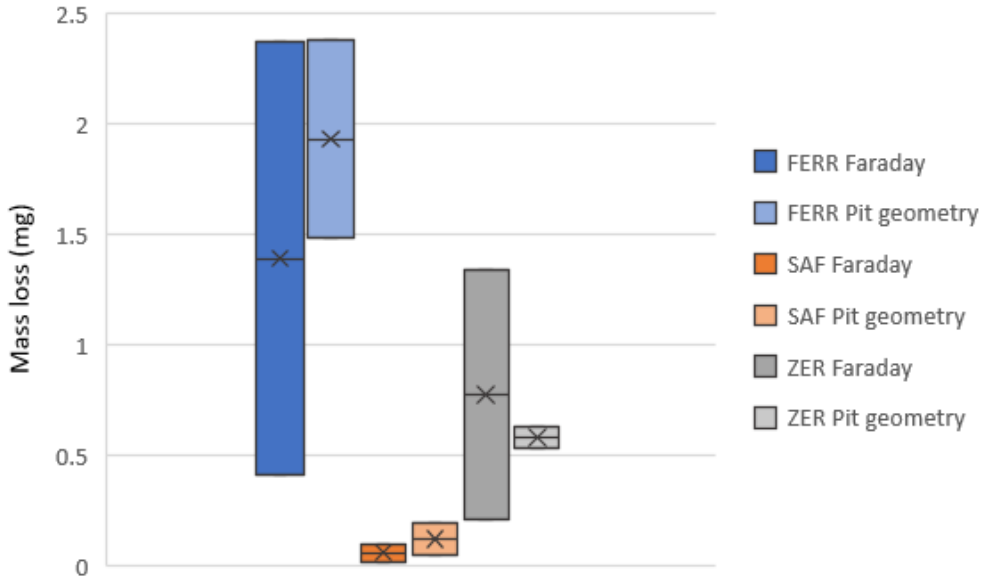

Figure 35: Faraday's Law and pit geometry mass loss for each sample

From **Figure 35**, both FERR and ZER have significant disparities between Faraday's Law and pit geometry calculations with the distribution of data for Faraday values much wider and both averages statistically different, 0.54 mg and 0.20 mg respectively. Both values calculated for SAF are similar in terms of distribution and average, with a 0.06 mg difference. For FERR and SAF, the average values were both smaller than the pit geometry average whereas ZER had a higher value for the Faraday average.

3.3 Influence of Deaeration and Surface Finish on Pit Initiation

This section is a comparison with the prior section of aerated results. These alloys may be used in both conditions in service so difference in performance is an interesting insight.

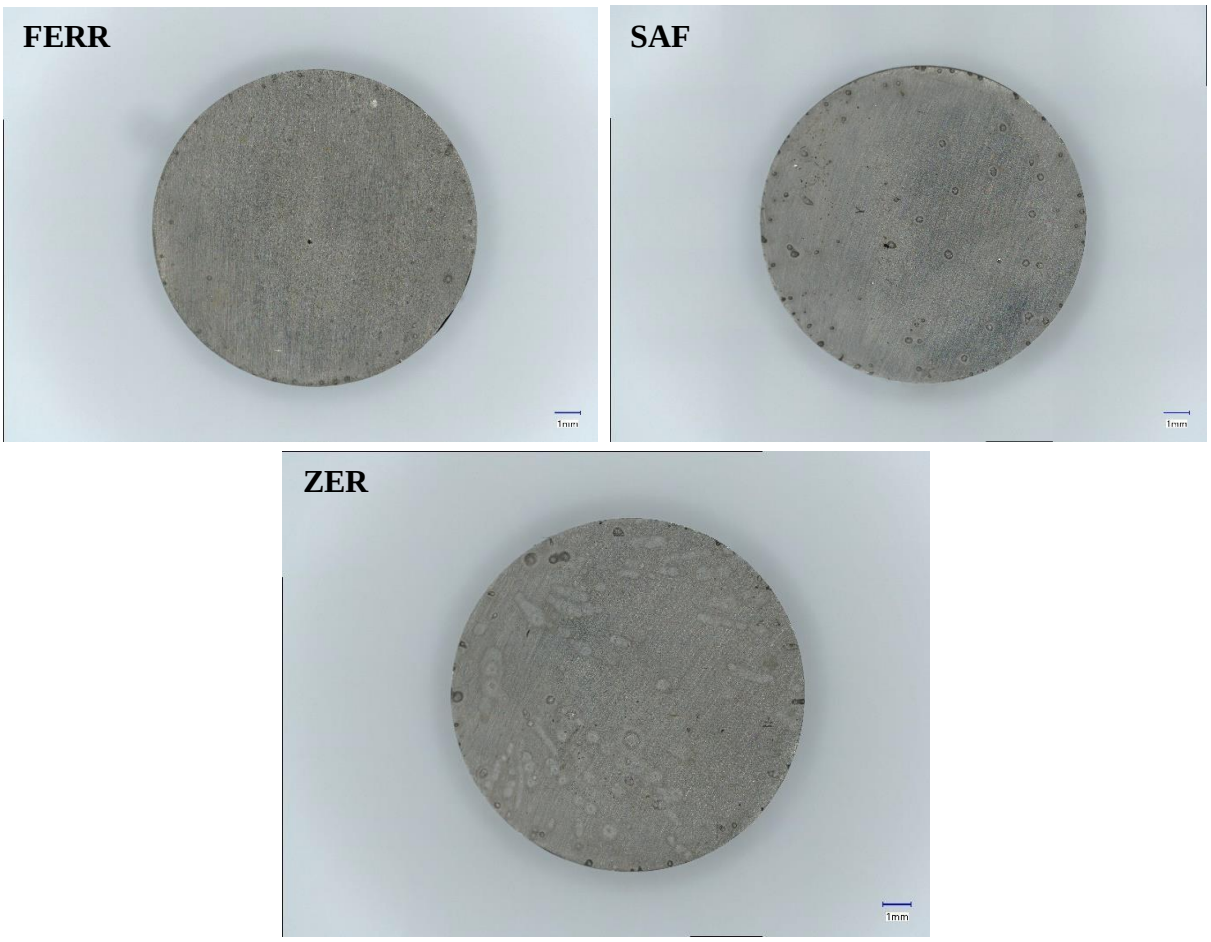

Figure 36: Extent of pitting corrosion in each sample observed after polarising in 3.5% w/v NaCl at 0.9 V vs SCE, 30°C/hr from 65 °C to 85 °C

Nine samples were analysed with **Figure 36** showing representative images of the corrosion observed in the three grades. Very few large pits were observed although smaller pits are visible which are hard to distinguish as most samples had evidence of metastable pitting and repassivation. This can be seen by the evidence of corrosion as the darker circular features mostly on SAF and ZER.

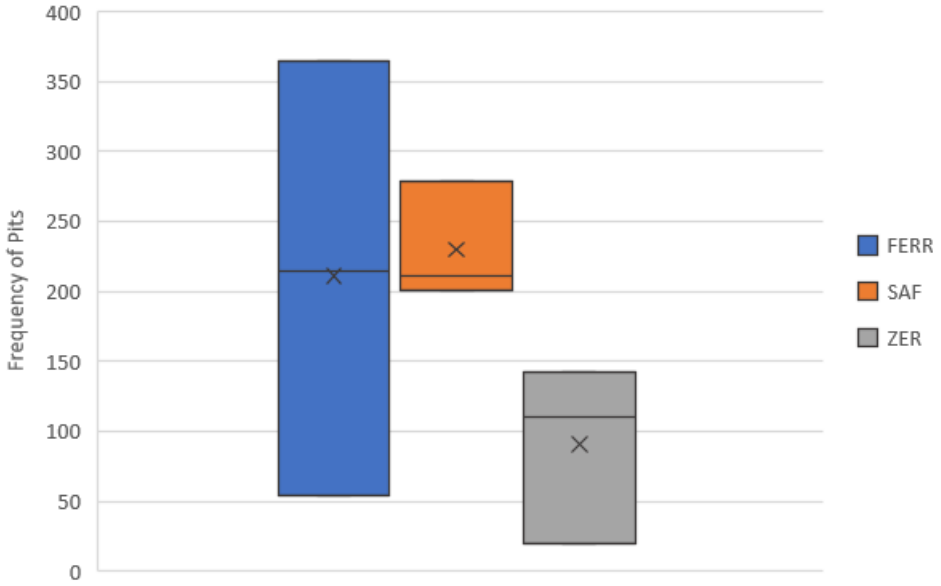

Figure 37: Number of pits observed in each sample after polarizing in 3.5% w/v NaCl at 0.9 V vs SCE, 30°C/hr from 65 °C to 85 °C

Figure 37 shows the statistical spread of data between the three grades in terms of frequency of pits observed. As all three data sets are skewed, the median will be used in comparison instead of the average value. FERR had the largest distribution of data points suggesting unpredictability of this grade, although there is little difference in the median frequency of pits with SAF of 214 and FERR of 211 pits respectively. Even though SAF had the smallest variability, ZER had the lowest median of the three with 110 pits, a significant statistical difference is seen between SAF and ZER as the plots do not overlap.

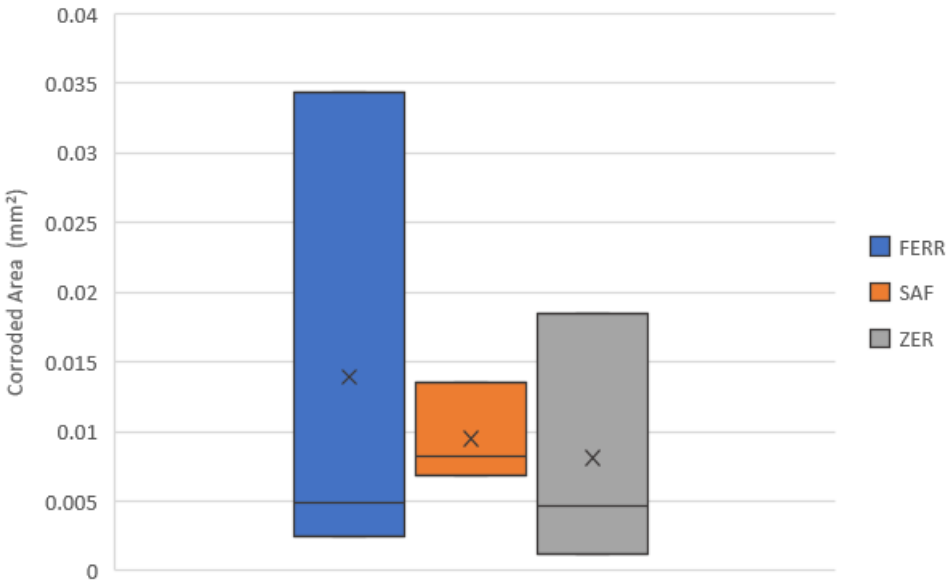

Figure 38: Average corroded area of pits in each sample after polarising in 3.5% w/v NaCl at 0.9 V vs SCE, 30 °C/hr from 65 °C to 85 °C

Figure 38 shows the statistical spread of data between the three grades in terms of corroded area measured. Due to skewness of the data obtained, the median value will be used for comparison instead of the average. FERR had the largest distribution of data points suggesting high variability in the data, although a relatively low corroded area with a median of 0.00488 mm^2. SAF had the smallest variability in the data but with a median of 0.00817 mm^2, it is almost double that of ZER which had a median area of 0.00465 mm^2. However, as the data overlaps there is little statistical difference between the three.

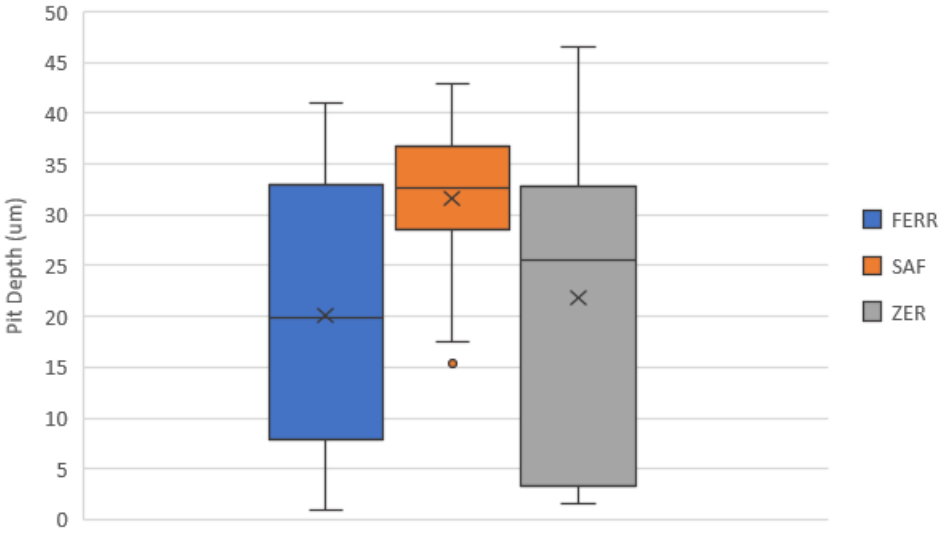

Figure 39: Average depth of pits in each sample after polarising in 3.5% w/v NaCl at 0.9 V vs SCE, 30 °C/hr from 65 °C to 85 °C

Figure 39 shows the statistical spread of data between the three grades in terms of pit depths measured. Due to skewness of the data obtained, the median value will be used for comparison instead of the average. SAF had the smallest variability in the data in comparison to FERR and ZER which have wide distributions. However, SAF had the largest pit depths with a median of 32.58 µm in comparison to FERR with 19.8 µm and ZER with 25.62 µm. As the data overlaps there is little statistical difference between the three. SAF had one outlier, the impact of this has been reflected below in **Figure 40**.

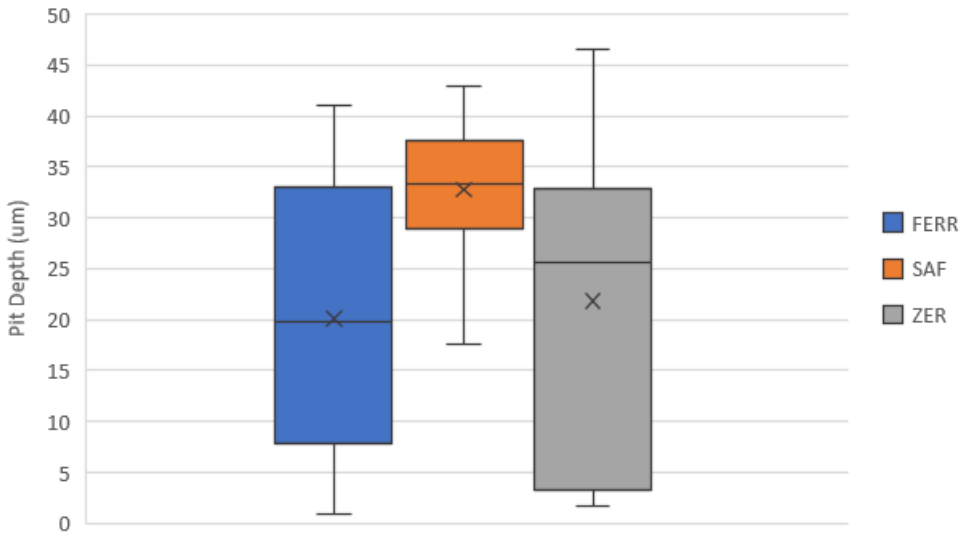

Figure 40: Average depth of pits in each sample after polarising in 3.5% w/v NaCl at 0.9 V vs SCE, 30 °C/hr from 65 °C to 85 °C, without outliers

Figure 40 shows the impact in pit depths without the outlier calculated in **Figure 39**. SAF still had the largest median pit depths but had subsequently increased from 32.58 µm to 33.29 µm. The performance of SAF had decreased in comparison to FERR and ZER which have the same medians of 19.8 µm and 25.62 µm respectively.

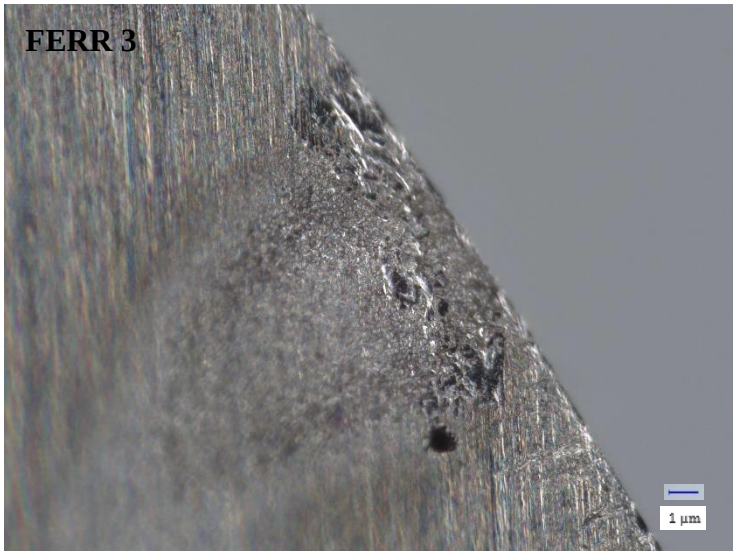

Figure 41: A lacy pit observed in FERR 3

Figure 41 shows a feature observed on a sample of FERR. Lacy pits were seen on the samples of varying size and shape, but all had a majority of material covering the top of the pit. This is evidence of repassivation.

3.4 Crevice Corrosion Susceptibility of SDSS at Temperature

This section is on crevice corrosion susceptibility of the three alloys at varying temperatures. Crevice corrosion can occur in service as well as pitting. Using o-rings can mimic a crevice to understand behaviour of the alloys.

85 °C

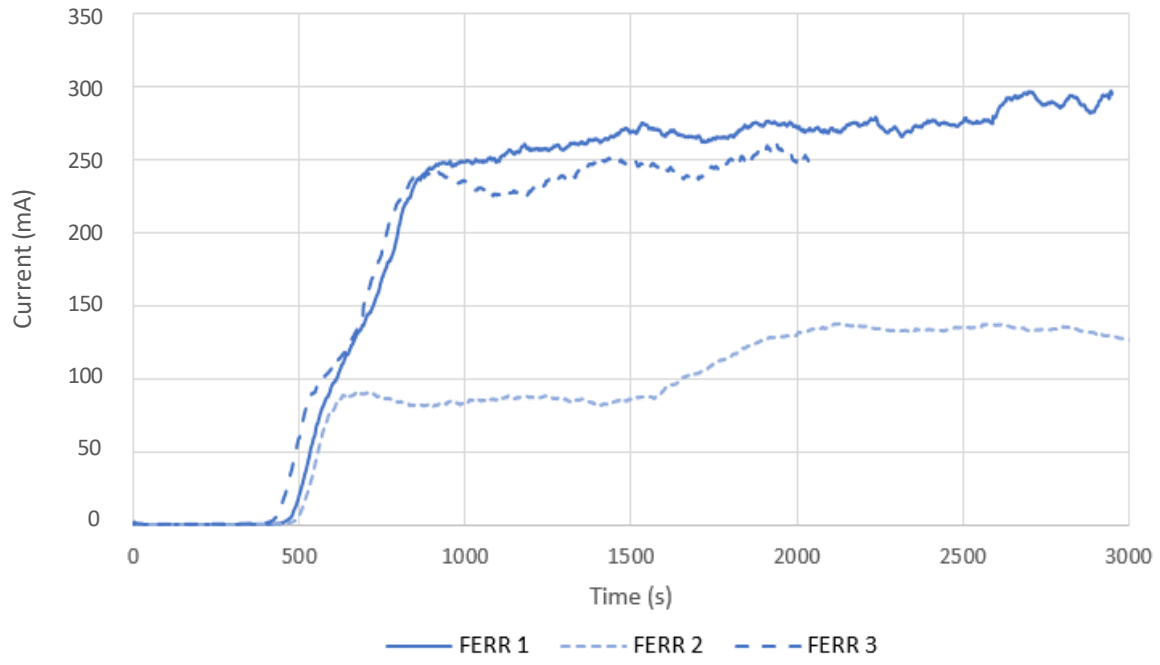

Figure 42: Current vs time of all three FERR samples after polarising in 3.5% w/v NaCl at 0.9 V vs SCE, heated to 85 °C and held for 30 minutes

Figure 42 displays the potentiostatic polarisation data for three sets of FERR when heated to 85 °C and held for 30 minutes. The data for FERR 3 had not been plotted past ~2000 s due to connection error in the equipment. All three samples have a substantial increase in current at ~500 s with similar gradients until ~90 mA, where FERR 2 started to plateau with a final current of 130 mA. FERR 1 & 3 followed a very consistent pattern up to 240 mA, in which they split slightly with FERR 1 finishing ~300 mA and FERR 3 ~250 mA.

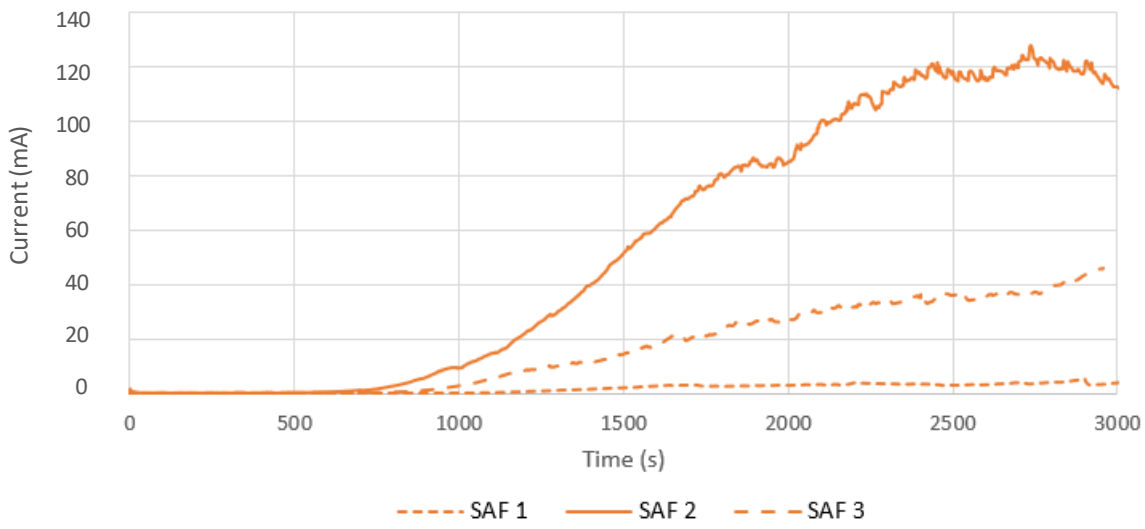

Figure 43: Current vs time of all three SAF samples after polarising in 3.5% w/v NaCl at 0.9 V vs SCE, heated to 85 °C and held for 30 minutes

Figure 43 displays the potentiostatic polarisation data for three sets of SAF when heated to 85 °C and held for 30 minutes. SAF 2 was the first to have a substantial rise in current at ~800 s with SAF 3 following ~200 s later. Both had consistent gradients although SAF 2 had the steepest increase in current, peaking at 120 mA after 2500 s, whereas SAF 3 rose to a concluding current of 50 mA. SAF 1 did not have a noticeable increase in current, rising slightly ~1500 s but only reaching a maximum of 5 mA throughout.

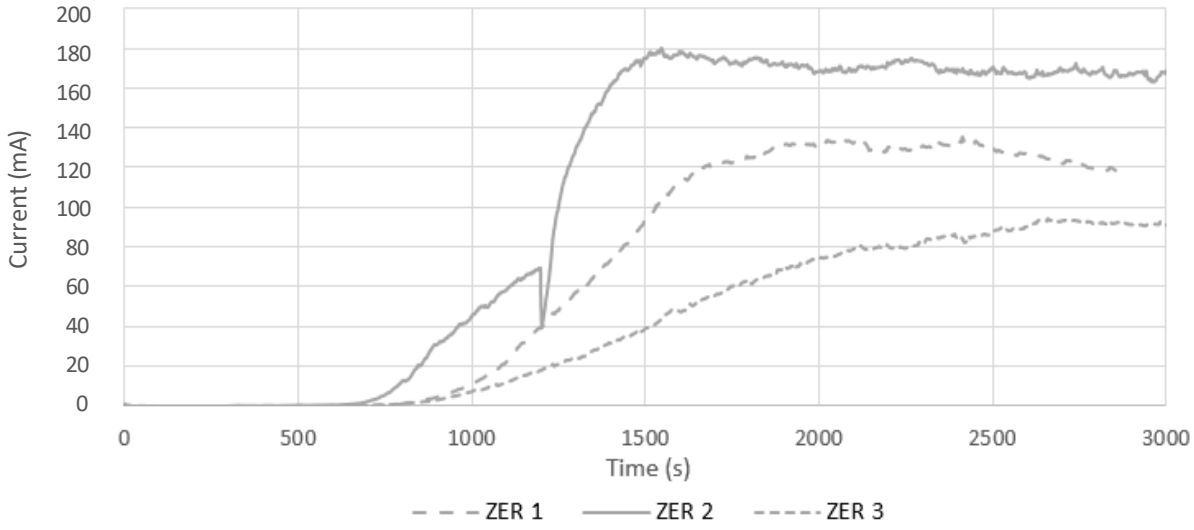

Figure 44: Current vs time of all three ZER samples after polarising in 3.5% w/v NaCl at 0.9 V vs SCE, heated to 85 °C and held for 30 minutes

Figure 44 displays the potentiostatic polarisation data for three sets of ZER when heated to 85 °C and held for 30 minutes. ZER 2 was the first to have a considerable increase in current ~700s with both ZER 1 & 3 following ~200s later. ZER 2 displayed some unique behaviour between 1000s – 1500s, in which the current rose to 70 mA, dropped rapidly down to 40 mA and immediately increased up to 180 mA where it plateaued for the duration of the temperature hold. This could possibly be metastable pitting or repassivation. The two other samples followed a regular trend with ZER 1 plateauing ~2000s with a concluding current of 120 mA and ZER 3 ~2500s with a final current of 90 mA.

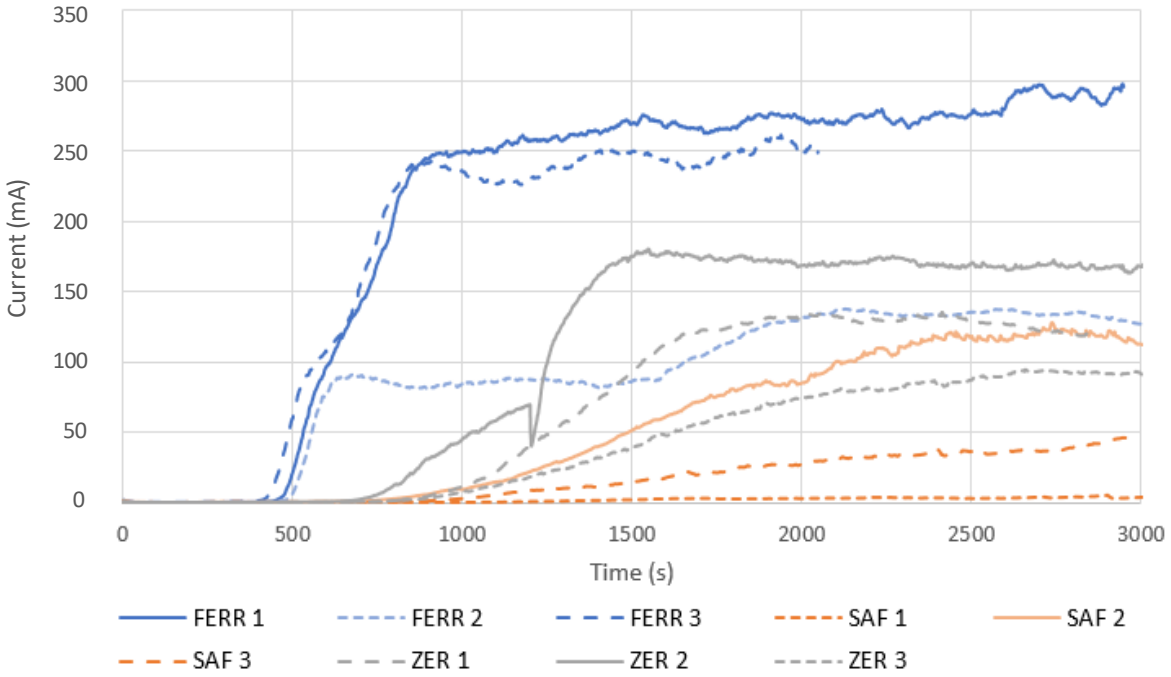

Figure 45: Current vs time of all three samples after polarising in 3.5% w/v NaCl at 0.9 V vs SCE, heated to 85 °C and held for 30 minutes

Figure 45 displays the potentiostatic polarisation data of all nine samples when heated to 85 °C and held for 30 minutes. The FERR samples were the first to have a substantial increase in current with ZER 2 following ~200 s afterward. The other samples all began to increase in current ~1000 s, all following a similar pattern of steady rise and plateau but with varying gradients. All three ZER, FERR 2 and SAF 2 & 3 all had final currents ending within 100 mA of each other. SAF 1 did not exhibit the same behaviour as there was no substantial rise in current throughout the test with an almost a flat gradient seen.

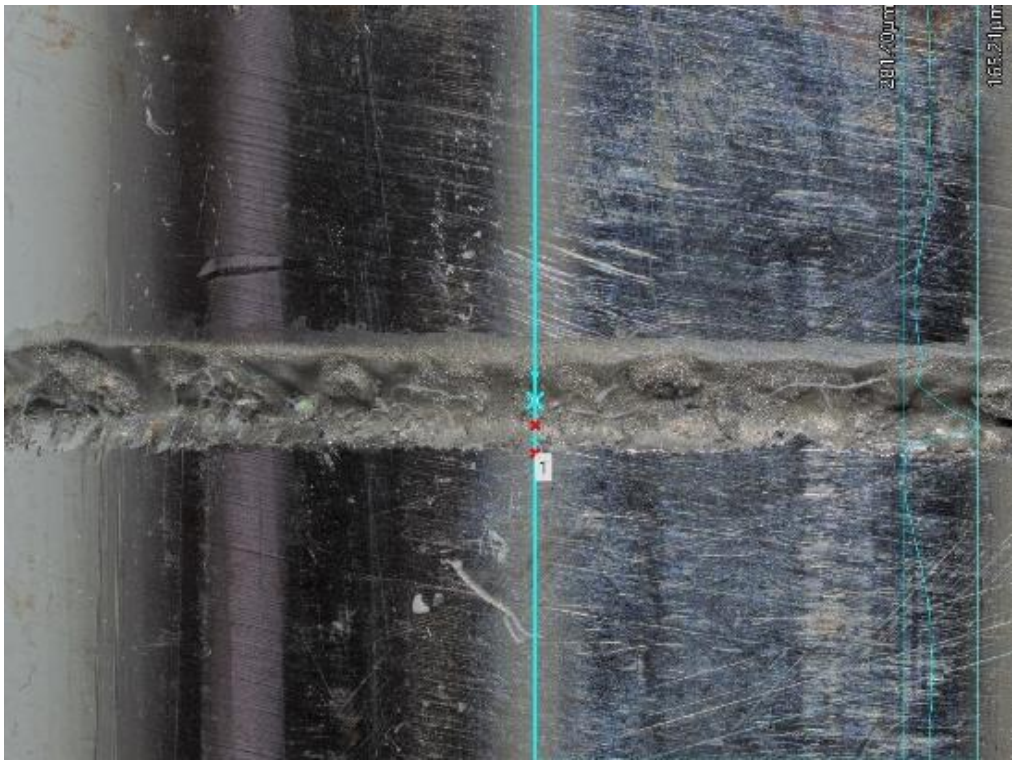

Figure 46: Crevice depth measurement from ZER 3 after polarising in 3.5% w/v NaCl at 0.9 V vs SCE, heated to 85 °C and held for 30 minutes

Figure 46 shows a micrograph and the technique used to measure the crevice depths from ZER 3, after heating to 85 °C and held for 30 minutes. This is a suitable representative image as all samples had a crevice around the entire circumference from underneath the o-ring as seen above.

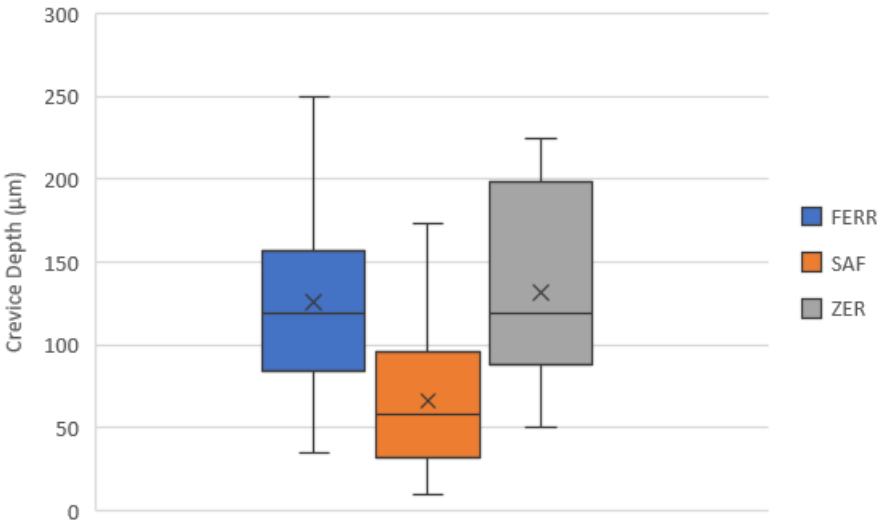

Figure 47: Average depth of crevice formed in each sample after polarising in 3.5% w/v NaCl at 0.9 V vs SCE, heated to 85 °C and held for 30 minutes

Figure 47 shows the statistical spread of data between the three grades with respect to depths of the crevice formed at 85 °C. Due to positively skewed data of all three grades, the median value will be used for comparison instead of the average. FERR had the largest distribution of the data sets, but ZER had the widest interquartile range implying higher variability of the data. However, FERR and ZER had similar crevice depths with medians of 119.47 µm and 118.84 µm respectively. SAF had the smallest variability in the data and the lowest median of the three, 57.71 µm, over half the crevice depth produced in both FERR and ZER. As all three data plots overlap, there is little statistical difference overall.

75 °C

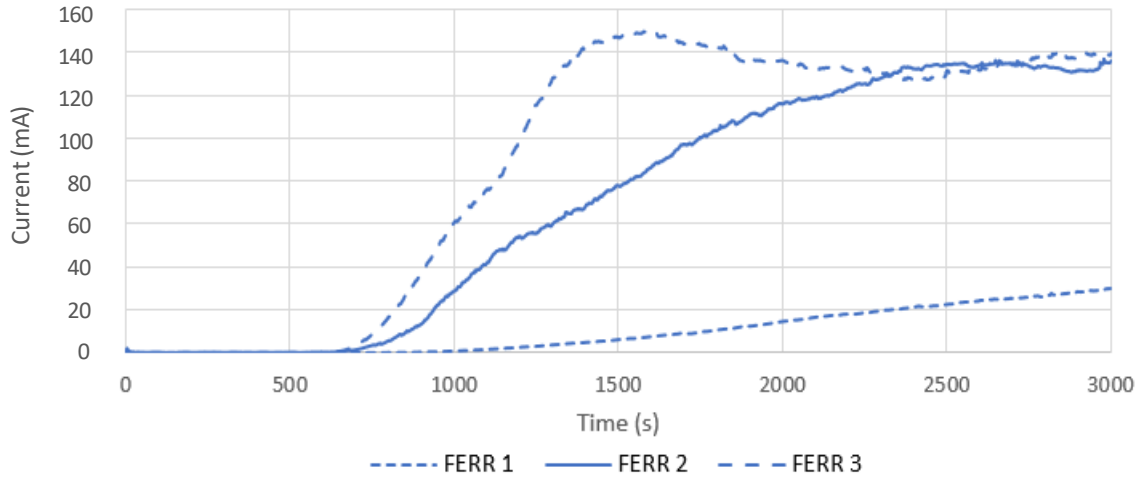

Figure 48: Current vs time of all FERR samples after polarising in 3.5% w/v NaCl at 0.9 V vs SCE, heated to 75 °C and held for 30 minutes

Figure 48 displays the potentiostatic polarisation data for three sets of FERR when heated to 75 °C and held for 30 minutes. Both FERR 2 & 3 had increases in current ~700 s but FERR 2 had a gradual increase up to 130 mA, whereas FERR 3 rose steeply up to 150 mA until remaining steady at a slightly lower current of 130 mA, till the end of the hold. FERR 1 exhibited different behaviour with a current increase ~400 s later than the other two samples and a very gradual gradient, ending with a final current of 30 mA, significantly lower than FERR 2 & 3.

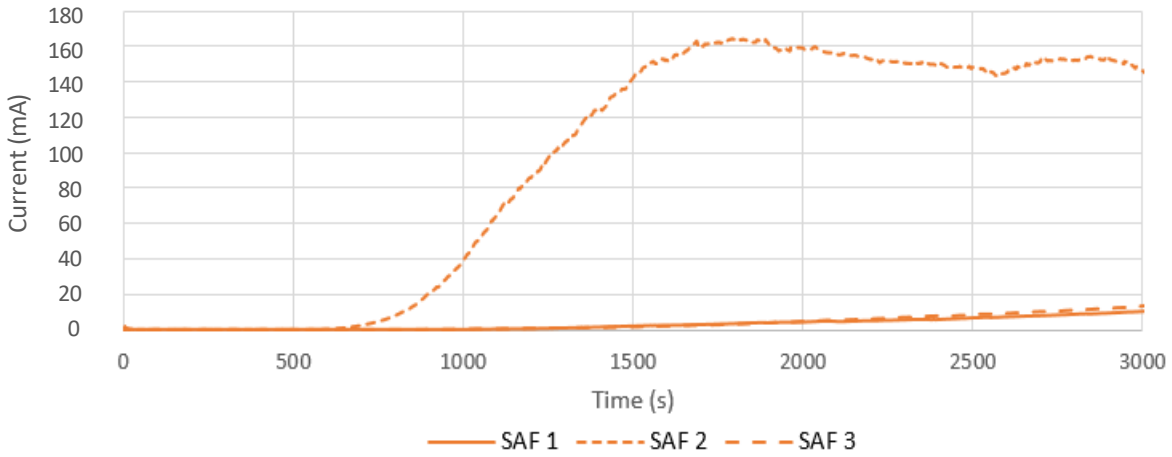

Figure 49: Current vs time of all SAF samples after polarising in 3.5% w/v NaCl at 0.9 V vs SCE, heated to 75 °C and held for 30 minutes

Figure 49 displays the potentiostatic polarisation data for three sets of SAF when heated to 75 °C and held for 30 minutes. SAF 2 displayed contrasting behaviour to the other two samples with increased current ~700 s and a steep gradient up to 160 mA, which plateaued till the end of the hold. Both SAF 1 & 3 had almost identical tests with rises in current ~1000 s after SAF 2, very flat gradients and similar final currents of 10 mA.

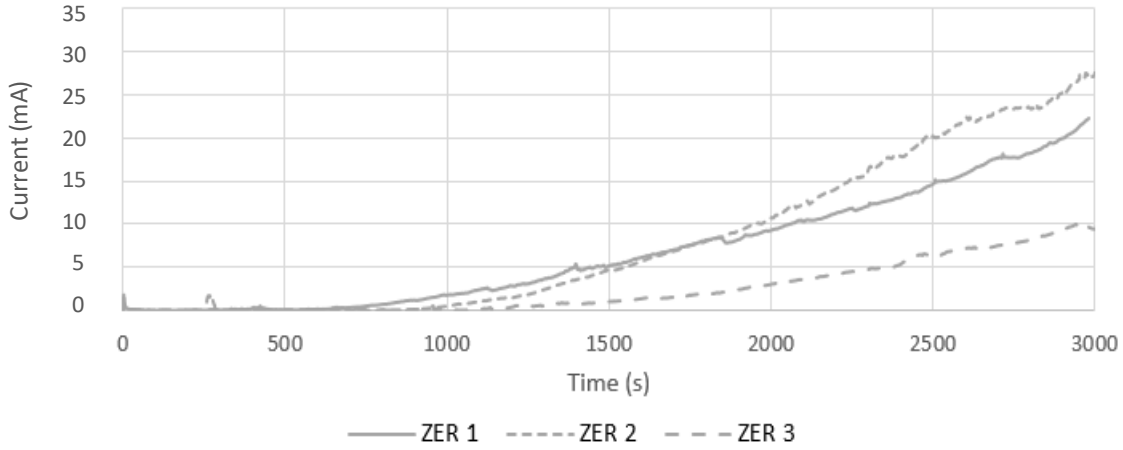

Figure 50: Current vs time of all ZER samples after polarising in 3.5% w/v NaCl at 0.9 V vs SCE, heated to 75 °C and held for 30 minutes

Figure 50 displays the potentiostatic polarisation data for three sets of ZER when heated to 75 °C and held for 30 minutes. All three samples follow a similar pattern but with varying gradients. ZER 1 had a substantial increase in current ~750 s and steadily increases to 22 mA at the end of the hold. ZER 2 rises ~250 s after which also gradually increases up to final current of 27 mA. ZER 3 began to increase ~1330s with the same continuous gradient and a concluding current of 10 mA.

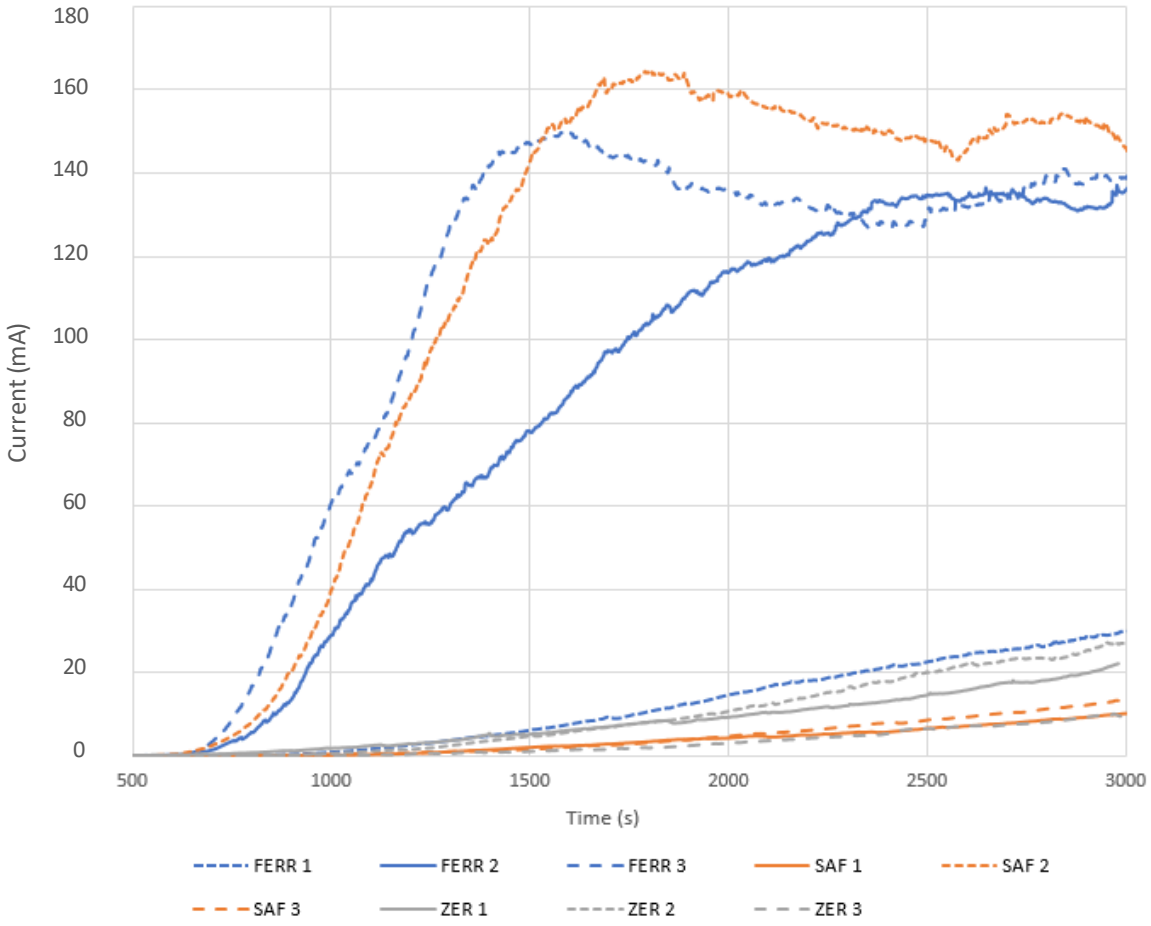

Figure 51: Current vs time of all samples after polarising in 3.5% w/v NaCl at 0.9 V vs SCE, heated to 75 °C and held for 30 minutes

Figure 51 shows data from **Figures 48, 49 & 50** from 500 s to 3000 s. FERR 1 & 2 and SAF 2 had substantial increases in current with little time difference between them, at ~750 s. Between 1000 s and 1500 s, the other samples rose in current with similar gradients, only a 251 mA difference between the six samples after the 30 minute hold. The six data sets were not grouped together in grades and the random order implies little distinction of performance between them.

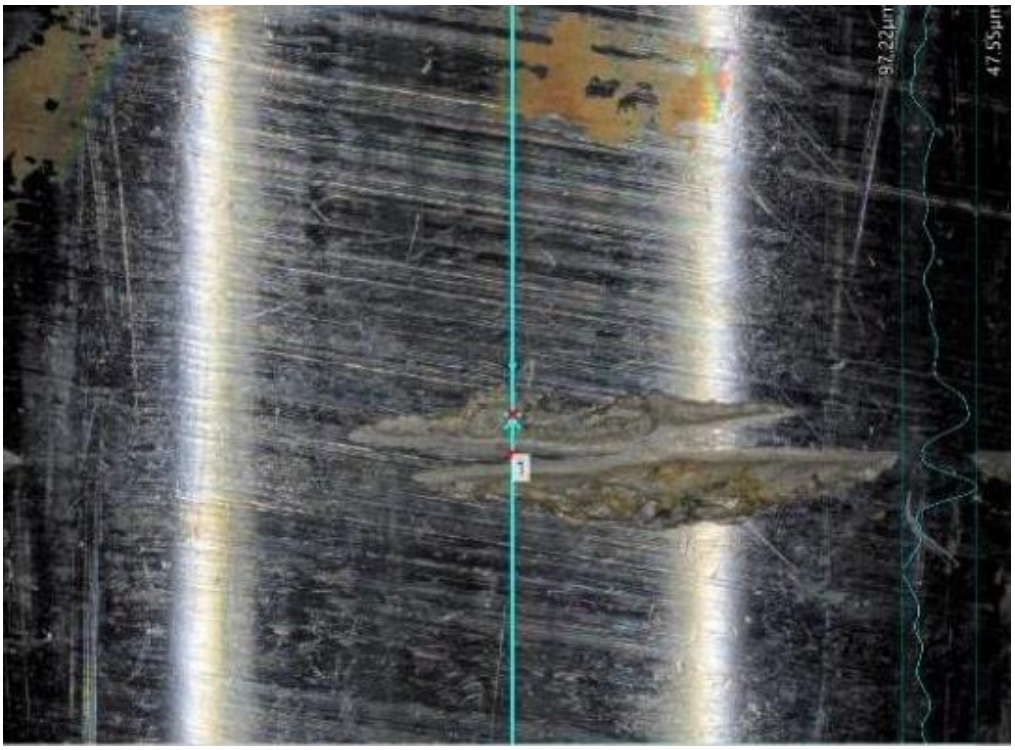

Figure 52: Depth of crevice measurement in FERR 1 after polarising in 3.5% w/v NaCl at 0.9 V vs SCE, heated to 75 °C and held for 30 minutes

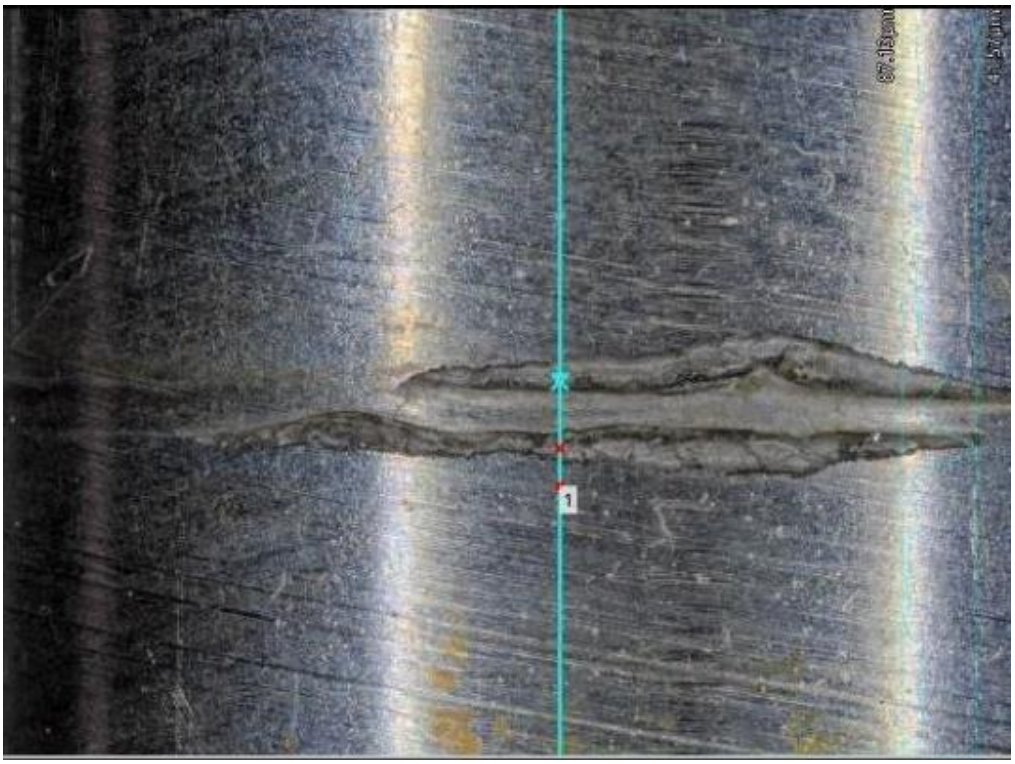

Figure 53: Depth of crevice measurement in SAF 1 after polarising in 3.5% w/v NaCl at 0.9 V vs SCE, heated to 75 °C and held for 30 minutes

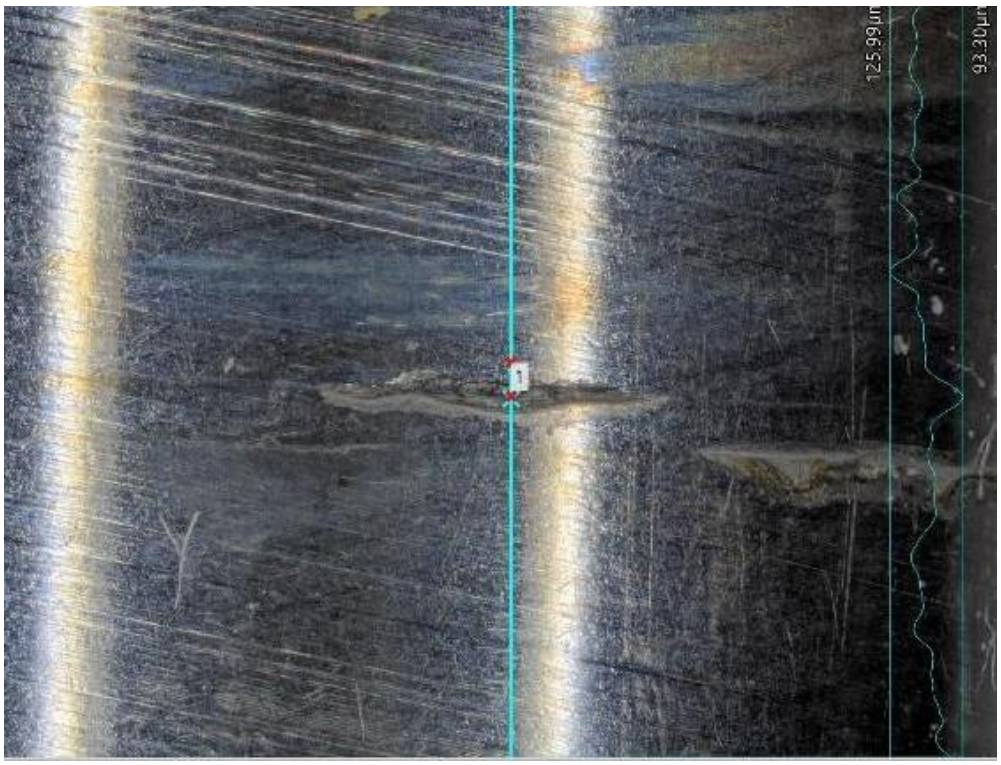

Figure 54: Depth of crevice measurement in ZER 2 after polarising in 3.5% w/v NaCl at 0.9 V vs SCE, heated to 75 °C and held for 30 minutes

Figures 52, 53 & 54 show representative images of the crevice depth measurements and micrographs at one quarter of each sample, after heated to 75 °C and held for 30 minutes. Unlike at 85 °C, the crevice did not form fully around the circumference of the sample, with random dissolution occurring underneath the o-ring instead. Two separate crevices have formed on each sample also, most likely on the sides of where the o-ring was sat. From these images, it seems that SAF had the most corrosion around the circumference due to the crevice spanning most of the quarter.

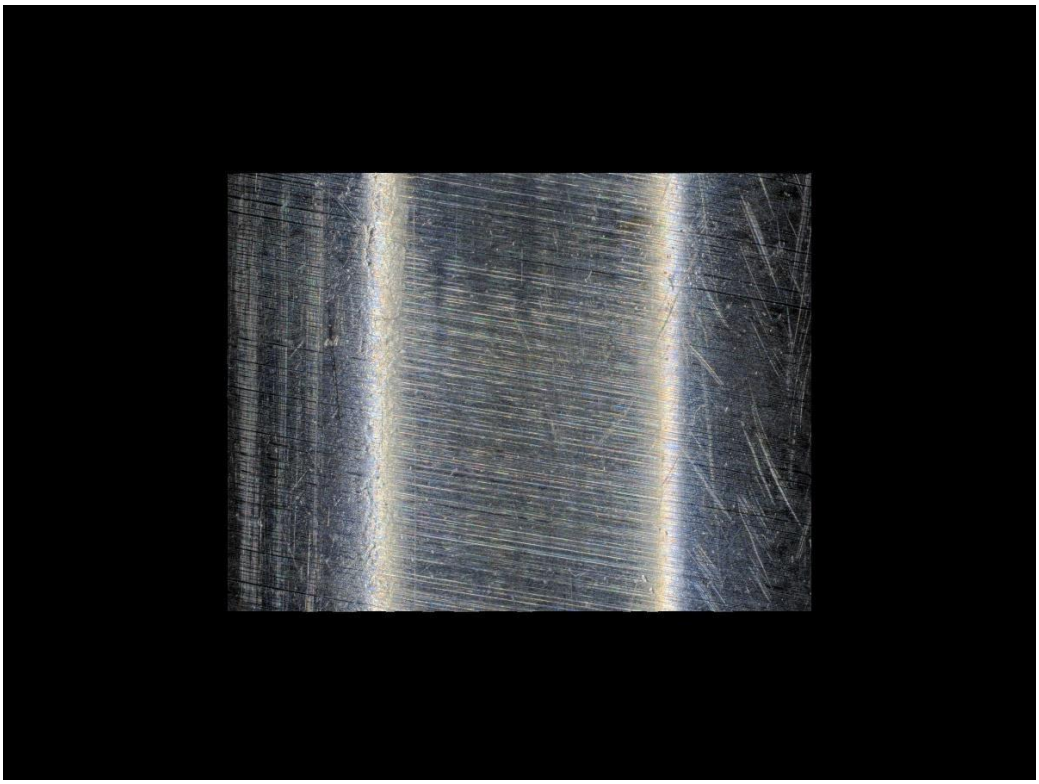

Figure 55: No dissolution observed at one quarter in ZER 3 after polarising in 3.5% w/v NaCl at 0.9 V vs SCE, heated to 75 °C and held for 30 minutes

On some quarters of FERR, SAF & ZER, there was no crevice or dissolution to measure as seen in **Figure 53** with ZER 3 as an example.

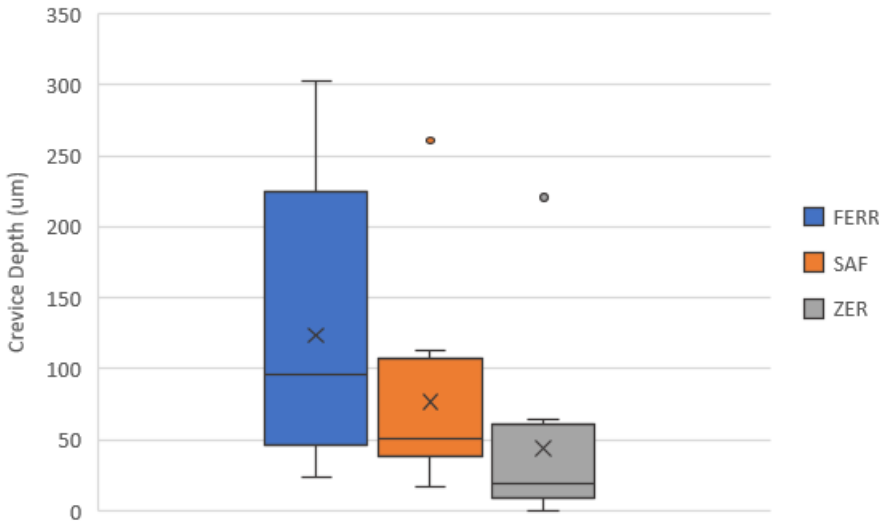

Figure 56: Average depth of crevice formed in each sample after polarising in 3.5% w/v NaCl at 0.9 V vs SCE, heated to 75 °C and held for 30 minutes, with outliers

Figure 56 shows the statistical spread of data between the three grades with respect to depths of the crevice formed at 75 °C. As all three data sets are positively skewed, the median value will be used for comparison instead of the average. FERR had the largest distribution of data and crevice depth also, with a median of 95.97 µm, nearly double that of SAF with a depth of 50.92 µm and nearly five times that of ZER with a median value of 19.44 µm. However, as all three data plots overlap, there is little statistical difference overall. Two outliers have been highlighted with the impact of these seen below in **Figure 57**.

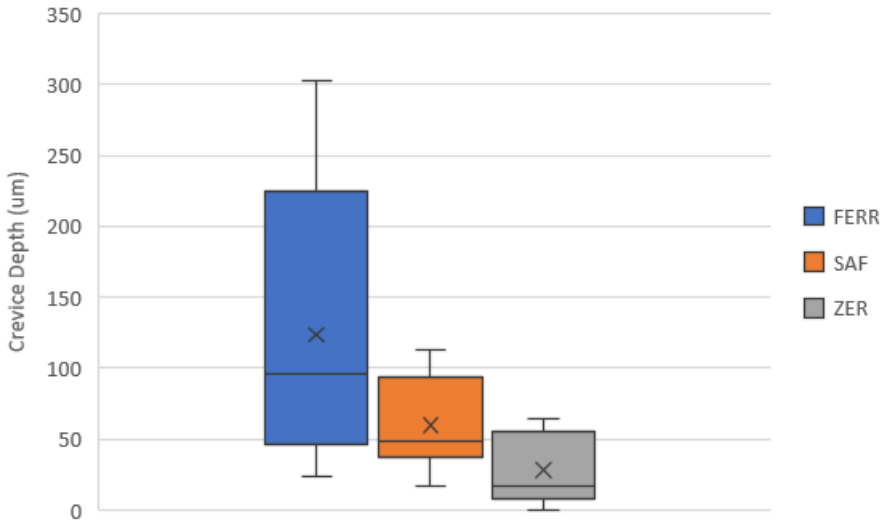

Figure 57: Average depth of crevice formed in each sample after polarising in 3.5% w/v NaCl at 0.9 V vs SCE, heated to 75 °C and held for 30 minutes, without outliers

Figure 57 shows the impact of crevice depths without the outliers calculated in **Figure 56**. Both SAF and ZER median values decreased from 50.92 µm to 48.71 µm and 19.44 µm and 17.41 µm respectively. Both samples have improved performance in comparison to FERR which had the same median of 95.97 µm.

65 °C

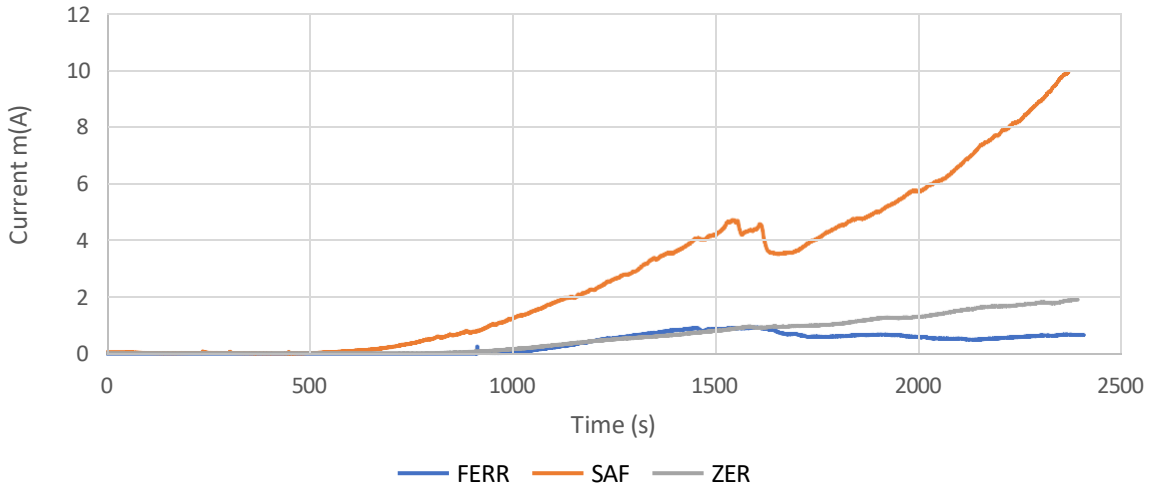

Figure 58: Current vs time of all three samples after polarising in 3.5% w/v NaCl at 0.9 V vs SCE, heated to 65 °C and held for 30 minutes

Figure 58 displays the potentiostatic polarisation data of all three samples when heated to 65 °C and held for 30 minutes. SAF was the first to have a substantial increase in the current ~600s and a steady rise was seen until ~1600 s, after which the current dropped from 5 mA to 3.5 mA. The drop could suggest possible repassivation or metastable pitting. Both FERR and ZER rose in the current ~1000 s and had flat gradients in comparison to SAF, until ~1600 s where FERR had a slight decrease in current and ZER continued to increase. At the end of the hold, SAF had the highest current of the three at 10 mA, followed by ZER of 2 mA and FERR of 1 mA.

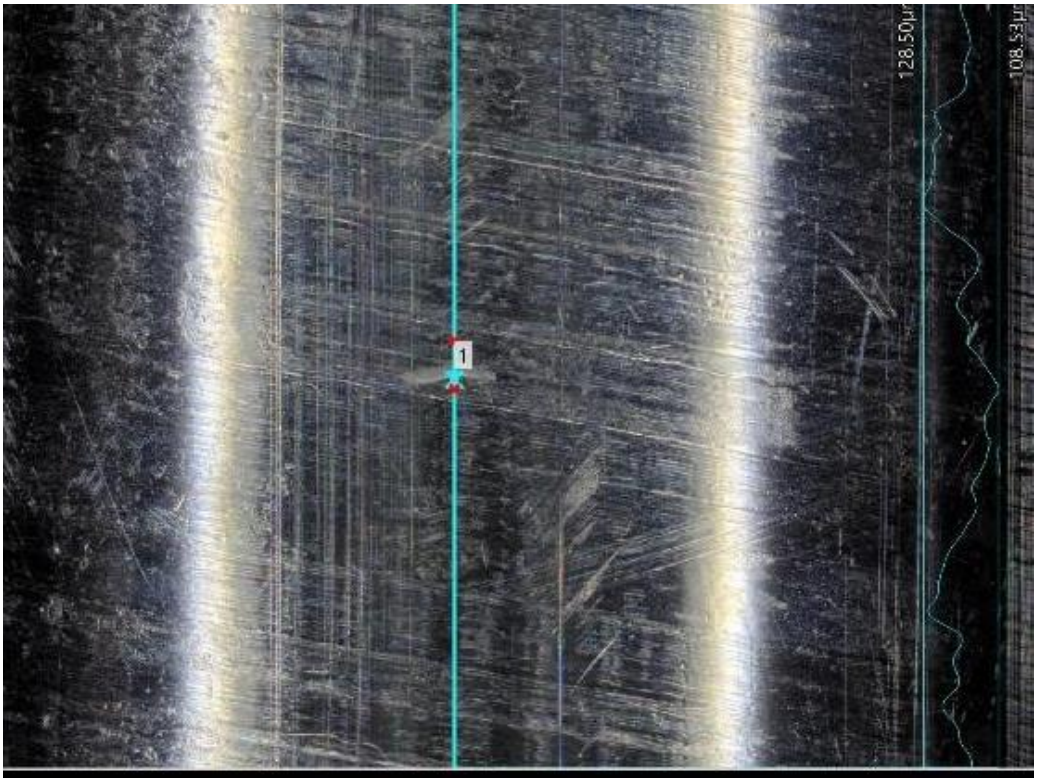

Figure 59: Depth of crevice formed in FERR after polarising in 3.5% w/v NaCl at 0.9 V vs SCE, heated to 65 °C and held for 30 minutes

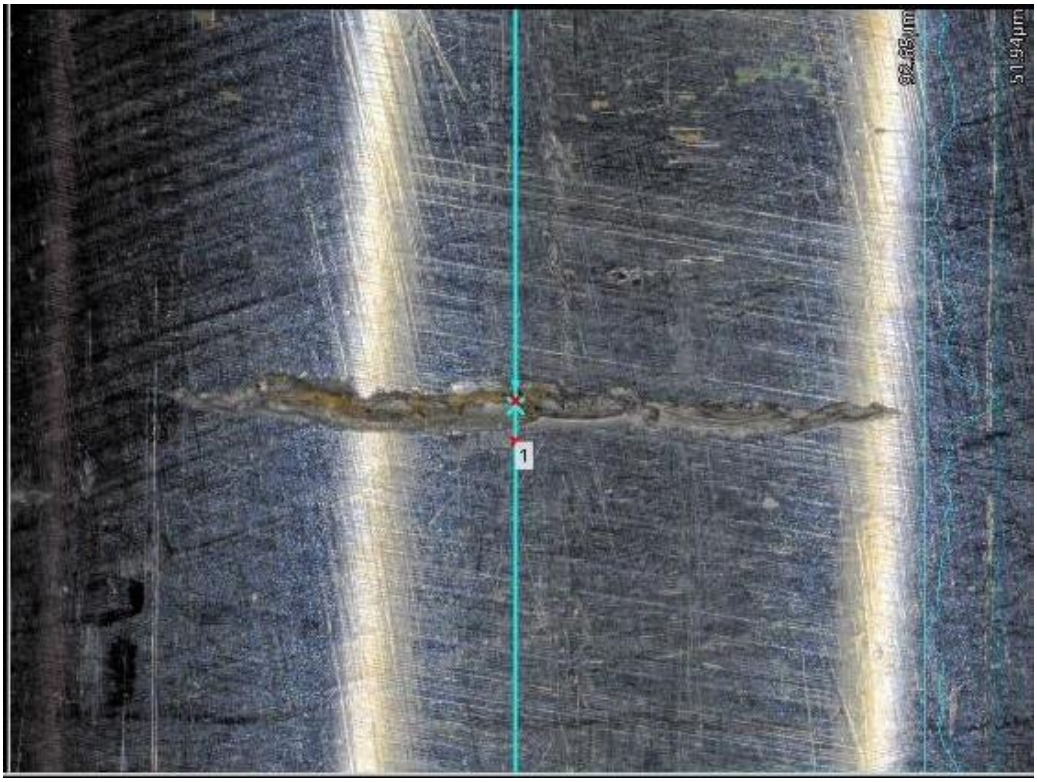

Figure 60: Depth of crevice formed in SAF after polarising in 3.5% w/v NaCl at 0.9 V vs SCE, heated to 65 °C and held for 30 minutes

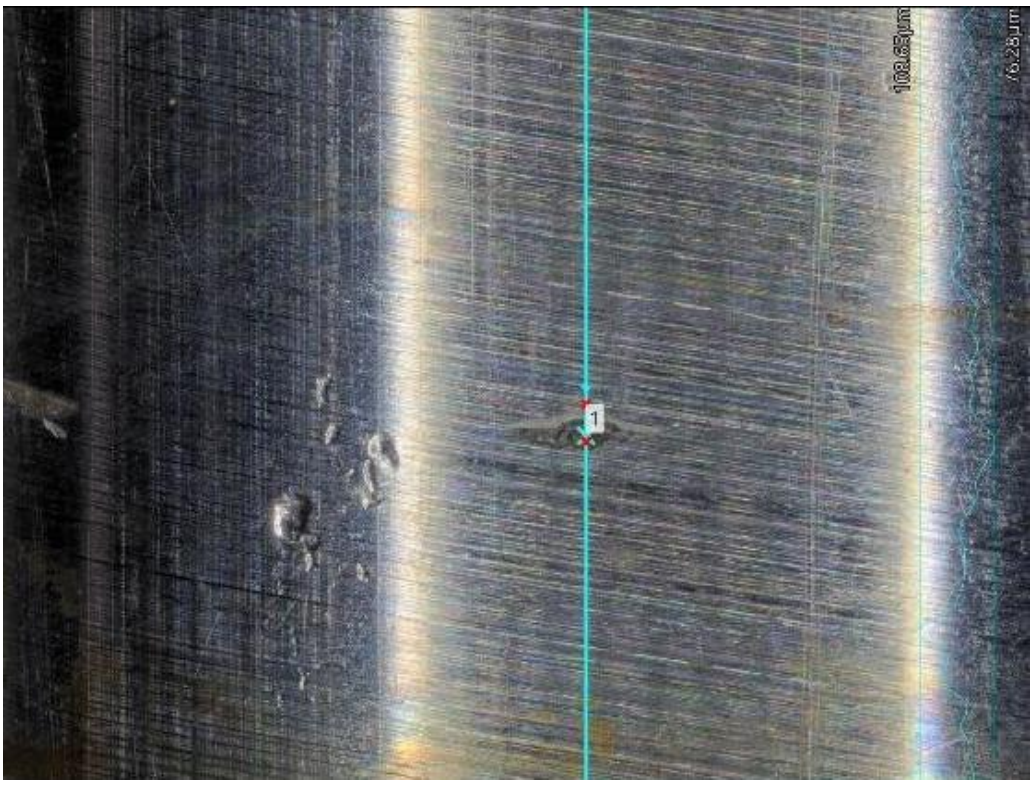

Figure 61: Depth of crevice formed in ZER after polarising in 3.5% w/v NaCl at 0.9 V vs SCE, heated to 65 °C and held for 30 minutes

Figures 59, 60 & 61 show representative images of the crevice depth measurements and micrographs at one quarter of each sample, after heated to 65 °C and held for 30 minutes. Similarly to 75 °C, the crevice did not form fully around the circumference of the sample, with random dissolution occurring underneath the o-ring instead. From these images, it seems that SAF had the most corrosion around its circumference due to the crevice spanning most of the quarter.

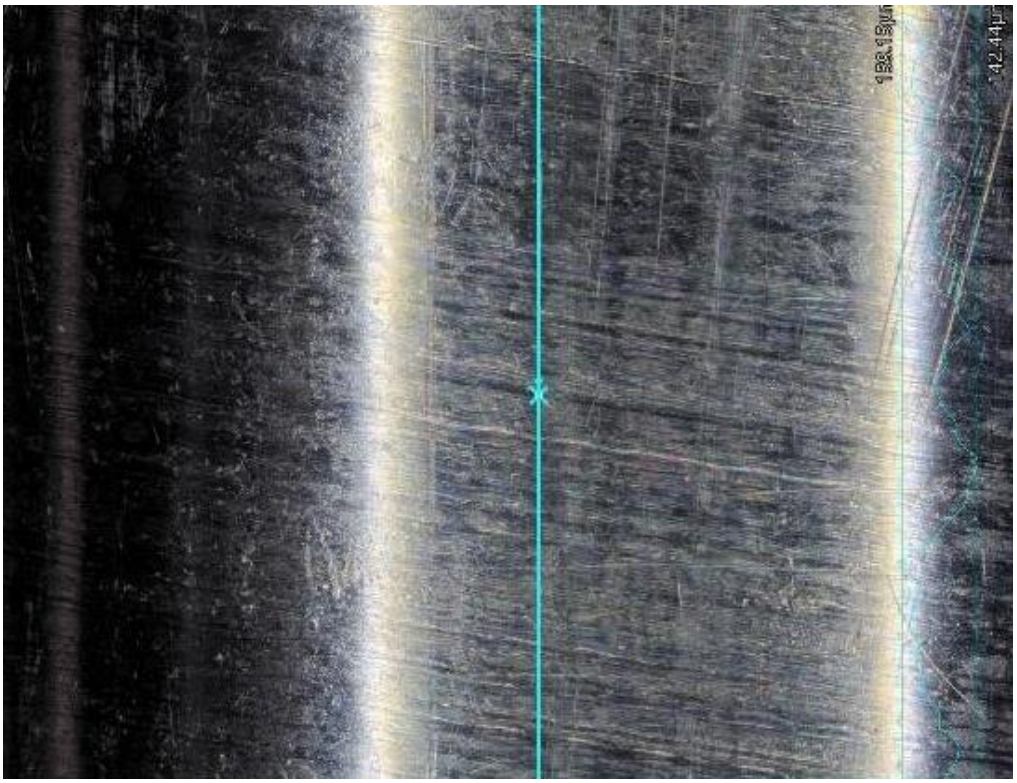

Figure 62: No dissolution observed at one quarter in FERR after polarising in 3.5% w/v NaCl at 0.9 V vs SCE, heated to 65 °C and held for 30 minutes

Similarly to 75 °C, there was no crevice or dissolution on some samples to measure as seen in **Figure 62** with FERR as an example.

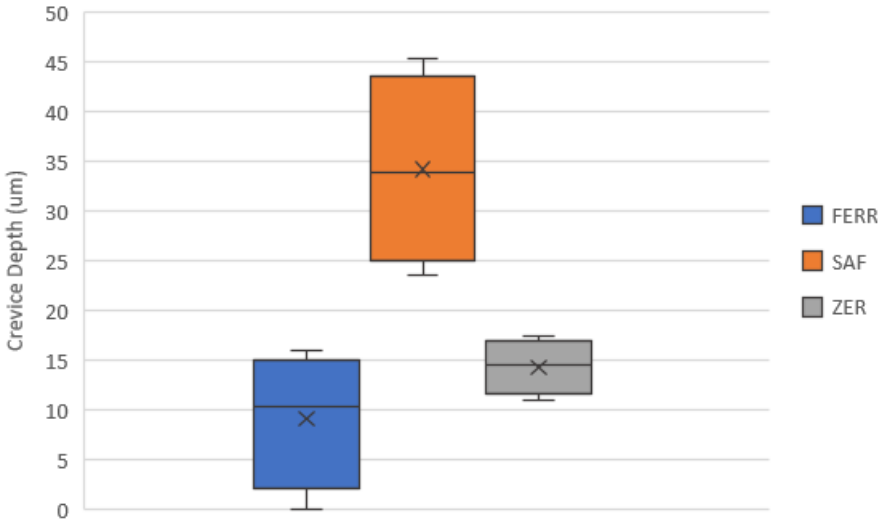

Figure 63: Average depth of crevice formed in each sample after polarising in 3.5% w/v NaCl at 0.9 V vs SCE, heated to 65 °C and held for 30 minutes

Figure 63 shows the statistical spread of data between the three grades with respect to depths of the crevice formed at 65 °C. Due to slightly skewed data seen in FERR, the median value will be used for comparison instead of the average. SAF had the largest distribution and the highest crevice depths with a median of 33.92 µm. A large statistical difference can also be seen between SAF and the other two grades as there is no overlap in the data plots. ZER had the smallest variability in the data although FERR had the lowest median crevice depth of 10.28 µm in comparison to 14.46 µm of ZER.

Comparison of Three Temperatures

This is linked to the prior section of crevice corrosion susceptibility of SDSS at temperature. This section will be comparing all three temperatures together for each sample.

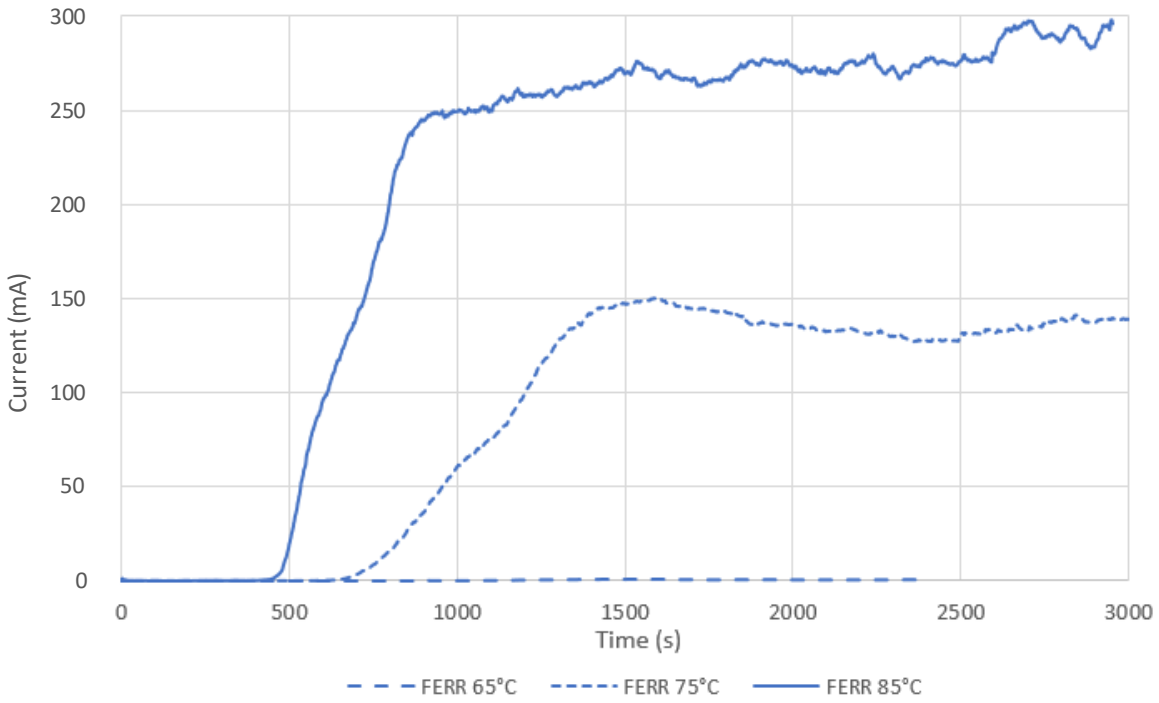

Figure 64: Current vs time of three FERR samples after polarising in 3.5% w/v NaCl at 0.9 V vs SCE, heated at three temperatures and held for 30 minutes

Figure 64 shows the potentiostatic polarisation data for FERR at 65 °C, 75 °C and 85 °C after being held at each temperature for 30 minutes. There is a clear difference between each sample with the gradients and maximum currents varying significantly at each temperature. FERR 85 °C started to rise in current ~450 s, FERR 75 °C increased ~200 s later and FERR 65 °C rose ~1000 s but hardly increased in current at all, with a final current of 1 mA, a significant difference to the other temperatures. FERR 85 °C had a steep gradient up to 250 mA which then gradually increased up to 300 mA until the end of the hold. FERR 75 °C had a shallower gradient reaching 150 mA until plateauing in the holding region, half the current that was seen for FERR 85 °C.

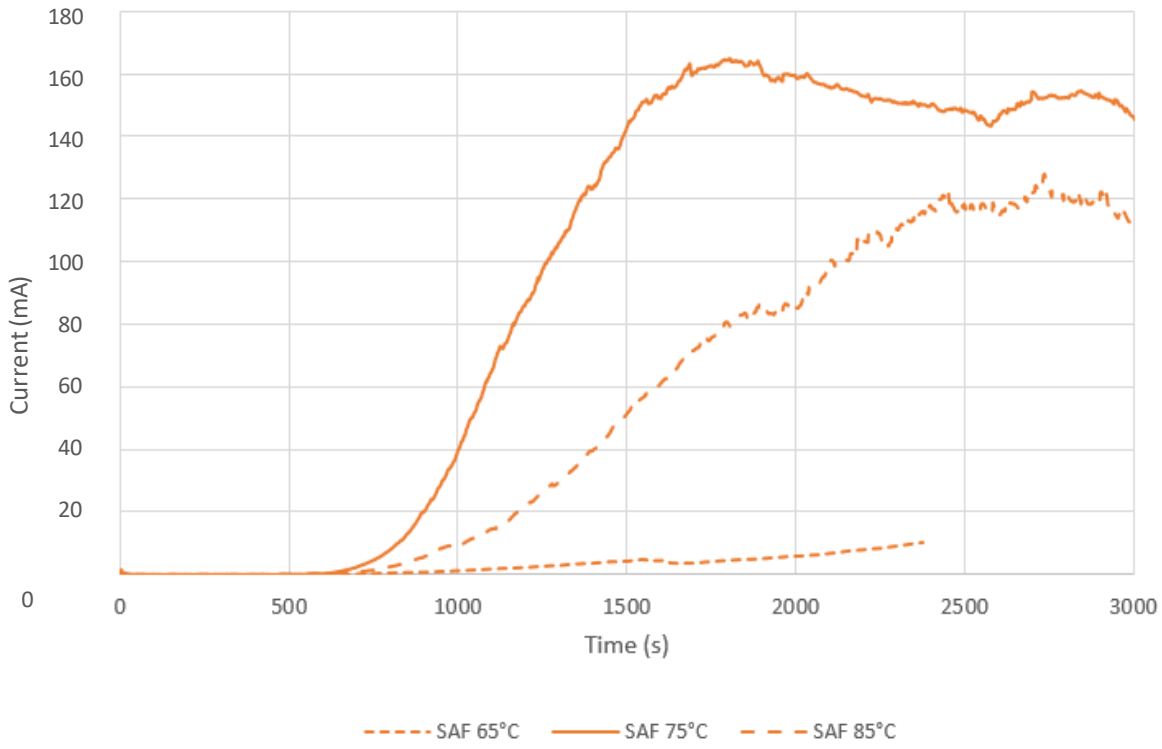

Figure 65: Current vs time of three SAF samples after polarising in 3.5% w/v NaCl at 0.9 V vs SCE, heated at three temperatures and held for 30 minutes

Figure 65 shows the potentiostatic polarisation data for SAF at 65 °C, 75 °C and 85 °C after being held at each temperature for 30 minutes. There is a clear difference between each sample with the gradients and currents varying significantly at each temperature. SAF 75 °C & 85 °C started to rise in current at similar times ~100 s apart with SAF 65 °C rising ~1000 s. SAF 85 °C had a steep gradient up to ~160 mA which then gradually decreased to 150 mA until the end of the hold. SAF 75 °C had a shallower gradient reaching 120 mA until plateauing in the holding region, not dissimilar to the current that was seen for SAF 85 °C. SAF 65 °C had the flattest gradient in comparison, ending the hold at 10 mA, a considerable difference to the other temperatures.

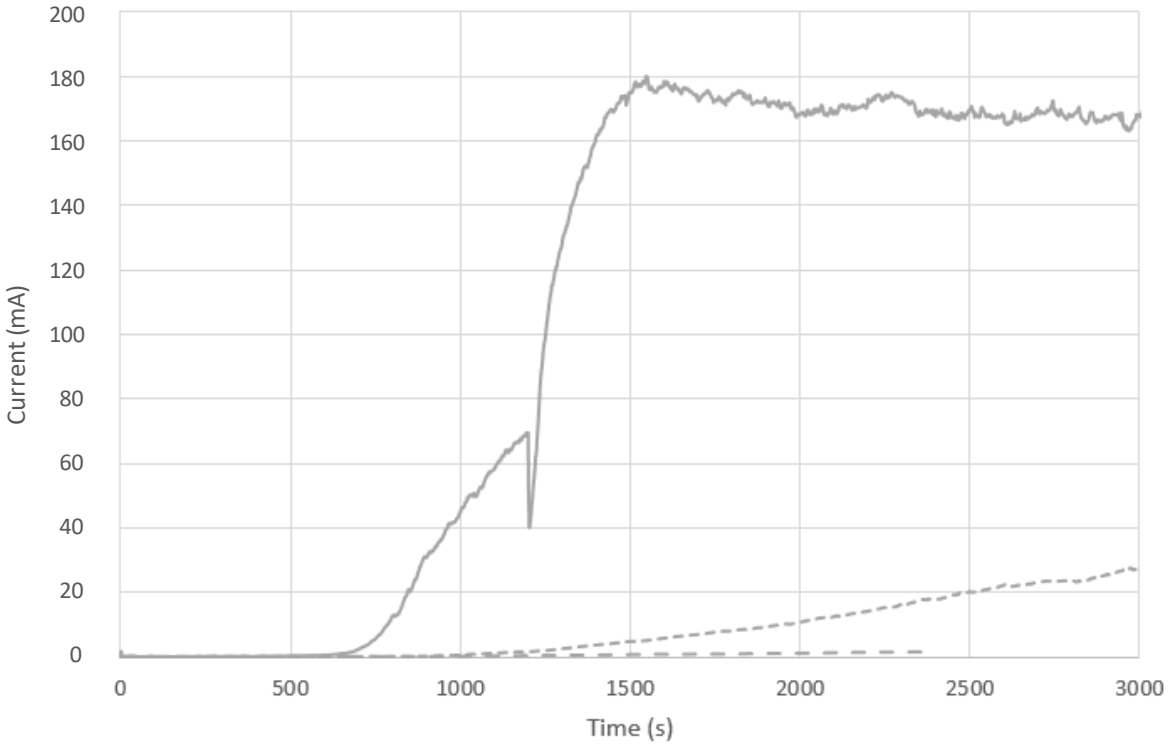

Figure 66: Current vs time of three ZER samples after polarising in 3.5% w/v NaCl at 0.9 V vs SCE, heated at three temperatures and held for 30 minutes

Figure 66 shows the potentiostatic polarisation data for ZER at 65 °C, 75 °C and 85 °C after being held at each temperature for 30 minutes. There is a clear difference between each sample with the gradients and currents varying significantly at each temperature. ZER 85 °C began to rise in current ~700 s with ZER 75 °C rising ~500s afterward and ZER 65 °C rose ~1000 s but hardly increased in current at all, with a final current of 2 mA, a significant difference to the other temperatures. ZER 85 °C had a steep gradient up to 180 mA which plateaued in the holding region at 170 mA, the distinct decrease seen in the 1000 s to 1500 s had been discussed in the previous section. ZER 75 °C had a much shallower gradient, with a concluding current of 30 mA, a vast disparity to ZER 85 °C.

Crevice Corrosion Susceptibility Mass Loss

This section continues using data from samples in the crevice corrosion tests in the previous section.

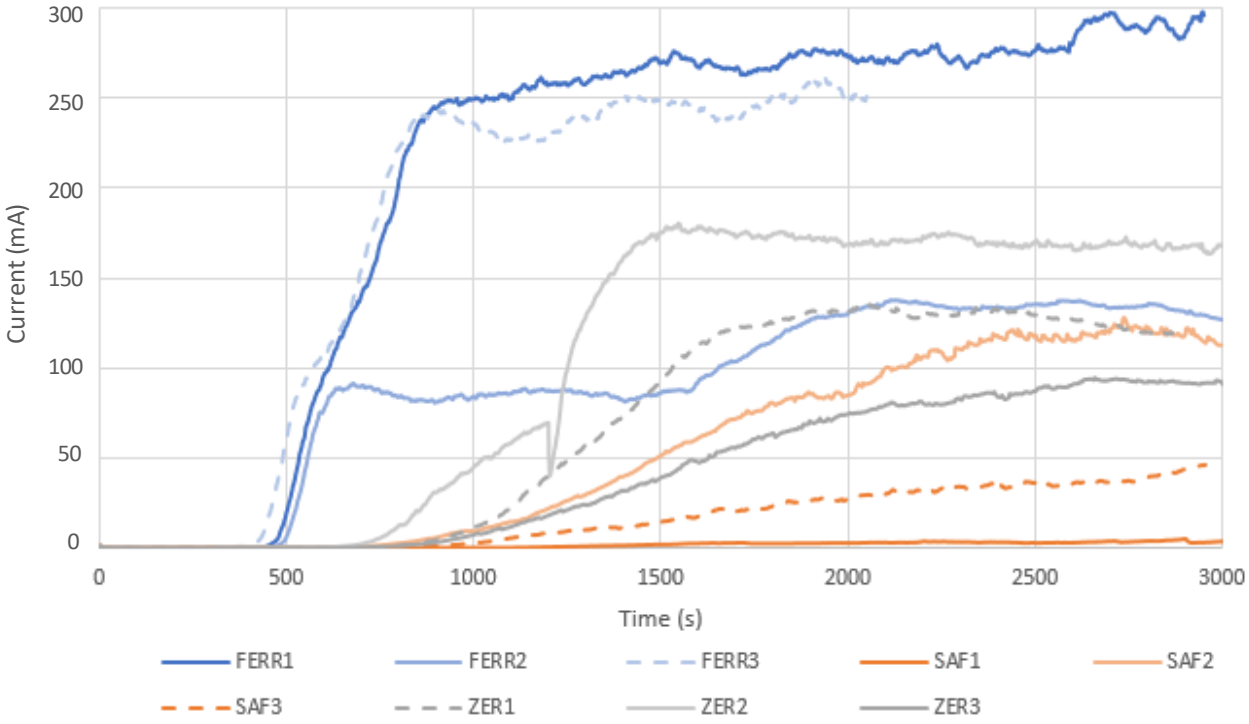

Figure 67: Current vs time of all samples after polarising in 3.5% w/v NaCl at 0.9 V vs SCE, heated to 85 °C and held for 30 minutes

Using **Figure 67**, charge (Q) was calculated for each sample by integrating under each curve and using equations (9) & (10) of Faraday's Law of Electrolysis to determine the mass loss. The data obtained from crevice depths can be used to estimate mass loss also by using equations (13), (14), (15), (16) & (17). The two methods have been compared and disparities between them discussed.

85 °C

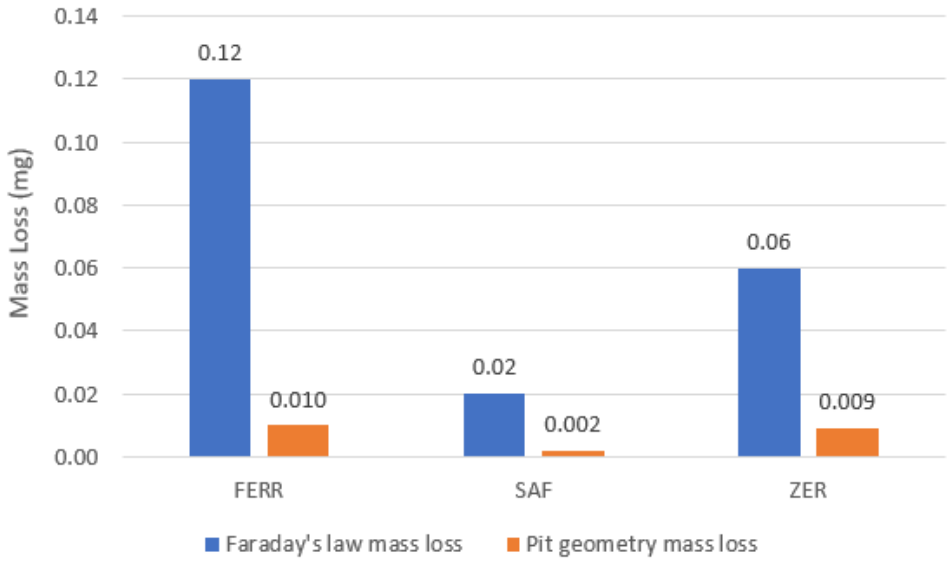

Figure 68: Faraday's Law and crevice geometry average mass loss for each sample at 85 °C

Using the values calculated using Faraday's Law and crevice geometry, the mass loss for each sample can be seen in **Figure 68**. FERR had the largest mass loss from both methods used with a significant disparity between each value, 0.11 mg. SAF and ZER had less variation in mass loss values with differences of 0.018 mg and 0.05 mg.

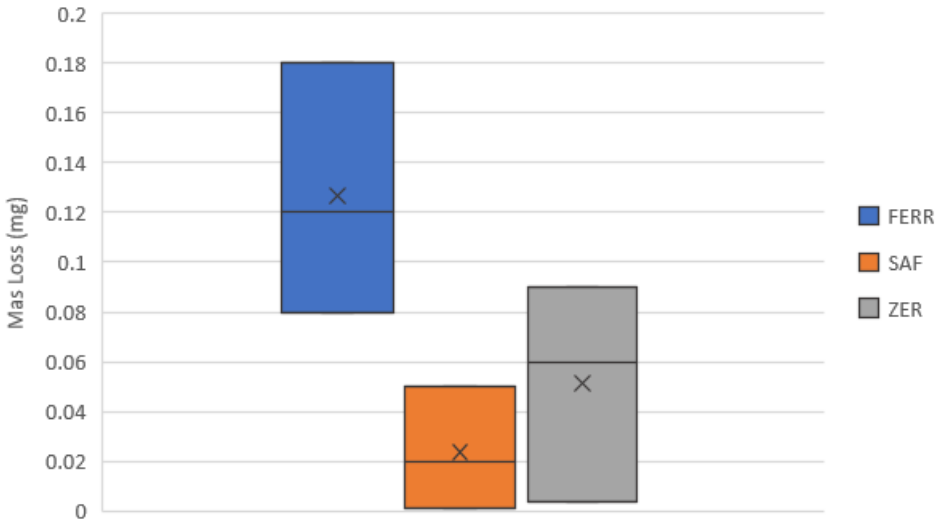

Figure 69: Faraday's Law mass loss for each sample at 85 ℃

From **Figure 69**, FERR had a wider distribution in Faraday's Law mass loss across samples in comparison to ZER and SAF. FERR had the largest mass loss with an average of 0.12 mg with SAF and ZER with similar mass loss of 0.02 mg and 0.06 mg.

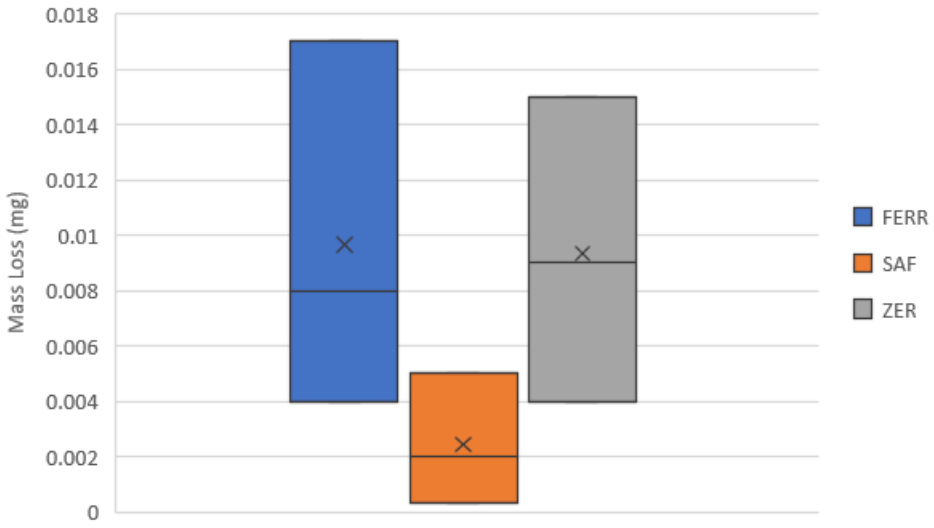

Figure 70: Pit geometry mass loss for each sample at 85 °C

From **Figure 70**, FERR and ZER had significantly wider distribution in comparison to SAF, implying unpredictability of these grades when calculating mass loss from its pit geometry. ZER had the largest mass loss with a median of 0.009 mg with FERR slightly smaller with a mass loss of 0.008 mg. SAF had small variation in the data with a low mass loss of 0.002 mg.

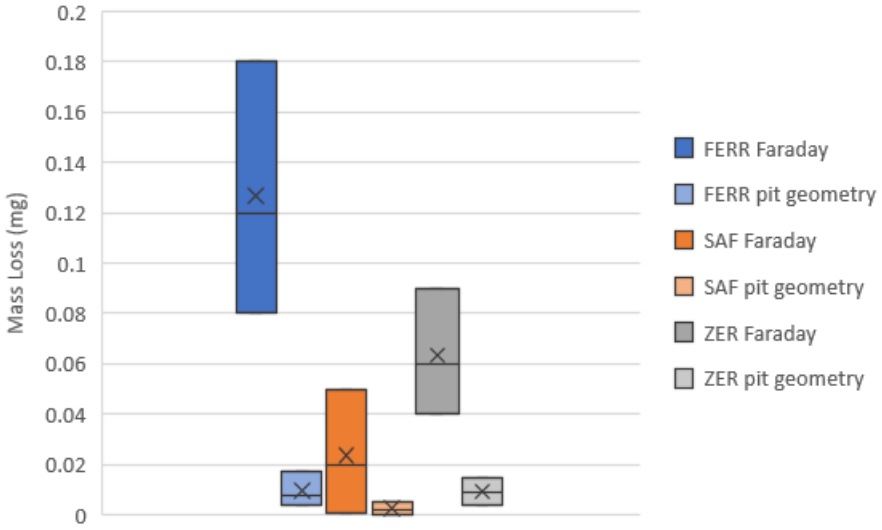

Figure 71: Faraday's Law and pit geometry mass loss for each sample at 85 °C

From **Figure 71**, both FERR and ZER have significant disparities between Faraday's Law and pit geometry calculations with the distribution of data for Faraday values much wider and both averages statistically different, 0.12 mg and 0.06 mg respectively. Both values calculated for SAF are similar in terms of distribution and average, with a 0.02 mg difference. For all three grades, the average values were higher for Faraday's Law than the pit geometry.

75 °C

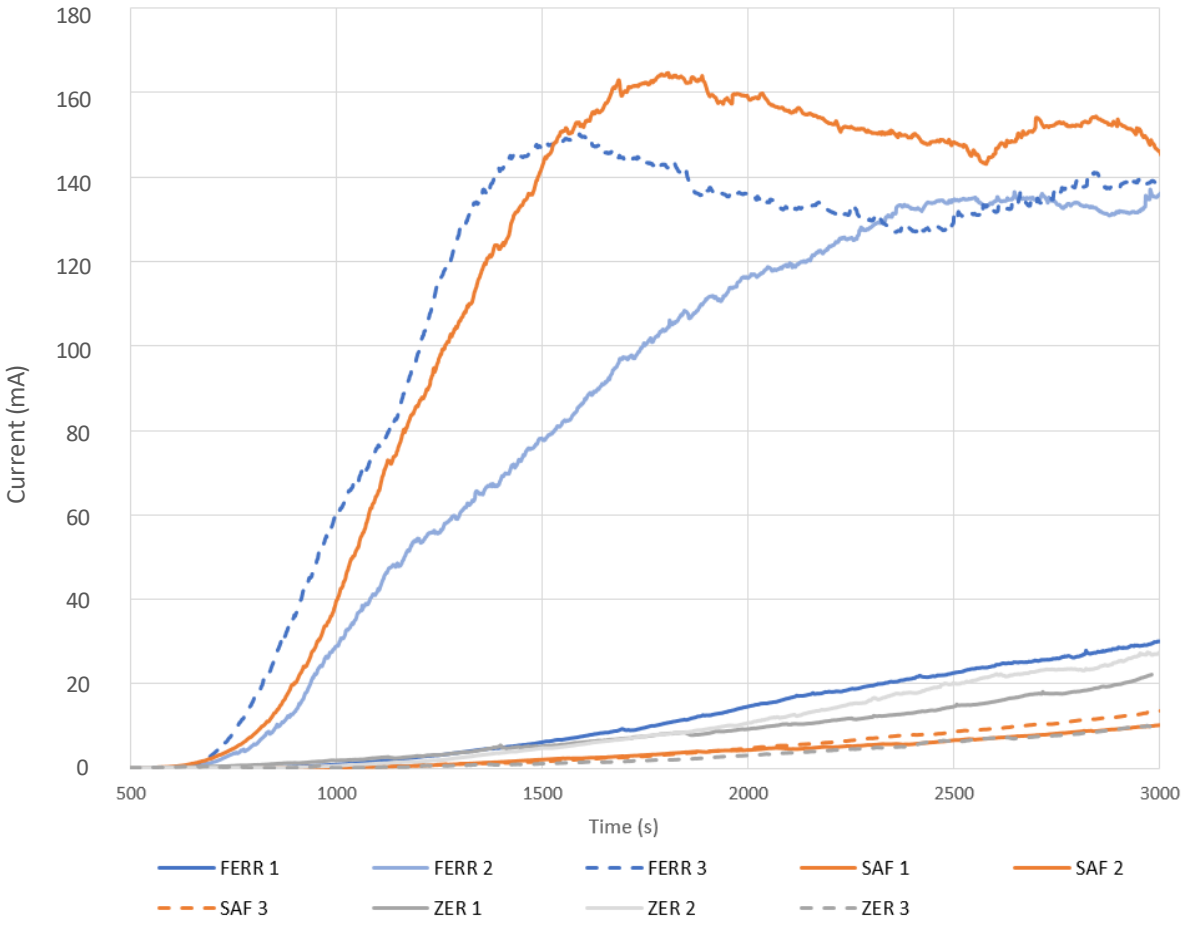

Figure 72: Current vs time of all samples after polarising in 3.5% w/v NaCl at 0.9 V vs SCE, heated to 75 °C and held for 30 minutes

Mass loss from Faraday's Law and pit geometry was calculated using the same method from the previous section of 85 °C but with the data recorded in **Figure 72**.

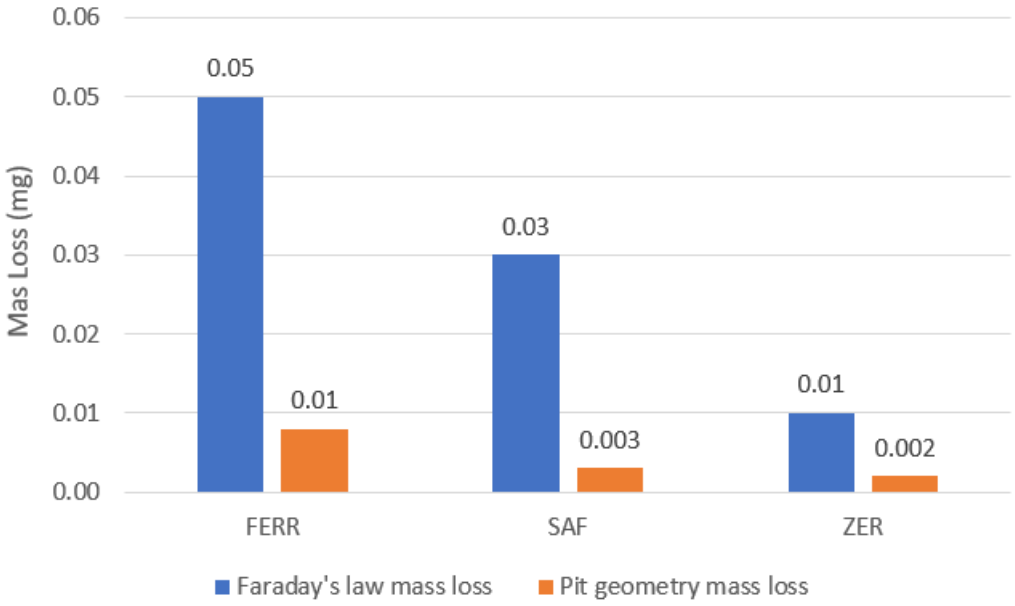

Figure 73: Faraday's Law and pit geometry mass loss for each sample at 75 °C

Using the values calculated using Faraday's Law and pit geometry, the mass loss for each sample can be seen in **Figure 73**. FERR had the largest mass loss from both methods used with a significant disparity between each value, 0.042 mg. SAF and ZER had less variation in mass loss values with differences of 0.27 mg and 0.008 mg.

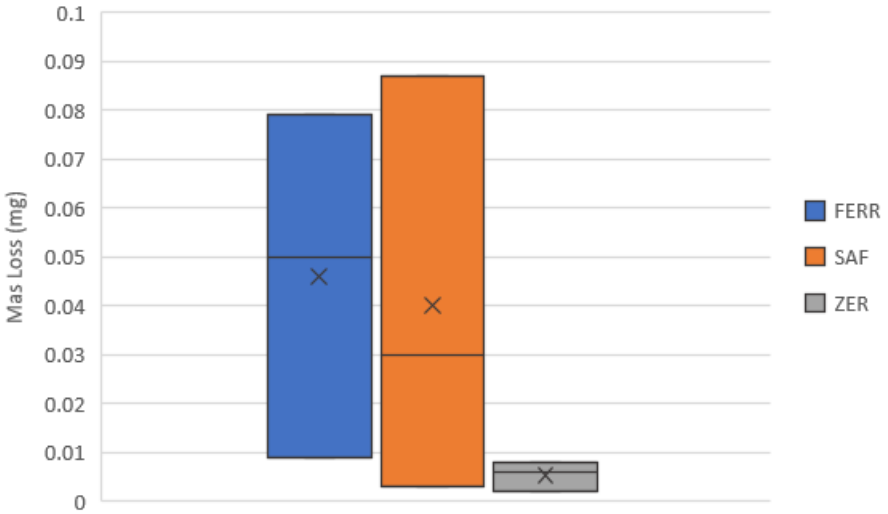

Figure 74: Faraday's Law mass loss for each sample at 75 ℃

From **Figure 74**, SAF and FERR had a wider distribution in Faraday's Law mass loss across samples in comparison to ZER. FERR had the largest mass loss with an average of 0.05 mg, SAF with 0.03 mg and ZER having a significantly lower mass loss of 0.006 mg.

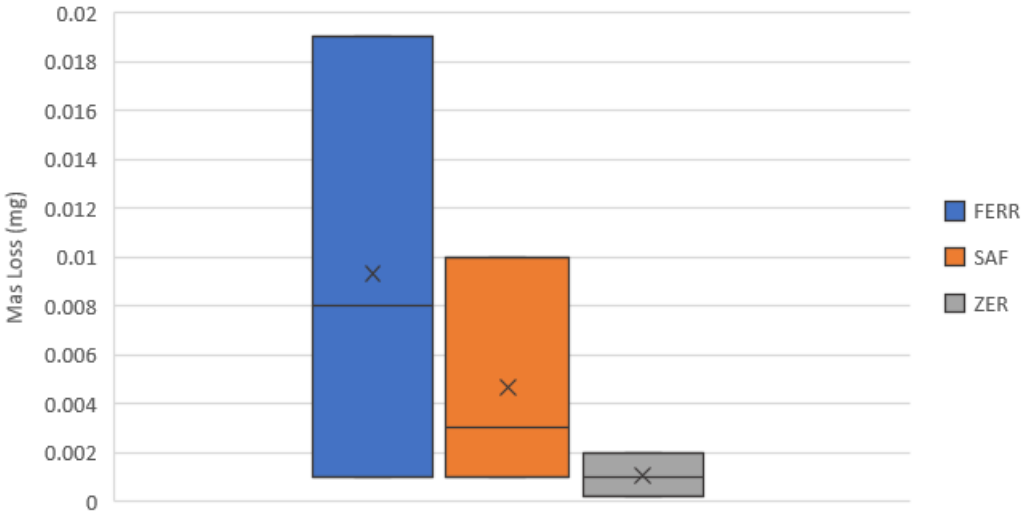

Figure 75: Pit geometry mass loss for each sample at 75 ℃

From **Figure 75**, FERR and SAF had significantly wider distribution in comparison to SAF and ZER, implying unpredictability of these grades when calculating mass loss from its pit geometry. FERR had the largest mass loss with a median of 0.008 mg with SAF and ZER considerably smaller with a mass loss of 0.003 mg and 0.001 mg.

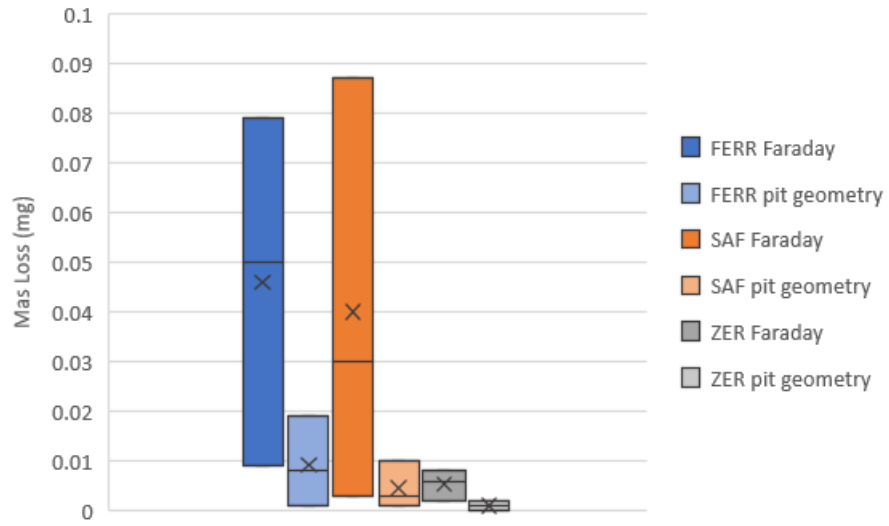

Figure 76: Faraday's Law and pit geometry mass loss for each sample at 75 °C

From **Figure 76**, both SAF and FERR have significant disparities between Faraday's Law and pit geometry calculations with the distribution of data for Faraday values much wider and both averages considerably different, 0.034 mg and 0.040 mg respectively. Both values calculated for ZER are similar in terms of distribution and average, with a 0.009 mg difference. For all three grades, the average values were higher for Faraday's Law than the pit geometry suggesting something influenced this calculation.

65 °C

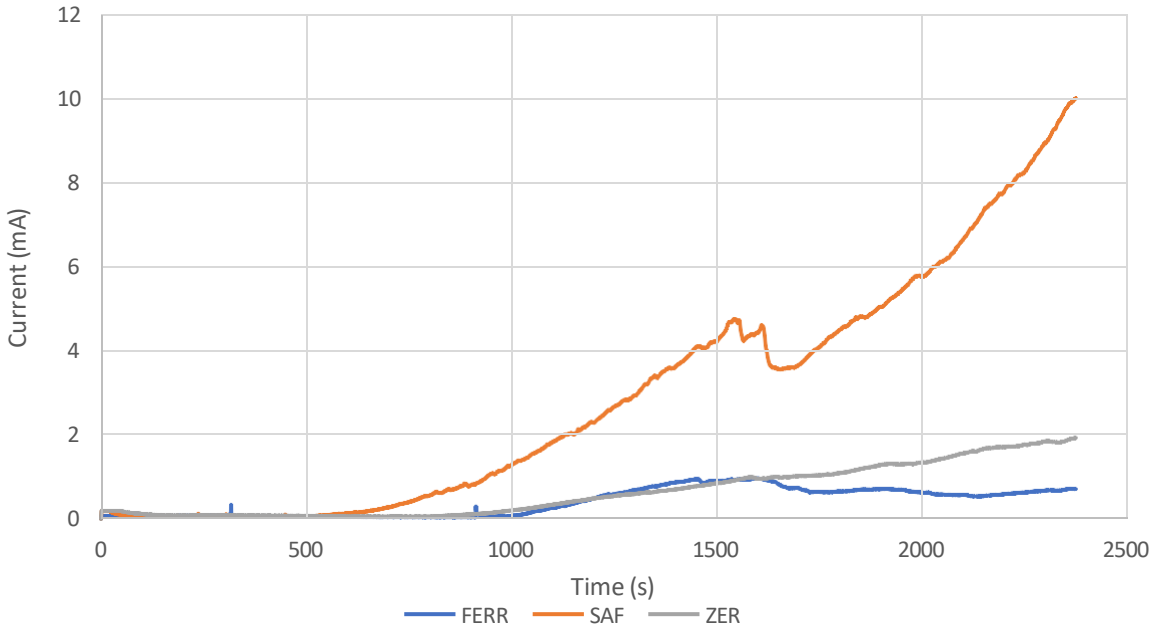

Figure 77: Current vs time of all samples after polarising in 3.5% w/v NaCl at 0.9 V vs SCE, heated to 65 °C and held for 30 minutes

Mass loss from Faraday's Law and pit geometry was calculated using the same method from the previous sections of 85 °C & 75 °C but with the data in **Figure 77**.

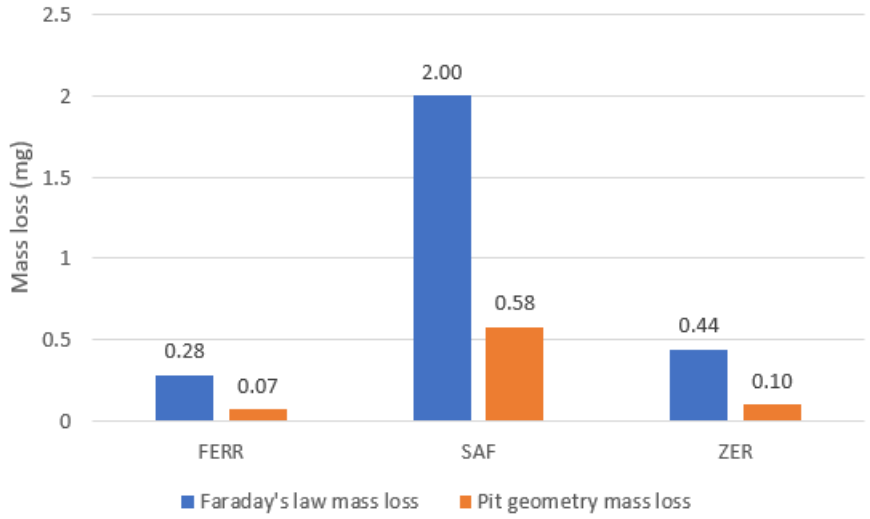

Figure 78: Faraday's Law and pit geometry mass loss for each sample at 65 °C

Using the values calculated using Faraday's Law and pit geometry, the mass loss for each sample can be seen in **Figure 78**. SAF had the largest mass loss from both methods used with a significant disparity between each value, 1.42 mg. ZER and FERR had less variation in mass loss values with differences of 0.34 mg and 0.021 mg.

3.0 DISCUSSION

4.1 Influence of Temperature on CPT and Pit Initiation

FERR had an average CPT of 77 °C and the highest final recorded currents of 14 mA and 8 mA. These values led to FERR having the highest average frequency of pits with 204 pits and corroded area of 0.02488 mm^2. A large statistical difference was seen in both data sets due to no overlap in the data plots with SAF and ZER. From these results, it could be predicted that FERR would have significantly deeper pits and although FERR does have the widest range of pit depths, the median, 64.44 µm, is not vastly dissimilar to SAF and ZER, only 15.06 µm deeper than smallest median seen for SAF of 46.5 µm. The difference in the composition of FERR is increased $Cu\ wt\%$ and extensive research Roscoe *et al.* [71] found that Cu increased the pitting corrosion resistance. Although Cu has positive effects, it segregates in the austenite phase as seen in **Figure 1** where the PREext is higher than the ferrite phase. However, pitting usually initiates in the ferrite phase and as such, the effect of Cu is reduced [7].

A large amount of dissolution was observed on the circumference on FERR, seen in **Figure 25**. This was unlike the other two grades which did not exhibit the same behaviour. Preferential corrosion of the outside circumference could suggest that the current density around the edge was higher, or that the crystallography differs between each grade. The outside cylindrical surface was assumed to be comparable across each specimen in the as received manufactured condition. Both factors were not explored in this paper but could be recommendations for future research to understand these. Due to the technique used on the Keyence microscope, the area on the edges was selected as one pit rather than multiple, resulting in a larger area included in the results. This would have attributed to the higher values of corroded area and wider distribution of FERR data seen in **Figures 27 & 29** respectively.

Of the three grades, SAF had the lowest CPT of 76 °C. However, SAF also had the lowest final current measurements of 0.9 mA and 0.4 mA, corresponding with this grade having the lowest frequency of pits at 38 pits, the lowest corroded area of 0.00940 mm^2 and the smallest crevice depths of 46.5 µm. When the temperature surpasses the CPT, the metal begins to corrode so it could be assumed that the lower the CPT, the higher amount of dissolution. In this case, SAF had a lower CPT but paired with low currents, the sample did not corrode as predicted. SAF has the lowest Cu wt% which would not contribute to same resistance in research as described

above for FERR, although it does have increased Mn, N and Mo wt% in comparison to the other grades which all are known for their properties improving corrosion resistance.

The average CPT measured for ZER was 80 °C with both ZER samples with final currents just above 3.5 mA. As these values are slightly higher than for SAF, this would correlate to ZER having a similar frequency of 85 pits, corroded area of 0.01056 mm^2 and a median pit depth of 55.79 µm. The composition of increased W wt% has not seemed to have impacted ZER's performance as well as stated in multiple papers [79] [80] [82] [84]. The CPT is 3-4 °C higher than the other grades which Eirik B. Haugan *et al.* [81] stated that W raises the CPT by increasing E_p whilst lowering i_p. It would have been expected to have a major performance advantage, but this was not observed. The added W may have decreased the overall size and depth of pits, although this cannot solely be attributed due to the increase in Cu wt% in the composition also.

Denny. A. Jones [18] stated that both Ni and Cr cations hydrolyse to acid chlorides in reactions similar to the corrosion equation (4) mentioned previously. Cr strongly passivates the outer surface but aggravates pitting corrosion by hydrolysing to a lower pH within the pit than Fe. Ni does not hydrolyse as strongly, which may result in improved pitting resistance. Given the ranges that the compositional additions can be, an average has been taken. SAF and ZER both have 25 wt% Cr and 7 wt% Ni whereas FERR has 25.5 wt% Cr and 6 wt% Ni. These are not large differences although the PREn calculations have shown that small changes to the composition can impact the corrosion tendency.

The lacy pits imaged in SAF 1 and ZER 2, seen in **Figure 30,** indicates how the technique used to measure the pit depths was not highly accurate. Due to the material partially covering the surface, the true depth was obscured, and the light of the microscope could not reach the bottom of the pit. These depths were removed from the measurements and other pits included, thus reducing the random bias from the pits that were chosen. No quantifiable data could be taken from the lacy pits which may have altered the overall results in each sample. The data is an approximation based on the technique used although any error incurred would be carried over with each sample so can still be used comparatively.

Two outliers in the pit depths can be seen in **Figure 28**, one for FERR and the other for ZER. The impact of these were evaluated and found to improve the overall performance of the two

grades when the outliers were not taken into consideration. The medians of both decreased by a minimum of 2 µm, as well as the variability of both grades with the distribution of data for ZER reducing significantly. As these are likely to be true outliers and represent natural variation in the samples, these shall not be excluded from the data set although measurement inaccuracy as discussed previously, lacy pits etc., could still be a possibility.

Fluctuation in current was seen in **Figure 23** for both SAF and ZER, whilst FERR had a steady increase throughout. These fluctuations can refer to the growth of metastable pits which are represented by a slow rise in current as the area of the pit increases, followed by a drop in current. This is due to diffusion being controlled through the apertures of the lacy covering of the pit. The initial current spike is reported to be the nucleation event of growth of a metastable pit succeeding it [29]. Before the first substantial increase in current, SAF had a distinct rise in current ~70 °C which then decayed almost immediately to the background current. There is no slow rise in current following nucleation seen with metastable propagation and this is believed to be nucleation of a pit which repassivates immediately after nucleation without any propagation [34]. It can be assumed from previous work [66] that small pits were the result of metastable events that repassivated during the tests. Larger pits observed were assumed to be mostly the result of stable pit growth terminated only by the end of the test. It is considered possible that some of the large pits had repassivated before the end of the test and could be referred to as metastable. The lacy pits mentioned previously were not quantified for each sample so it cannot be confirmed which grade had the most. Although the images taken from SAF and ZER correspond to the behaviour of metastable pitting seen in the current vs time graphs.

The micrographs in **Figure 24** represent the data discussed above accurately. It can clearly be seen that FERR had the highest frequency of pits with the largest area corroded, followed by ZER and then SAF. All samples had evidence of corrosion on the surface seen in the darker, circular shapes but particularly in SAF. This links to the potentiostatic data seen in **Figure 23**, in which frequent fluctuations in current were observed, discussed previously as a result of metastable pitting. These variations can also be seen in ZER but to a lesser extent whereas FERR mostly had steady increases in current. The corrosion features on the sample face were included in the frequency of pits measurements, but a depth value could not be obtained as the pit had not developed enough. This would have skewed the number of pits measured in all

samples as all had corrosion evident on the surface, but no depths able to be measured as a result.

Influence of Temperature on Mass Loss in Aerated Conditions

Some assumptions were used when calculating mass loss using the pit geometry model. All pits have been assumed hemispherical which J. Soltis [39] reported that most pits are not identical and form in different shapes. He found that square and hexagonal etch pits were more likely to be found at low potential and pits of circular edges with a dull or polished interior were found at higher potentials.

As mentioned previously, many lacy pits were identified in the samples which could have affected the ability of the technique used to accurately measure the pit depth. Furthermore, metastable pitting affected the overall pit count due to the technique including dark areas in the samples that would not be classed as pits. These all would cause large errors in calculations and could be an explanation in the disparities between the two models.

FERR had the largest average calculated mass loss from both models correlating to the measurements of the most pits, highest corroded area and largest pit depths. Although the measurements align with the larger mass loss, these are much greater in comparison to other samples, as already mentioned, other factors may have influenced the calculation which contributed to the values. The current vs time graphs for FERR produced a larger area due to the higher currents measured. As the calculation involved integrating underneath the curves to estimate Q, this would have impacted the final value for Faraday's Law, as it was the only variable to change between grades in the calculation. The difference can be seen in **Figure 33** in the distribution of data points as the mass loss ranges from 0.41mg to 2.37mg for Faraday's Law.

A large disparity can be seen in **Figure 32** between the models also with the pit geometry value, 6.22 mg, being significantly larger than Faraday's Law, 1.55 mg, a 4.67 mg difference. This was due to severe dissolution on the circumference of the sample previously discussed in **Figure 25**, which the technique used to determine corroded area and frequency of pits, detected the large area as one pit instead of many pits coalesced and skewed the results. The difference can be seen in the distribution of data points as the mass loss ranges from 1.48 mg to 6.22 mg for pit

geometry values in **Figure 34**. The median is significantly skewed also of 2.38 mg, showing the impact of the corrosion in one sample.

SAF had the lowest number of pits, corroded area and pit depth which explains the exceptionally low mass loss values from both models, Faraday of 0.07 mg and pit geometry of 0.11 mg. Unlike FERR, SAF had little area under the curve, having less influence on Faraday's Law mass loss, shown in the distribution of both methods in **Figure 33 & 34**, where they are statistically different from FERR and ZER.

ZER also had low mass loss values of Faraday and pit geometry, 0.60 mg and 0.59 mg, respectively, correlating to the lower pits and corroded area measured. As already discussed, ZER's depth of pits was not too dissimilar to FERR and higher currents were recorded, thus increasing Faraday's Law value and explanation to why ZER had slightly larger mass loss than SAF. ZER had low variability in the pit geometry method, seen in **Figure 34**, as the distribution of data points is the lowest for all samples, wider for Faraday's Law as the currents recorded were varied.

Both ZER and SAF had similar mass loss values, indicating consistency in the two mass loss methods but also uniform corrosion performance over the three samples. However, this was not the case for FERR, as significant disparities in corrosion performance affected the mass loss models. This could potentially distort perception of performance if only one method was used for evaluation.

4.2 Influence of Deaeration and Surface Finish on Pit Initiation

Although FERR had a wide distribution of data points, which previously mentioned implies unpredictability, the grade had similar performance in comparison to SAF and ZER. A frequency of 214 pits was not dissimilar to 211 pits of SAF and a corroded area of 0.00488 mm^2 to ZER of 0.00465 mm^2. FERR had the lowest pit depths measured of 19.8 µm, which is unlike the results seen for the previous aerated experiment, where FERR had the deepest pits. This signifies the importance of the differing conditions with the samples ground to a smoother finish, using a nitrogen inlet for deaeration and a slower ramp rate of 10 °C/hour.

SAF also had contradictory results to the previous experiment, with a high frequency of pits at 211 and the largest corroded area of 0.00817 mm^2, with the largest pit depths also, 32.58 µm. This is the opposite to previous where SAF had the lowest values of the three grades. The research of a smoother surface finish seems to not be applicable in this case as it would result in the grade following the same pattern of improved performance. Another factor which could be influencing the experiment is the nitrogen inlet. Impurities or elements in the metal typically support oxygen reduction. Cu has more of a cathodic reaction than Fe, causing higher corrosion rate and increased depth of pits. Under nitrogen, the environment is deaerated so the oxygen cannot react with the impurities and increase the corrosion rate. The elements in SAF may differ and not prevent the corrosion rate from reducing as significantly as seen in FERR. Although, performance was still improved in the deaerated conditions.

One outlier for SAF can be seen in **Figure 39**. The impact of this was evaluated and found to reduce the overall performance of the grade when the outlier was not taken into consideration. The median increased by less than 1 µm but as this is likely to be a true outlier representing natural variation and the effect is small, it shall not be excluded from the data set as measurement inaccuracy as discussed previously, lacy pits etc., could still be a possibility.

ZER had a higher number of pits in comparison to the aerated experiment from 85 to 100 pits but had a much lower corroded area of 0.00465 mm^2 and pit depths of 25.62 µm. As metastable pitting and repassivation are favoured more in an deaerated environment, the appearance of pitting was more visible. This gave a false presence of developed pitting seen in the frequency of pits, although the pit depths measured confirm that these were not existing pits but pits that had repassivated. The same effects of smoother finish and impact of deaerated conditions can be seen as the performance of ZER increased.

As previously mentioned, B. E. Wilde *et al.* [49] found that a smoother finish decreases the probability of pits becoming stable due to a higher E_{pit} value. Burstein *et al.* [29] [32] found that there are more nucleation events but the probability that propagation ensues from a nucleation event is far lower for a smoother surface. This correlates to a higher number of smaller pits and shallower depths. Although there is no potentiostatic data for this surface finish, the frequency of current spikes for the smoother surface samples was far greater than that of the rougher finish. The frequency of metastable pitting on the smoother surface is lower than that of the rougher.

It is well known that the pitting potential tends to decrease as the sample surface roughness increases, caused by the changing characteristics of the sites available for pit initiation. It is easier to maintain a concentrated local chemistry and support a higher frequency of pit initiation [66]. As this paper does not have the current vs temperature graphs from this experiment, a lower E_{pit} cannot be confirmed, although the results from other analysis conducted in research appear to correlate to this finding.

The micrographs in **Figure 24** represent the data discussed above accurately as the pits are hard to distinguish due to the areas being very small. All samples had visible metastable pitting evidence on the surface identified by the dark circles on the surface, with SAF having the greatest amount. These were included in the measurements for frequency of pits as it was mistaken by the software as pits, although no depths were able to be measured as these pits had repassivated.

As discussed in the previous experiment, the lacy pit imaged in FERR 3 indicates how the technique used to measure the pit depths was not highly accurate. No quantifiable data could be taken from the lacy pits which may have altered the overall results in each sample.

Overall, the experiment in deaerated conditions with a smoother surface finish produced more pits, but smaller corroded areas and much shallower pit depths. The differing temperature ramping would mean the samples were under polarisation for a longer period, as both were heated to 85 °C. It would then be expected that both the areas and pit depths would be higher also, which is not the case. As mentioned above, the deaerated conditions would reduce the cathodic reaction with the impurities slowing the propagation rate. This paired with a smoother surface finish would increase the number of nucleation events but inhibit the pits from developing, decreasing the pit depths. There are some environments in industry where oxygen may not be present and deaerated conditions could improve pitting corrosion. The surface finish can also be controlled during manufacturing and should be taken into consideration.

4.3 Crevice Corrosion Susceptibility of SDSS at Temperature

85 °C

The preferential corrosion method was successfully altered from pitting to crevice using an o-ring around the circumference of the rod. This can be seen in **Figure 46** where the corrosion is easily identified by the truncated cylindrical shape around the samples, under where the o-ring had been placed.

FERR had the fastest initial increase in current with all three samples rising just before 500 s. The highest final currents were recorded at 300 mA for FERR 1 and FERR 2 slightly lower at 130 mA. From **Figure 46**, the current for FERR 3 stops ~2000 s due to error in the data collected after this point, which was not beneficial to include in the results. The CCT was not established for each grade in these experiments, but it can be assumed to be similar to CPT although slightly lower according to research [60]. FERR appears to have the lowest CCT as the current rose first by ~200 s. It also had the fastest corrosion rate, seen by the gradient from 500 s – 1000 s, but did level off quickly whereas the other two grades continued to rise for a longer period. From this, it could be predicted that FERR would have the deepest crevice by a substantial amount, but it was not dissimilar to ZER, only 1 µm deeper at 119.47 µm. Although the corrosion mechanism was changed, some pitting was observed on some sample faces, although this was not quantified. This was seen mostly on samples of FERR so could be an explanation for the higher currents observed, and the shallower crevice formed due to additional corrosion methods occurring. This would also result in discrepancy between the pit geometry and Faraday's Law calculations, with Faraday's Law taking all corrosion into account, both pitting as well as crevice. The composition of increased Cu wt% has not seemed to have impacted FERR's performance as well as in Roscoe *et al.* [71] research, although this applies to pitting corrosion and limited research has been undertaken for Cu impact on crevice corrosion. It may be possible that the Cu addition prevented further dissolution although SAF has low copper content, and a lower average crevice depth was observed.

SAF had the slowest increase of initial current across samples, with SAF 2 & 3 rising in the 800s – 1000 s region and SAF 3 rising ~1500 s. The final currents varied significantly with the highest at 110 m A, 50 mA and the lowest 50 mA, but was still the lowest of all three grades. The corrosion rates varied also with low gradients for two samples and a gradual rate for the

third. This correlates accurately to the average depth value as even though SAF had a wide distribution of data points, it had the lowest average depth of 57.51 µm, over half the crevice depth measured in both FERR and ZER. As mentioned previously, SAF has the lowest Cu wt%, although it does have increased Mn, N and Mo wt% which all are known for their properties improving corrosion resistance.

ZER had a similar increase in current across the three samples, with the first rise ~700 s and the last ~200 s later. Although, the final currents varied somewhat with the highest at 17 mA, 120 mA and lowest at 90 mA, there were in a similar region to the currents of FERR. ZER 2 had a sudden decline and rapid incline in current observed, most likely as a result of pit or crevice growth stopping and continuing again after. This sample had a very rapid corrosion rate after the dip with the other samples exhibiting shallower gradients. From these values, it would be expected that ZER would have a similar crevice depth to FERR of 118.84 µm, of 1 µm shallower. The composition of increased W wt% has not seemed to have impacted ZER's performance as well as in previous research [6] [81], although this has only been proven in terms of pitting corrosion instead of crevice. Similarly, to ZER in the first experiment, ZER also had current increases and drops characteristic of metastable pitting at 85 °C. The rate of increase in current was slow relative to which the current decreased, correlating to the repassivation currents Burstein *et al.* [29] [61] theorised.

All three grades had varying results with only FERR having two samples of relatively close final currents. This emphasises the variability in the behaviour of the samples and therefore the unpredictability of the materials in this environment.

The micrograph seen in **Figure 46** is a suitable representative image as all samples analysed had a crevice formed around the entire circumference where the o-ring was placed. The temperature, solution concentration and time under polarisation was above what was needed for each sample to show continuous corrosion around the entire circumference.

75 °C

FERR 2 & 3 had the lowest initial increase of current ~700 s with the last sample increasing ~1100 s. Two of the final currents were similar, 140 mA and 130 mA, but the last sample had a large disparity with a concluding current much lower at 30 mA. This would most likely cause the wide distribution in data points which can be seen in **Figure 56** due to a shallower crevice formed. This difference can also be seen in the corrosion rates, with a stark difference in the gradients observed. The average crevice depth had a clear difference at 95.97 µm, over five times that of ZER. However, there is not a statistical difference as the data plots overlap. Again, pitting was observed on some sample faces but was not quantified. This was seen mostly on samples of FERR so could be an explanation for the high currents observed. Again, it may be possible that the Cu addition prevented further dissolution although SAF has low copper content, and a lower average crevice depth was observed.

SAF had one sample with a similar increase in current to FERR ~700 s but the other two rose ~1500 s. A significant difference was seen in the three final currents with the highest ~150 mA and the lowest both ~10 mA. SAF had a median crevice depth of 50.92 µm. The result of SAF 1 significantly impacted the crevice depths as SAF had similar currents and initial rises in comparison to ZER, but an average crevice depth ~3x deeper. This shows the impact of the high corrosion rate on the mechanical properties of the grade.

ZER had one sample rising ~800 s with the other two rising at intervals of ~300 s and ~600 s after. The samples also had intervals in the final current with the highest at 27 mA, 22 mA and the lowest recorded current of 10 mA. ZER had the lowest median crevice depth by a substantial amount of 17.41 µm. This is correlated with ZER having low recorded currents, delays in initial current rises and shallow gradients. Before the first substantial increase in current, ZER had a distinct rise in current ~250 s which then decayed shortly after back to the background current. There is no slow rise in current following nucleation seen which is indicative of metastable propagation and this is believed to be nucleation of a pit which repassivates immediately after nucleation with no propagation at all [34]. The additional W content may have impacted performance but may also be due to ZER having the highest CCT, providing more stability at this temperature.

Similar to 85 °C, the grades had varying results. In particular SAF, with two samples at low current and one significantly higher. This emphasises the variability in the behaviour of the samples and therefore the unpredictability of the materials in this environment.

The micrographs in **Figures 52, 53 & 54** show representative crevices of each grade. Most samples did not have a crevice form around the entire circumference. This indicates that at this temperature and solution concentration, the time under polarisation was not enough for each sample to show continuous corrosion around the entire circumference. This can be seen in **Figure 55**, where some quarters of the sample did not have any crevice to measure at each quarter. Although SAF did not have the largest crevice depth, the crevice did span most of the quarters showing more corrosion laterally.

Two outliers can be seen in **Figure 56**, one for SAF and the other for ZER. The impact of these were evaluated and found to improve the overall performance of the two grades when the outliers were not taken into consideration, as the medians of both decreased by a minimum of 2 µm. As these are likely to be true outliers and represent natural variation in the samples, these shall not be excluded from the data set, although measurement inaccuracy as discussed previously could still be a possibility.

65 °C

As seen from **Figure 58**, SAF had the first initial rise in current at ~600 s, followed by FERR and ZER ~400 s later. SAF also had the highest final current of 10 mA, substantially higher than the two other grades. This correlates with SAF having the highest median crevice depth of 33.92 µm, with a large statistical difference between FERR and ZER due to no overlap in the data plots. Similarly to the first experiment, SAF also had current increases and drops, followed by a steeper rise in current afterwards, a characteristic of metastable pitting. The rate of increase in current was faster relative to which the current decreased, correlating to the repassivation currents Burstein *et al.* [29] theorised.

Both FERR and ZER had initial increases in current ~1000 s seconds with similar corrosion rates and final currents within ~1 mA of each other. This correlates to both grades having similar crevice depths of 10.28 µm and 14.46 µm, respectively. FERR had the lowest final current and crevice depth suggesting that the grade is the most stable at this temperature,

lowering the current reached, thus reducing formation of the crevice. This could also be applied to ZER, which exhibited the same behaviour but to a lesser extent. Both grades have increased Cu wt% in comparison to SAF, with FERR having the highest wt%, correlates to the results seen but may be other factors contributing. Before the first substantial increase in current, FERR had a small but distinct rise in current ~900 s, which then decayed shortly after to the background current. There is no slow rise in current following nucleation, this is believed to be nucleation of a pit which repassivates immediately after nucleation with no propagation at all [34].

These results correspond to the representative micrographs of each grade seen in **Figures 59, 60 & 61**. FERR can be seen with the smallest crevice formed, ZER with marginally more dissolution and SAF with a considerable crevice which spans most of the quarter. Similarly to 75 °C, all the samples did not have a crevice fully formed around the entire circumference. This suggests that at this temperature, the time under polarisation was not enough for each sample to show continuous corrosion around the entire circumference. This can be seen in **Figure 62** where the majority of samples did not have any crevice to measure at each quarter.

Comparison of Three Temperatures

From **Figures 64, 65 & 66**, it is clear that a drop in temperature decreases the current dramatically. The maximum current reached at each temperature varied, with FERR and ZER having significant drops in current from 85 °C to 75 °C. FERR halved the current from 300 mA to 150 mA and ZER dropped by over 5x, from 170 mA to 30 mA. The most significant current decrease for SAF was from 75 °C to 65 °C of 110 mA to 10 mA. All three grades' average crevice depth dropped by over 50% from 85 °C to 65 °C. The corrosion rates also decreased with all three grades showing shallower gradients as the temperature decreased, which confirms research [62] that temperature is a large influence in corrosion.

85 °C was higher than all three grades CPT and as CCT is generally at a lower temperature, this would explain why all three samples had a large amount of dissolution. 75 °C is similar to the CPT of the grades which shows lesser dissolution than 85 °C but still significant crevice depths. The largest difference in current and crevice depth occurred from 75 °C to 65 °C due to dropping even further below each grades' CPT. It can be predicted that the CCT is not much lower than

65 °C. This can be confirmed as all three grades had small levels of dissolution, with most of the circumference with no crevice to measure at all.

SAF had the smallest difference in depth with increasing temperature suggesting it could be the most stable over a larger temperature range in comparison to the other grades, with an average crevice depth increasing by 32 µm over 20 °C. FERR and ZER had similar increases of 113 µm and 117 µm, respectively.

The scatter of data between temperatures decreases as the temperature decreases. This could be due to the CCT being surpassed by a large extent at 85 °C in comparison to 65 °C, meaning the likelihood of corrosion is increased at higher temperatures. The probability that a nucleation site activates is increased, along with metastable pitting within the crevice and the transition to stable pitting.

Crevice Corrosion Susceptibility Mass Loss

85 °C

FERR had the largest calculated mass loss from both models which correlates to the large depths measured as a result of the experiment. Although the pit geometry value of 0.010 mg was not statistically different to the other grades, the Faraday's Law value was significantly larger, which is inconsistent as the values for average crevice depth did not have such disparity between them. As analysed previously, the current vs time graphs for FERR showed a larger area due to the higher currents measured. This would have impacted the value for Q and therefore the final value. This is most likely due to pitting on the sample face, with conflicting corrosion methods increasing the current. There was considerable disparity in the two methods also, 0.11 mg between each method. The difference can be seen clearly in **Figure 69** where FERR's values are statistically different with comparison to the two other grades also.

The values for both methods were the lowest for SAF corresponding well as the smallest crevice depths were measured for this grade. The lowest currents were recorded also resulting in 0.02 mg mass loss from Faraday's Law with 0.002 mg for pit geometry. SAF also had the smallest difference between calculations also, 0.018 mg, implying small involvement of

external factors affecting Faraday's Law that affected FERR. This is shown as it is the only grade to have both methods values that are not statistically different, seen in **Figure 71**.

ZER had similar crevice depth measurements to FERR which highlights the accuracy of the pit geometry calculation as they are only 0.001 mg in difference. There is a disparity between the two models which could be attributed to the Q calculated for Faraday's Law as ZER had larger currents recorded. The values for both methods were statistically different from **Figure 71**, similar to FERR.

The values calculated for pit geometry were more consistent than for Faraday's Law across the grades. FERR and ZER having similar values of 0.010 mg and 0.009 mg which is also consistent with the average crevice pit depths measured for the two grades being similar also, 119.47 µm and 118.84 µm. In the case of FERR and the occurrence of pitting corrosion, the crevice geometry method would be more accurate due to only the feature of interest taken into consideration. This also positively correlates with the value for SAF with the crevice depth measurement of 57.71 µm. The values also had small variability also, increasing the likelihood of greater accuracy in this method in comparison to Faraday's Law method.

75 °C

FERR had the largest mass loss of both calculations, 0.05 mg and 0.008 mg, correlating to FERR having the deepest crevice measurement of 95.97 µm. This can be seen in the high currents measured where FERR had two samples of the three highest, at 150 mA. FERR had a wide spread of crevice depth data, all included as average was used, increasing pit geometry value. Although, there is not a statistical difference to the other grades, seen in **Figures 74 & 75** and between methods seen in **Figure 76**.

ZER had the smallest mass loss of both calculations, 0.01 mg and 0.002 mg, with the smallest crevice depth of 17.41 µm. The sample had the lowest recorded currents, all under 30 mA which would have less impact on the Faraday value. A significantly smaller spread of data in both mass loss calculations was seen, highlighted in **Figure 76** where the other two grades have exceptionally wide distributions of data points. However, no statistical difference between methods was seen.

Two of the SAF samples had currents under 20 mA but one reaching a maximum of ~160 mA, which is similar to ZER's currents, but SAF 2 had increased the average charge calculation, impacting the Faraday's Law value. This correlates to the crevice depths measured without outliers as SAF and ZER had similar average depths. The spread of data for Faraday's Law is the largest of the three grades and although there is no statistical difference, the impact of the larger current of SAF 2 can be seen clearly in **Figure 74** with the median being much lower than the largest mass loss values. Whilst the charge had a large impact on the value, the pit geometry mass loss value had not been influenced as SAF is only 0.001 mg higher than ZER average.

Again, the values from the pit geometry calculations were more consistent than for Faraday's Law. There was less disparity in Faraday's Law due to smaller currents recorded so the effect was less on the charge calculation. The values also had small variability also, increasing the likelihood of greater accuracy in this method. The pit geometry model assumes that there is a hemispherical cylinder around the full diameter of the sample. As seen in **Figures 52, 53 & 54**, the crevice did not fully form round the circumference of the samples, therefore overestimating the mass loss calculated and reducing the validity of the values stated. Although not produced for this paper, further work could be undertaken to accurately quantify the corrosion area to produce more accurate mass loss.

65 °C

SAF had the largest mass loss of both calculations, 2.00 mg and 0.58 mg, correlating to the high final current reached of 10 mA and the crevice depth, statistically different to the other grades at 33.92 µm. The large charge calculated for SAF would have caused the discrepancy in the two methods.

FERR had the lowest disparity between the two method values which could be attributed to the low current FERR reached of 0.71 mA, the charge having less of an effect on Faraday than seen previously. These values also correlate to FERR having the lowest crevice depth of 10.28 µm. It is unusual to observe that at higher temperatures, FERR consistently reached the highest currents resulting in the deepest pit depths/crevice depths, to then perform better than SAF and ZER, after dropping below a specific temperature. This could imply that when the temperature falls below a certain threshold, FERR's composition promotes material stability. This might

involve the accumulation of metallic copper on the surface, forming a protective insoluble salt when reacting with chloride ions. Since only one sample was tested for each grade, this limited dataset does not provide a full overview of corrosion performance at this temperature. Further research would be required to test a larger number of samples.

ZER had an only slightly deeper crevice than FERR of 14.46 µm, correlating to the similar pit geometry mass loss values and both grades reaching similar final currents, ~10 mA between them with only a 0.03 mg difference. As ZER also reached small final charge values, this would result in a smaller impact of the charge in the Faraday's Law calculation, explanation of the low Faraday's mass loss value.

As seen previously, the values from the pit geometry calculations were more consistent than for Faraday's Law. There was less disparity in Faraday's Law due to smaller currents recorded so the effect was less on the charge calculation. The pit geometry model assumes that there is a hemispherical cylinder around the full circumference of the sample. As seen in **Figures 59, 60 & 61**, the crevice did not fully form round the circumference of the samples, therefore overestimating the mass loss calculated and reducing the validity of the values stated. Although not produced for this paper, further work could be undertaken to accurately quantify the corroded area to calculate more accurate mass loss.

Crevice Corrosion Susceptibility of SDSS at Temperature - Comparison of Three Temperatures

As expected, the drop in mass loss as the temperature decreases correlates to the current dropping also, again proving the influence of temperature on the corrosion of SDSS. There was also a smaller disparity between each calculation with reducing temperature due to smaller charges affecting Faraday's Law values.

Roscoe *et al.* [71] researched the effects of composition in aerated 3% $NaCl + 0.05Na_2SO_4$, at 80 °C and 90 °C on crevice corrosion. They found that immunity potential increased up to 1.5 W wt%, 6 – 6.5% Ni and 3 – 4% Mo gave the minimum mass loss. This composition of the samples used in Roscoe's study are closest to ZER which did have low mass loss but SAF,

containing no additional W, saw a lower mass loss. This suggests that adding W into a composition will not automatically improve its performance in all solutions.

Although both calculations accurately depicted the trends in grades across temperatures, pit geometry was the most consistent of the two methods. Using the depths measured reduced any external factors affecting the calculation, as seen in FERR where some pitting was observed on the top face of the sample and could not be excluded from the current used to calculate the charge.

5.0 Conclusion

Three samples of Super Duplex Stainless Steel, FERR - UNS S32250 (high copper content), SAF - UNS S32750 (low copper content) and ZER - UNS S32760 (tungsten & copper content) were investigated for insight into the role of Cu and W on pitting and crevice corrosion. The influence of surface roughness of the samples and deaeration of the environment was also explored. The experiments were conducted using potentiostatic polarisation techniques, and microscopy to quantify the frequency, area and depth of the dissolution observed. Two mass loss models, Faraday's Law & Pit Geometry, were also implemented to further quantify the corrosion seen.

The first investigation involved the use of 3.5% w/v $NaCl$ solution and the samples heated from 65 °C to 85 °C at a ramp rate of 40 °C/hour.

- Critical Pitting Temperatures (CPT) were not too dissimilar with 4 °C difference between lowest and highest, SAF and ZER, respectively. There were no clear decreases in dissolution as the CPT increased. SAF, paradoxically, had the lowest current measurements which did not correspond to its anticipated higher dissolution due to the lowest CPT. FERR had substantial total number of pits aligning with the highest recorded currents, however exhibited preferential corrosion on the outer circumference, influencing the results. Despite expectations of improved performance due to highest CPT, this was not observed in ZER, with a higher number of pits seen than SAF.

- The presence of metastable pitting was witnessed with SAF and ZER through current fluctuations and on the sample faces, contributing to pit repassivation and the lower number of pits observed.

- Increased Cu alloying in FERR has not shown as significant an impact as seen in other studies. A larger difference was seen in additional W content. The impact of other differences in composition, Mn, N and Mo, should also be considered as small variations in alloying elements could influence corrosion tendencies as seen in SAF.

- The mass loss calculations correlated accurately with the potentiostatic results collected. However, FERR showed a significant disparity between the two models due to a large corroded area being detected as a single pit in the pit geometry model.

- Several key considerations for accuracy of the mass loss calculations:
    - Lacy pits & metastable pitting - impacted pit count and depth measurements.
    - Variability in the pit shape – assumption of hemispherical pits used when pits can take various forms in reality.
    - Important to note that the choice of mass loss model can significantly affect the perceived performance, using multiple can give an overall view.

The second investigation involved samples from previous research in the use of 3.5% w/v $NaCl$ solution and the samples heated from 65 °C to 85 °C at a ramp rate of 30 °C/hour. A deaerated environment was created using a nitrogen inlet and the samples ground to a smoother finish.

- FERR demonstrated improved performance under these conditions compared to the aerated experiment. ZER also exhibited improved performance, which both can be contributed to the smoother surface finish decreasing sites for pit initiation and reduced cathodic reaction in the oxygen-depleted environment. SAF behaved the opposite, with increased pit frequency, area and depth. Metastable pitting was seen across all samples.

- These grades show great performance for industries operating in oxygen-depleted environments. Controlling the surface finish could also positively impact corrosion in application.

The third investigation involved the samples in the use of 3.5% w/v $NaCl$ solution at three temperatures, 85 °C, 75 °C, and 65 °C and held for 30 minutes at the respective temperature. An o-ring was utilised to change the preferential corrosion method from pitting to crevice corrosion.

- At 85 °C, all grades exhibited substantial dissolution, due to surpassing the respective CCT, with deep crevice formation. FERR and ZER both had similar crevice depths, indicating neither increased Cu or W significantly impacted performance.

- At 75 °C, there was a notable reduction in current and crevice depths. Although still above CCT, the crevice did not form around the entire circumference in some samples. FERR displayed variation in crevice depth across samples, implying unpredictability at this temperature. A sudden drop and increase was seen in the potentiostatic data of ZER, indicating metastable pitting behaviour. Additional W proved effective at a lower temperature.

- At 65 °C, there was a large decline in corrosion with some areas of the circumference showing no crevice formation at all. FERR and ZER showed similar behaviour of low crevice depths, indicating higher stability at this temperature but no difference between Cu and W additions.

- SAF demonstrated a stable performance over the temperature range, with less variation in crevice depth compared to FERR and ZER. This gives potential suitability for broad temperature applications.

- The mass loss calculations correlated accurately with the potentiostatic results collected. As anticipated, the decrease in temperature resulted in a reduction of mass loss. Smaller disparities in each model due to smaller charge (Q) impacting Faraday's Law.

- Several key considerations for accuracy of the mass loss calculations:
    - Unquantified corrosion occurring on the sample face, the model would be overestimating the mass loss from crevice corrosion for the Faraday calculations.
    - In some samples the crevice did not fully surround the circumference, overestimating the mass loss for the crevice geometry calculations.

In conclusion, this research has offered insights into the corrosion behaviour of these SDSS grades, highlighting the complex relationship between composition, temperature and other factors. While Cu additions did not show a significant impact in aerated conditions, it showed much improvement in deaerated environments. This could also be attributed to the other variable of smoother surface finish. The addition of W had a more influential role in aerated conditions although both Cu and W additions performed similarly under the crevice corrosion mechanism. The lower alloyed SAF seemed to have irregular behaviour across all experiments. Additionally, a smoother surface finish and absence of oxygen became a crucial factor for influencing corrosion rates.

5.1 Recommendation of Future Research

To develop a further understanding into the corrosion behaviour of the three SDSS grades, further work has been outlined:

- Repeat the crevice corrosion experimentation with a lower range of temperatures to ascertain the specific CCT of each grade.
- Repeat the experiments where surface finish and deaeration are explored separately. This would determine which variable is most beneficial and whether it forms a synergistic effect.
- The use of X-ray Computed Tomography (XCT) could be used to validate the mass loss observed in the samples more accurately.

- Investigate the corrosion properties in a variety of solutions and concentrations e.g., Nitric, hydrochloric, phosphoric and formic acids. This could lead to insight into the behaviour of the grades in industrial applications.

REFERENCES

[1] J. R. Galvele, "Transport processes and the mechanism of pitting of metals," *J. Electrochem. Soc.*, vol. Volume 123, 1976. doi:https://doi.org/10.1016/0010-938X(90)90163-Y

[2] J. P. Simpson, "Corrosion behaviour of cast duplex stainless steels in sulfuric acid containing chloride," *Stainless Steel*, vol. 8, no. 53, 1994. doi:https://doi.org/10.1016/j.msea.2007.08.036

[3] P. Guha and C. A. Clark, "Properties and application of high chromium duplex steels," in *ASM Conference on Duplex Steels*, St. Louis, 1983.

[4] S. Sharafi, "Microstructure of Super-Duplex Stainless Steel, PhD," University of Cambridge, 1993. doi:https://doi.org/10.17863/CAM.14216

[5] A. J. Sedriks, "Corrosion of stainless steels," no. 2, 1996. doi:https://doi.org/10.1016/B978-0-12-803581-8.02893-9

[6] K. Lorentz and G. Medawar, "Tyssenforschung," vol. 1, pp. 97-108, 1969.

[7] J. Alsarraf, Hydrogen embrittlement susceptibility of super duplex stainless steels, PhD, Cranfield University, 2010.

[8] J. O. Nilsson, "Super Duplex Stainless Steel," *Materials Science and Technology*, vol. 8, p. 685–700, 1992. doi:https://doi.org/10.1179/mst.1992.8.8.685

[9] R. J. Brigham and E. W. Tozer, "Temperature as a pitting criterion," *Corrosion*, vol. 29, pp. 33-36, 1973. doi:https://doi.org/10.5006/0010-9312-29.1.33

[10] A. J. Sedriks, "Effects of alloy composition and microstructure on the passivity of stainless steels," *Corrosion*, pp. 376-389, 1986. doi:https://doi.org/10.5006/1.3584918

[11] C. Moyano, Learn the Anti-Corrosion Code, Parker, 2017. [Online]. Available: https://www.parker.com/content/dam/Parker-com/Literature/Instrumentation-Products-Division/Technical-Articles/Learn_the-Anti-corrosion_code.pdf. [Accessed 15 March 2023].

[12] Anon., "Corrosion," 2019. [Online]. Available: https://chem.libretexts.org/Courses/Saint_Marys_College_Notre_Dame_IN/CHEM_122-02_(Under_Construction)/4%3A_Electrochemistry/4.1%3A_Electrochemistry/Corrosion. [Accessed 15 March 2023].

[13] S. Lower, "Electrochemical Corrosion," [Online]. Available: https://chem.libretexts.org/Bookshelves/General_Chemistry/Book%3A_Chem1_(Lower)/16%3A_Electrochemistry/16.08%3A_Electrochemical_Corrosion. [Accessed 15 March 2023].

[14] C. V. L. Sabará, L. N. S. Prachedes and L. C. Santos, "Influence of parameters related to microstructure, chemical composition and environment characteristics on localised corrosion failure susceptibility of supermartensitic stainless steels," *Engineering Failure Analysis*, vol. 27, 2021. doi:https://doi.org/10.1016/j.engfailanal.2021.105524

[15] K. Hashimoto, K. Asami, A. Kawashima, H. Habazaki and E. Akiyama, “The role of corrosion-resistant alloying elements in passivity,” *Corrosion Science,* vol. 49, p. 42–52, 2007.
doi:https://doi.org/10.1016/j.corsci.2006.05.003

[16] G. S. Frankel, “Pitting corrosion of metals: A review of the critical factors,” *J. Electrochem. Soc.,* 1998.
doi:https://doi.org/10.5006/1.3292074

[17] W. Schwenk, “Theory of Stainless Steel Pitting,” *Corrosion,* vol. 20, pp. 129-137, 1964.

[18] D. A. Jones, Principles and Prevention: Corrosion 2, 1996.

[19] H. S. Isaacs and G. Kissel, “Surface Preparation and Pit Propagation in Stainless Steels,” *J. Electrochem. Soc.,* vol. 119, p. 1628–1632, 1972.
doi:10.1149/1.2404061

[20] G. S. Frankel, “Perspective – Localized Corrosion: Passive Film Breakdown vs Pit Growth Stability,” *Journal of The Electrochemical Society,* vol. 164, 2017.
doi:10.1149/2.1381704jes

[21] G. Frankel and N. Sridhar, “Understanding Localized Corrosion,” *Materials Today,* vol. 11, pp. 38-44, 2008.
doi:https://doi.org/10.1016/S1369-7021(08)70206-2

[22] Z. Szklarska – Smialowska, “Review of Literature on Pitting Corrosion Published since 1960,” *Corrosion,* vol. 27, pp. 223-233, 1971.
doi:https://doi.org/10.5006/0010-9312-27.6.223

[23] K. V. Akpanyung and R. T. Loto, “Pitting corrosion evaluation: a review,” *Journal of Physics: Conference Series,* vol. 2378, 2019.

[24] N. J. Laycock, J. Stewart and R. C. Newman, “The initiation of crevice corrosion in stainless steels,” *Corrosion Science,* vol. 39, p. 1791–1809, 1997.
doi:https://doi.org/10.1016/S0010-938X(97)00050-4

[25] P. C. Pistorius and G. T. Burstein, “Metastable pitting corrosion of stainless steel and the transition to stability,” *Phil. Trans. R. Soc. Lond.,* vol. 321, no. 1662, 1992.
doi:https://doi.org/10.1098/rsta.1992.0114

[26] M. H. Moayed and R. C. Newman, “Evolution of current transients and morphology of metastable and stable pitting on stainless steel near the critical pitting temperature,” *Corrosion Science,* vol. 48, no. 4, pp. 1004-1008, 2006.
doi:10.1016/j.corsci.2005.03.002

[27] P. Ernst, N. J. Laycock, M. H. Moayed, R. C. Newman, M. H. Moayed and R. C. Newman, “The mechanism of lacy cover formation in pitting,” *Corrosion Science,* vol. 39, no. 6, pp. 1133-1136, 1997.
doi:https://doi.org/10.1016/S0010-938X(97)00043-7

[28] P. C. Pistorius and G. T. Burstein, “Growth of corrosion pits on stainless steel in chloride solution containing dilute sulphate,” *Corrosion Science,* vol. 33, pp. 1885-1897, 1992.
doi:https://doi.org/10.1016/0010-938X(92)90191-5

[29] G. T. Burstein and S. P. Vines, “Repetitive nucleation of corrosion pits on stainless steel and the effects of surface roughness,” *J. Electrochem. Soc,* vol. 48, 2001.
doi:http://dx.doi.org/10.1149/1.1416503

[30] G. T. Burstein and S. P. Mattin, “Nucleation of corrosion pits on stainless steel,” *Philosophical Magazine Letters,* vol. 63, pp. 127-131, 1992. doi:10.5772/intechopen.70579

[31] S. P. Mattin and G. T. Burstein, “Detailed resolution of microscopic depassivation events on stainless steel in chloride solution leading to pitting,” *Philosophical Magazine Letters,* vol. 76, pp. 341-348, 1997.

[32] G. T. Burstein and P. C. Pistorius, “Surface roughness and the metastable pitting of stainless steel in chloride solutions,” *Corrosion,* vol. 51, pp. 380-385, 1995. doi:http://dx.doi.org/10.1016/j.corsci.2014.04.033

[33] J. R. Galvele, “Transport processes in passivity breakdown – II. Full hydrolysis of the metal ions,” *Corrosion Science,* vol. 21, pp. 551-579, 1981. doi:https://doi.org/10.1016/0010-938X(81)90009-3

[34] A. M. Riley, D. B. Wells and D. E. Williams, “Initiation events for pitting corrosion of stainless steel?,” *Corrosion Science,* vol. 32, pp. 1307-1313, 1991. doi:https://doi.org/10.1016/0010-938X(91)90050-Y

[35] T. Wenming, D. Nan, S. Li, S. Chen and Q. Wu, “Metastable pitting corrosion of 304 stainless steel in 3.5% w/v NaCl solution,” *Corrosion Science,* vol. 85, pp. 372-279, 2014. doi:10.1016/j.corsci.2014.04.033

[36] Y. C. Tang and A. J. Davenport, “Magnetic field effects on the corrosion of artificial electrodes and pits in thin films,” *J. Electrochem. Soc.,* vol. 154, pp. 262-370, 2007. doi:http://dx.doi.org/10.1149/1.2736662

[37] T. Li, “Localized Corrosion: Passive Film Breakdown vs. Pit Growth Stability: Part III. A Unifying Set of Principal Parameters and Criteria for Pit Stabilization and Salt Film Formation,” *J. Electrochem. Soc.,* vol. 165, 2018. doi:10.1149/2.0251811jes

[38] C. Nyby, X. Guo, J. Saal, S. Chien and A. Gerard, “Electrochemical metrics for corrosion resistant alloys,” *Scientific Data,* vol. 8, no. 58, 2021. doi:10.1038/s41597-021-00840-y

[39] J. Soltis, “Passivity breakdown, pit initiation and propagation of pits in metallic materials – Review,” *Corrosion Science,* vol. 90, pp. 5-22, 2015. doi:10.1016/j.corsci.2014.10.006

[40] N. J. Laycock and R. C. Newman, “Localised dissolution kinetics, salt films and pitting potentials,” *Corrosion Science,* vol. 39, pp. 1771-1790, 1997. doi:https://doi.org/10.1016/S0010-938X(97)00049-8

[41] A. S. H. Makhlouf and M. A. Botello, “Failure of the metallic structures due to microbiologically induced corrosion and techniques for protection,” *Handbook of materials failure analysis,* 2018.

[42] R. P. Frankenthal and H. W. Pickering, “On the mechanism of localized corrosion of iron and stainless steel: II. Morphological Studies,” *J. Electrochem. Soc.,* vol. 119, pp. 1304-1310, 1972.

[43] T. Materia, Corrosion and Corrosion Properties of Stainless Steels: Part Two, 2008. [Online]. Available: https://www.totalmateria.com/page.aspx?ID=CheckArticle&site=kts&NM=235 [Accessed 15 March 2023].

[44] G. C. Wood, J. A. Richardson and M. F. Abd Rabbo, "The role of flaws in breakdown of passivity of aluminum and crevice corrosion of stainless steel," *J. Electrochem. Soc.,* pp. 973-988, 1978.

[45] B. A. Kehler and J. R. Scully, "Role of metastable pitting in crevices on crevice corrosion stabilization in Alloys 625 and 22," *Corrosion,* vol. 61, pp. 665-684, 2005. doi:https://doi.org/10.5006/1.3278202

[46] R. C. Newman, "W.R.Whitney Award Lecture: Understanding the Corrosion of Stainless Steel," *Corrosion,* vol. 27, pp. 1030-1041, 2001. doi:https://doi.org/10.5006/1.3280390

[47] D. Han, Y. M. Jiang, C. Shi, B. Deng and J. Li, "Effect of temperature, chloride ion and pH on the crevice corrosion behaviour of SAF 2205 duplex stainless steel in chloride solutions," *Journal of Materials Science,* vol. 47, pp. 1018-1025, 2012. doi:10.1007/s10853%2D011%2D5889%2D6

[48] J. W. Oldfield and W. H. Sutton, "Crevice Corrosion of Stainless Steels: II. Experimental Studies," *British Corrosion Journal,* vol. 13, pp. 104-111, 1978. doi:https://doi.org/10.1179/000705978798276258

[49] B. E. Wilde and E. Williams, "The use of current/voltage curves for the study of localized corrosion and passivity breakdown on stainless steels in chloride media," *Eltrochemimica Acta,* vol. 16, pp. 1971-1985, 1971. doi:10.1016/0013-4686(71)85151-4

[50] N. Sridhar and D. S. Dunn, "An electrochemical approach to predicting long-term localized corrosion of corrosion resistant container materials," *Corrosion,* vol. 50, pp. 857-872, 1997.

[51] S. E. Lott and R. C. Alkire, "The Role of Inclusions on Initiation of Crevice Corrosion of Stainless Steel: I . Experimental Studies," *Journal of The Electrochemical Society,*vol. 136, no. 4, 1989. 10.1149/1.2096896

[52] H. W. Pickering, H. Shu and F. M. Al-Faqeer, "Pitting on the crevice wall prior to crevice corrosion: Iron in sulfate/chromate solution," *Electrochim. Acta,* vol. 56, pp. 1719-1728, 2011.

[53] L. Stockhert and H. Boehni, "Susceptibility to crevice corrosion and metastable pitting of stainless steel," *Mater. Sci. Forum,* pp. 313-328, 1991. doi:https://doi.org/10.4028/www.scientific.net/MSF.44-45.313

[54] J. R. Galvele, "Tafel's law in pitting corrosion and crevice corrosion susceptibility," *Corrosion Science,* vol. 47, pp. 3052-3067, 2005. doi:10.1016/j.corsci.2005.05.043

[55] E. Shojaei, M. Mirjalili and M. H. Moayed, "The influence of the crevice induced IR drop on polarisation measurement of localized corrosion behaviour of 316L stainless steel," *Corrosion Science,* vol. 156, pp. 96-105, 2019.

doi:10.1016/j.corsci.2019.04.030
[56] M. Nishimoto, J. Ogawa, I. Muto, Y. Sugawara and N. Hara, “Simultaneous visualization of pH and Cl- distributions inside the crevice of stainless steel,” *Corrosion Science,* vol. 106, pp. 298-302, 2016.
doi:https://doi.org/10.1016/j.corsci.2016.01.028
[57] P. C. Pistorius and G. T. Burstein, “Aspects of the effects of electrolyte composition on the occurrence of metastable pitting on stainless steel,” *Corrosion Science,* vol. 36, pp.525-538, 1994.
doi:https://doi.org/10.1016/0010-938X(94)90041-8
[58] D. E. Williams, J. Stewart and P. H. Balkwill, “The nucleation, growth and stability of micropits in stainless steel,” *Corrosion Science,* vol. 35, pp. 1213-1235, 1994.
doi:https://doi.org/10.1016/0010-938X(94)90145-7
[59] E. Shojaei, M. H. Moaeyed, M. Mirjalili and S. Pahlaven, “Proposed stability product criterion for open hemispherical metastable pits formed in the crevices of different aspect ratios (l/d) on 316L stainless steel in 3.5% w/v NaCl solution,” *Corrosion Science,* vol. 184, 2021.
doi:10.1016/j.corsci.2021.109389
[60] P. T. Jakobsen and E. Maahn, “Temperature and potential dependence of crevice corrosion of AISI 316 stainless steel,” *Corrosion Science,* vol. 43, pp. 1693-1709, 2001.
doi:10.1016/S0010-938X(00)00167-0
[61] P. Ernst and R. C. Newman, “Pit growth studies in stainless steel foils. I. Introduction and pit growth kinetics,” *Corrosion Science,* vol. 44, no. 5, pp. 927-941, 2002.
doi:https://doi.org/10.1016/S0010-938X(01)00133-0
[62] L. Zhang, Y. Jiang, B. Deng, D. Sun, J. Gao and J. Li, “Effect of temperature change rate on the critical pitting temperature for duplex stainless steel,” *Journal of Applied Electrochemistry,* vol. 29, pp. 1703-1708, 2009.
doi:10.1007/s10800-009-9863-9
[63] C. R. Lauritsen, Pitting Corrosion of Super Duplex Stainless Steel-Effect of Isothermal Heat Treatment, NTNU, 2016.
[64] P. E. Manning, D. J. Duquette and W. F. Savage, “The effect of test method and surface condition on pitting potential of single and duplex phase 304L stainless steel,” *Corrosion,* vol. 35, pp. 151-157, 1979.
doi:https://doi.org/10.5006/0010-9312-35.4.151
[65] L. F. Lin, C. Y. Chao and D. D. Macdonald, “A point defect model for anodic passive films: II. Chemical breakdown and pit initiation,” *J. Electrochem. Soc.,* vol. 128,1981.
doi:10.1149/1.2127592
[66] M. H. Moayed, N. J. Laycock and R. C. Newman, “Dependence of the critical pitting temperature on surface roughness,” *Corrosion Science,* vol. 45, pp. 1203-1216, 2003.
doi:10.1016/S0010-938X(02)00215-9
[67] Y. Tang, N. Dai, J. Wu, Y. Jiang and J. Li, “Effect of Surface Roughness on Pitting Corrosion of 2205 Duplex Stainless Steel Investigated by Electrochemical Noise Measurements,” *Materials,* vol. 12, 2019.

doi:10.3390/ma12050738

[68] J. Bonfield, The influence of copper and tungsten additions on the passivity and pitting corrosion resistance of super duplex stainless steels, MRes, Swansea University, 2019.

[69] D. Klenam, *Effect of temperature and carbonaceous environment on the fatigue behaviour of AISI 316L austenitic stainless steel,* p. 12, 2013. doi:10.13140/RG.2.1.5109.0967

[70] Y. Yu, S. Shironita, K. Souma and M. Umeda, "Effect of chromium content on the corrosion resistance of ferritic stainless steels in sulfuric acid solution," *Heliyon,* vol. 4, no. 11, 2018. doi:https://doi.org/10.1016/j.heliyon.2018.e00958

[71] C. V. Roscoe and K. J. Gradwell, "The history and development of duplex stainless steels," *Duplex Stainless Steel,* 1986.

[72] S. Ogura, K. Sugimoto and Y. Sawada, "Effects of Cu, Mo and C on the corrosion of deformed 18Cr-8Ni stainless steels in H2SO4/NaCl solutions," *Corrosion Science,* vol.16, pp. 323-337, 1976. doi:https://doi.org/10.1016/0010-938X(76)90118-9

[73] H. G. Kivisäkk and J. Frodigh, "Influence of copper in super duplex stainless steel on iso-corrosion curves in hydrochloric acid and dilute sulfuric acid," *Corrosion,* 2013.

[74] J. Lee, S. Kim, I. Lee, G. Kim, J. Kim and Y. Park, "Effect of Copper Addition on the Active Corrosion Behavior of Hyper Duplex Stainless Steels in Sulfuric Acid," *MATERIALS TRANSACTIONS,* vol. 53, no. 6, pp. 1048-1055, 2012. doi:https://doi.org/10.2320/matertrans.M2012008

[75] L. Garfias-Mesias, J. Sykes and C. Tuck, "The effect of phase compositions on the pitting corrosion of 25 Cr duplex stainless steel in chloride solutions," *Corrosion Science,* vol. 38, no. 8, pp. 1319-1330, 1996. doi:10.1016/0010-938X(96)00022-4

[76] L. Garfias-Mesias and J. Sykes, "Effect of copper on active dissolution and pitting corrosion of 25% Cr duplex stainless steels," *CORROSION,* vol. 54, no. 1, pp. 40-47, 1998. doi:10.5006/1.3284827

[77] I. Olefjord and L. Wegrelius, "The influence of nitrogen on the passivation of stainless steels," *Corrosion Science,* vol. 38, pp. 1203-1220, 1996. doi:https://doi.org/10.1016/0010-938X(96)00018-2

[78] M. Janik-Czachor, E. Lunarska and Z. Szklaraska-Smialowska, "Corrosion," vol. 21, p. 349, 1975. doi:https://doi.org/10.1016/0010-938X(96)00018-2

[79] C. Torres, R. Johnsen and M. Iannuzzi, "Crevice corrosion of solution annealed 25Cr duplex stainless steels: Effect of W on critical temperatures," *Corrosion Science,* vol. 178, 2021. doi:https://doi.org/10.1016/j.corsci.2020.109053

[80] E. Rahimi, A. Kosari, S. Hosseinpour, A. Davoodi, H. Zandbergen and J. Mol, "Characterization of the passive layer on ferrite and austenite phases of super duplex stainless steel," *Applied Surface Science,* vol. 496, 2019. doi:https://doi.org/10.1016/j.apsusc.2019.143634

[81] E. B. Haugan and M. Naess, “Effect of tungsten on the pitting and crevice corrosion resistance of type 25Cr super duplex stainless steels,” *Corrosion,* vol. 73, 2017. doi:10.5006/2185

[82] Z. Skzlarska-Smialowska, “Surface Treatments,” *Pitting and Crevice Corrosion,* pp. 519-533, 2005.

[83] J. Kim and H. Kwon, “Effects of Tungsten on Corrosion and Kinetics of Sigma Phase Formation of 25% Chromium Duplex Stainless Steels,” *Corrosion,* vol. 55, no. 5, pp. 515-521, 1999. doi:https://doi.org/10.5006/1.3284014

[84] N. Bui, A. Irhzo, F. Dabosi and Y. Limouzin-Maire, “On the Mechanism for Improved Passivation by Additions of Tungsten to Austenitic Stainless Steels,” *Corrosion,* vol. 39, pp. 491-496, 1983. doi:https://doi.org/10.5006/1.3577373

[85] “ASTM G31 – 12A – Standard guide for laboratory immersion corrosion testing of metals’’ ASTM International, 2012.

[86] F. Malaret, “Exact calculation of corrosion rates by the weight-loss method” *Experimental Results*, 2022. doi:10.1017/exp.2022.5

[87] E. Ahmed Ali, “Mathematical Modelling of Corrosion Measurements” Doctor of Philosophy Thesis, University of Wollongong, 1999. doi:http://ro.uow.edu.au/theses/2051

[88] B. Sundén, “Chapter 2 - Electrochemistry and Thermodynamics. Hydrogen, Batteries and Fuel Cells”, *Academic Press*, pp. 15-36, 2019. doi:https://doi.org/10.1016/B978-0-12-816950-6.00002-6.

[89] Langley Alloys Ltd, “Introduction to Duplex and Super Duplex Stainless Steels,” 2020.

[90] E. Purkhardt, “Effect of Cu and W additions on pitting corrosion resistance of super duplex stainless steels”. MSc thesis submitted for examination, 2023.

[91] “ASTM G150 – Standard test methods for electrochemical critical pitting temperature testing of stainless steel”. [Online]. Available: https://www.astm.org/g0150-18.html [Accessed November 2022].

[92] Langley Alloys Ltd, “New Guide to Duplex and Super Duplex Stainless Steels”, 2020. [Online]. Available: https://www.langleyalloys.com/2020/04/16/guide-duplex-super-duplex-stainless-steels/ [Accessed October 2022].